



ANNUAL  
REVIEWS **Further**

Click [here](#) to view this article's online features:

- Download figures as PPT slides
- Navigate linked references
- Download citations
- Explore related articles
- Search keywords

# Mass Fractionation Laws, Mass-Independent Effects, and Isotopic Anomalies

Nicolas Dauphas<sup>1,\*</sup> and Edwin A. Schauble<sup>2</sup>

<sup>1</sup>Origins Laboratory, Department of the Geophysical Sciences and Enrico Fermi Institute, The University of Chicago, Chicago, Illinois 60637; email: [dauphas@uchicago.edu](mailto:dauphas@uchicago.edu)

<sup>2</sup>Department of Earth and Space Sciences, University of California, Los Angeles, California 90095

Annu. Rev. Earth Planet. Sci. 2016. 44:709–83

First published online as a Review in Advance on May 18, 2016

The *Annual Review of Earth and Planetary Sciences* is online at [earth.annualreviews.org](http://earth.annualreviews.org)

This article's doi:  
10.1146/annurev-earth-060115-012157

Copyright © 2016 by Annual Reviews.  
All rights reserved

\*Corresponding author

## Keywords

isotopes, fractionation, laws, NFS, nuclear, anomalies, nucleosynthesis, meteorites, planets

## Abstract

Isotopic variations usually follow mass-dependent fractionation, meaning that the relative variations in isotopic ratios scale with the difference in mass of the isotopes involved (e.g.,  $\delta^{17}\text{O} \approx 0.5 \times \delta^{18}\text{O}$ ). In detail, however, the mass dependence of isotopic variations is not always the same, and different natural processes can define distinct slopes in three-isotope diagrams. These variations are subtle, but improvements in analytical capabilities now allow precise measurement of these effects and make it possible to draw inferences about the natural processes that caused them (e.g., reaction kinetics versus equilibrium isotope exchange). Some elements, in some sample types, do not conform to the regularities of mass-dependent fractionation. Oxygen and sulfur display a rich phenomenology of mass-independent fractionation, documented in the laboratory, in the rock record, and in the modern atmosphere. Oxygen in meteorites shows isotopic variations that follow a slope-one line ( $\delta^{17}\text{O} \approx \delta^{18}\text{O}$ ) whose origin may be associated with CO photodissociation. Sulfur mass-independent fractionation in ancient sediments provides the tightest constraint on the oxygen partial pressure in the Archean and the timing of Earth's surface oxygenation.

Heavier elements also show departures from mass fractionation that can be ascribed to exotic effects associated with chemical reactions such as magnetic effects (e.g., Hg) or the nuclear field shift effect (e.g., U or Tl). Some isotopic variations in meteorites and their constituents cannot be related to the terrestrial composition by any known process, including radiogenic, nucleogenic, and cosmogenic effects. Those variations have a nucleosynthetic origin, reflecting the fact that the products of stellar nucleosynthesis were not fully homogenized when the Solar System formed. Those anomalies are found at all scales, from nanometer-sized presolar grains to bulk terrestrial planets. They can be used to learn about stellar nucleosynthesis, mixing in the solar nebula, and genetic relationships between planetary bodies (e.g., the origin of the Moon). They can also confound interpretations based on dating techniques (e.g.,  $^{146}\text{Sm}$ - $^{142}\text{Nd}$ ) when they are misidentified as isotopic variations of radiogenic origin. To summarize, there is a world to explore outside of mass-dependent fractionation whose impact is promised to expand as analytical capabilities to measure ever-subtler isotopic anomalies on ever-smaller samples continue to improve.

## 1. INTRODUCTION

In natural systems, isotopic variations can arise from a variety of processes such as phase equilibrium, unidirectional reactions, radioactive decay, and nuclear transmutations induced by particle irradiation. The study of these variations is the basis of isotope geochemistry, spanning an ever-expanding range of applications, from biochemistry to nuclear astrophysics. Most isotopic variations in Solar System materials follow clear sets of rules. Phase equilibrium and unidirectional reactions are most often associated with mass-dependent variations, meaning that the degree of isotopic fractionation scales with the difference in mass of the isotopes involved. Radioactive decay produces variations in the abundances of the daughter isotopes that scale with parent-to-daughter ratios. Nuclear transmutations by particle irradiation, coming either from space (cosmogenic) or from surrounding rocks by decay of radioactive nuclides (nucleogenic), only affect certain isotopes in specific settings.

In some cases, isotopic variations are found that depart from those rules and are categorized as anomalies. Isotopic anomalies were discovered when Black & Pepin (1969) measured the isotopic composition of neon released during stepwise heating of carbonaceous chondrites. They identified a component extremely rich in  $^{22}\text{Ne}$ , labeled Ne-E (letters A to D were already taken), that could not be related to neon in air by any of the processes discussed above. Years later, it was shown that this component has a nucleosynthetic origin, meaning that it is hosted in presolar grains of silicon carbide (Ming & Anders 1988) and graphite (Amari et al. 1990). Developments in mass spectrometry and accompanying improvements in precision of isotope ratio analyses revealed that isotopic anomalies were widespread in planetary materials (Clayton 1978, Huss & Lewis 1995, Birck 2004).

The divide between mass-dependent fractionation and isotopic anomalies is not clear-cut. The reason is that mass-dependent fractionation is not uniquely defined and can be described using various laws that depend on the cause for the fractionation (Maréchal et al. 1999, Young et al. 2002). Often, isotopic variations are small, so mass-dependent fractionation cannot be easily distinguished from bona fide isotopic anomalies. This contribution therefore starts (Section 2) with a discussion of the theory of mass-dependent fractionation and reviews emerging applications of mass fractionation laws in Earth and planetary sciences.

Isotopic anomalies are departures from mass-dependent fractionation and can be divided into clearly distinct categories: Some were produced in the Solar System by nebular, planetary, or

geological processes, whereas others were inherited from stellar nucleosynthesis. Oxygen and sulfur present a very rich phenomenology of isotopic anomalies in meteorites, planetary atmospheres, sediments, and igneous rocks. Although there is a near consensus on the general causes of some of these anomalies, important disagreements remain. The uncertainties have not prevented their use as geochemical tracers, however, and these are reviewed in Section 3. This section cannot give justice to the considerable amount of work done on this topic, and the reader is referred to relevant reviews (Clayton 1993, 2003; Farquhar & Wing 2003; Thiemens 2006).

The best-documented reactions that produce oxygen and sulfur isotopic anomalies involve gas phase chemistry. Heavy elements that do not form volatile compounds can also display mass-independent fractionation caused by at least two chemical processes (the field shift effect and a probable magnetic isotope effect). Of these processes, the field shift effect is relatively well understood. In heavy elements, the nucleus can influence the strength of the chemical bonds that are formed, which can induce a fractionation that is not strictly mass dependent and is often characterized by an odd-even modulation of the isotope variations (Bigeleisen 1996a, Fujii et al. 1989). This phenomenon and examples drawn from nature and experiments are presented in Section 4.

Early work on noble gases revealed the presence of material extraneous to the Solar System that was characterized by very large isotopic anomalies relative to terrestrial composition (Black & Pepin 1969). The search for the carriers of these anomalies led to the identification of presolar grains, which formed in the outflows of stars that lived and died before the Solar System was formed (Bernatowicz et al. 1987, Lewis et al. 1987). By analyzing the compositions of those grains in a laboratory setting, one can study the compositions of stars with a precision level that is unachievable by remote astronomical observations (Section 5). Some anomalies, albeit of smaller magnitude, are manifested at larger scales, ranging from millimeter-sized grains to planets.

In presolar grains, isotopic variations are very large, so precision in isotopic analyses is often less of an issue than spatial resolution and isobaric interferences. At the other end of the size spectrum, bulk planetary bodies display isotopic anomalies that are very subtle and call for highly precise and accurate measurements (Clayton et al. 1973, Dauphas et al. 2002b). Such planetary-scale anomalies provide a means to (*a*) study stellar nucleosynthesis of elements that cannot be easily measured in presolar grains using *in situ* techniques, (*b*) trace genetic relationships between planetary bodies, and (*c*) understand how dust was size sorted, vaporized, and condensed in the solar nebula (Section 6). Isotopic anomalies are also potential pitfalls as they can be mistaken for variations arising from radioactive decay in dating planetary differentiation and early Solar System events (Section 7).

## 2. MASS FRACTIONATION LAWS

For most elements, the dominant naturally occurring chemical processes that act to separate isotopes from each other depend ultimately on differences in mass. Isotope masses affect the velocities and diffusivities of atoms and molecules. Mass differences also affect vibrational and rotational frequencies, altering spectral features (and photochemical cross sections), as well as thermodynamic energies (and thus equilibria and activation energies of reactions). Each of these mass-related effects can cause different isotopes to react at different rates and partition unequally between reactants and products. As a result, the separation of isotopes typically scales in proportion to differences in isotopic mass. For example, the  $^{17}\text{O}/^{16}\text{O}$  ratio usually changes by roughly half as much as the  $^{18}\text{O}/^{16}\text{O}$  ratio because the mass difference between  $^{17}\text{O}$  and  $^{16}\text{O}$  (1.0042 amu) is roughly half as large as the mass difference between  $^{18}\text{O}$  and  $^{16}\text{O}$  (2.0042 amu). Isotope fractionations that are

observed to follow this proportionality are called mass-dependent fractionations; fractionations that depart markedly are termed mass-independent fractionations. These names are potentially misleading, however, because the distinction is empirical rather than mechanistic. It is possible for differences in isotopic mass to drive isotope separations that are wildly disproportionate, for instance, in the self-shielding photochemical fractionation proposed to explain mass-independent fractionation in sulfur isotopes from Archean rocks and oxygen isotopes in meteorites (Farquhar et al. 2001, Clayton 2002). Mass-dependent physical and chemical processes (e.g., equilibrium partitioning versus diffusion) also impart a (typically small) range of mass fractionation relationships. Conversely, the nuclear field shift effect, dependent on the shape and volume of space occupied by nuclei rather than their mass (Bigeleisen 1996a), generates isotope fractionations of the major even-numbered isotopes of mercury ( $^{198}\text{Hg}$ ,  $^{200}\text{Hg}$ ,  $^{202}\text{Hg}$ , and  $^{204}\text{Hg}$ ) (Ghosh et al. 2008) that appear mass dependent even though the odd isotopes  $^{199}\text{Hg}$  and  $^{201}\text{Hg}$  often show strong mass-independent fractionation effects (Bergquist & Blum 2007). The field shift effect is also expected to generate nearly proportionate isotope fractionations for all of the major isotopes of tungsten and platinum (Schauble 2013a) despite the lack of any mechanistic dependence on mass differences in the field shift effect.

Interest in slight differences in relationships between fractionation and mass, depending on the types of reactions and isotopes studied, has intensified as measurement precision has improved and potential uses of measured differences have been proposed (e.g., Eiler et al. 2014). It should be noted, however, that the study of the variability in mass fractionation laws includes a number of early investigations of the relationships between D/H and T/H fractionation of the hydrogen isotopes (e.g., Grilly 1951, Bigeleisen 1962, Bron et al. 1973, Pyper & Christensen 1975). Hulston & Thode (1965) and Matsuhisa et al. (1978) were among the first to theoretically investigate variability in mass fractionation laws applied to the isotopes of heavier elements. Matsuhisa et al. (1978) calculated the relationship between  $^{17}\text{O}/^{16}\text{O}$  and  $^{18}\text{O}/^{16}\text{O}$  fractionation in  $\text{CO}_2$ , relative to  $\text{H}_2\text{O}$  vapor, as a function of temperature, in order to better understand experimental isotope exchange equilibrations between isotopically labeled phases. Hulston & Thode (1965) made analogous calculations on sulfur isotope fractionation in simple molecules, to provide a frame of reference for understanding meteoritic measurements. Their work, along with roughly contemporary investigation of the importance of mass fractionation laws for correcting mass fractionation induced by mass spectrometers in the measurement of calcium isotopes (Russell et al. 1978), provided a foundation for the study of mass fractionation relationships in multiple-isotope systems. In this section, the concepts of theoretical estimation of mass fractionation laws are reviewed for mass-dependent equilibrium and kinetic isotope effects. Young et al. (2002) provided a useful starting point, as they gave compact descriptions of mass fractionation laws for several processes. Deviations from these type cases in geochemical and cosmochemical environments are discussed.

## 2.1. Terminology and Notation

For the sake of clarity, we will slightly adapt the notation of Mook (2000), which is widely used in theoretical discussions of mass fractionation laws (e.g., Farquhar et al. 2003, Cao & Liu 2011). The theoretical study of mass fractionation laws by Young et al. (2002) used a somewhat different system of symbols, superscripts, and subscripts, which have been adopted mainly among planetary scientists and high-temperature geochemists. In both cases, mass laws for isotope fractionation are described in terms of fractionation factors ( $\alpha$ ), equal to isotope abundance ratios in one substance

relative to another:

$${}^{i2/i1}\alpha_{a-b} = \frac{\left(\frac{X_{i2}}{X_{i1}}\right)_a}{\left(\frac{X_{i2}}{X_{i1}}\right)_b}. \quad (1)$$

Here  $a$  and  $b$  are the substances of interest, and  $(X_{i2}/X_{i1})_a$  and  $(X_{i2}/X_{i1})_b$  are the abundance ratios of isotopes  $i2$  and  $i1$  in each substance. For a third isotope in the same system, an analogous expression describes  $i3/i1$  fractionation:

$${}^{i3/i1}\alpha_{a-b} = \frac{\left(\frac{X_{i3}}{X_{i1}}\right)_a}{\left(\frac{X_{i3}}{X_{i1}}\right)_b}. \quad (2)$$

It is useful to consider the relationship between these fractionation factors in terms of the ratio of their natural logarithms:

$${}^{i1,i2,i3}\theta_{a-b} = \frac{\ln({}^{i2/i1}\alpha_{a-b})}{\ln({}^{i3/i1}\alpha_{a-b})}. \quad (3)$$

Logarithms are often used in isotope geochemistry because  $\ln X \approx X - 1$  for  $X$  close to 1, so  $\delta \approx \delta'$  with  $\delta = 1,000(R/R_{\text{standard}} - 1)$  and  $\delta' = 1,000 \ln(R/R_{\text{standard}})$ . An equivalent expression to Equation 3 is

$${}^{i2/i1}\alpha_{a-b} = ({}^{i3/i1}\alpha_{a-b})^{i1,i2,i3}\theta_{a-b}. \quad (4)$$

Measurements of deviations from a reference mass fractionation law are typically presented in per mil  $\Delta$  notation, or the logarithmic analog  $\Delta'$ , so it is useful to express the relationship between  $\Delta'$  and the exponent  $\theta$ :

$${}^{i2/i1}\Delta'_{a-b} (\text{‰}) = 10^3 ({}^{i1,i2,i3}\theta_{a-b} - {}^{i1,i2,i3}\theta_{\text{reference}}) \ln {}^{i3/i1}\alpha_{a-b}, \quad (5)$$

where  ${}^{i2/i1}\Delta'$  is the deviation of the  $i2/i1$  ratio in substance  $a$  relative to what the  $i2/i1$  ratio would be if the  $i2/i1$  and  $i3/i1$  ratios in substance  $b$  were fractionated by a reference mass fractionation law to reproduce the  $i3/i1$  ratio in substance  $a$ , in logarithmic  $\delta$  units. Note that it is common to exclude the denominator isotope  $i1$  from expressions for  $\alpha$ ,  $\delta$ , and  $\Delta$ , but we have included it explicitly to avoid ambiguity. This equation suggests that deviations from an expected mass fractionation exponent will scale with the magnitude of fractionation, and with differences in fractionation exponents—below, we show that these two quantities are not independent, particularly in the case of equilibrium fractionation. Young et al. (2002) adopted the symbol  $\beta$  rather than  $\theta$  to describe this mass law exponent. However, the use of  $\beta$  may cause confusion when discussing reduced partition function ratios in the context of equilibrium isotope fractionation, which are typically labeled  $\beta$  factors.

## 2.2. Mass Fractionation Laws for Equilibrium Isotope Exchange

The mass-dependent partitioning of isotopes at equilibrium is a quantum mechanical effect, chiefly sensitive to the effects of isotope mass on vibrational frequencies in molecules, solids, and liquids. This dependence is evident in the equation most commonly used to calculate the reduced partition function ratio  $(s/s')f$  that gives equilibrium fractionation between a substance and atomic vapor; that is, it is equivalent to  ${}^{i/i'}\alpha_{a-\text{atoms}}$ , often written as  ${}^{i/i'}\beta_a$  and called the  $\beta$  factor (Bigeleisen &

Mayer 1947):

$$\frac{s}{s'} f = \prod_j \frac{u_j e^{-u_j/2} / (1 - e^{-u_j})}{u'_j e^{-u'_j/2} / (1 - e^{-u'_j})}, \quad (6)$$

$$u_j = \frac{h\nu_j}{k_B T}, \quad u'_j = \frac{h\nu'_j}{k_B T},$$

where  $\nu_j$  are the vibrational frequencies ( $u_j$  are called reduced frequencies) of the substance of interest containing one heavy isotope,  $\nu'_j$  are the corresponding vibrational frequencies in the same substance containing a light isotope,  $k_B$  is the Boltzmann constant,  $T$  is absolute temperature, and the series product is over all  $j$  vibrational frequencies. For straight linear molecules (such as  $\text{CO}_2$ ),  $j = 3n - 5$ , where  $n$  is the number of atoms in the molecule; for all other molecules (such as  $\text{H}_2\text{O}$ ), there are  $3n - 6$  frequencies.

The equilibrium fractionation of isotopes  $i$  and  $i'$  between substances  $a$  and  $b$  can then be written as the ratio  $^{i/i'}\alpha_{a-b} = ^{i/i'}\beta_a / ^{i/i'}\beta_b$ . Detailed derivations of this equation and methods of finding approximate solutions were given elsewhere (e.g., Schauble 2004). For present purposes it may suffice to point out that the  $e^{-u/2}$  and  $e^{-u'/2}$  terms describe isotope effects on zero-point (ground state) vibrational energy, whereas the  $(1 - e^{-u})$  and  $(1 - e^{-u'})$  terms describe the effects of excited vibrational states. The  $(u/u')$  terms account for the loss of rotational and translational degrees of freedom when an atom becomes part of a molecule or condensed phase.

This expression, which is widely used in theoretical studies of isotope fractionation, assumes that all molecular vibrations are harmonic, and that there is no coupling between molecular vibration and rotation, so that the total partition function can be written as the product of partition functions for translation, rotation, and vibration. Quanta of molecular rotation are assumed to be closely spaced, relative to thermal kinetic energy, so that the rotational partition function can be written as an integral rather than as a sum over discrete quantum states and eventually made to cancel out of the equation altogether through the Redlich-Teller product rule, which relates moments of inertia to vibrational frequencies. It further assumes that isotope substitution has no direct effect on electronic energies. These simplifications make it possible to estimate equilibrium fractionation factors using only vibrational frequencies as input. The loss of accuracy from these assumptions appears to be small in many natural materials and stable isotope systems, with the exception of D/H fractionation and some other special cases, where anharmonic effects become important (e.g., Richet et al. 1977, Liu et al. 2010, Webb & Miller 2014, Pinella et al. 2015), and for at least some elements with high atomic number (Hg, Tl, U, and likely others), where nuclear field shift effects are significant. The expression also appears to be adequate for understanding equilibrium mass fractionation laws for nonhydrogen elements (Cao & Liu 2011).

### 2.2.1. The canonical equilibrium exponent: a high-temperature limit with broad practical usefulness.

In the limit of relatively high temperatures ( $h\nu/kT \ll 2\pi$ ) (Weston 1999) and modest fractional differences in isotopic vibrational frequencies ( $\nu'/\nu \approx 1$ ), it is possible to extract a further simplified high-temperature (high-T) formula describing equilibrium fractionation from Urey (1947, equation 8) and/or Bigeleisen & Mayer (1947, equations 11b, 17, and 18) that leads to a particularly convenient expression for the mass fractionation law exponent  $\theta$ . This limiting case is of particular interest because one need only know the isotopic masses to calculate  $\theta$ ; the resulting exponent is also surprisingly accurate over a wide range of temperatures and materials (Matsuhisa et al. 1978, Weston 1999, Young et al. 2002). Therefore, the high-T equilibrium  $\theta$  is a useful reference for discussing other mass fractionation laws. A simple derivation of the high-T  $\theta$  is reproduced below.

Adapted to the current notation, Bigeleisen & Mayer's (1947) equations 11*b* and 18 can be combined to yield

$${}^{i2/i1}\beta_a \approx 1 + \frac{b}{96\pi^2 k_B T} \frac{m_{i2} - m_{i1}}{m_{i2} m_{i1}} A, \quad (7)$$

where  $A$  is a sum of spring (force) constants determined by the electronic structure of the material, which is independent of isotopic masses. Because  $(x - y)/xy = (1/y - 1/x)$  and  $\ln(1 + \varepsilon) \approx \varepsilon$ , this leads to

$$\ln {}^{i2/i1}\alpha_{a-b} \approx \left( \frac{1}{m_{i1}} - \frac{1}{m_{i2}} \right) \frac{b}{96\pi^2 k_B T} (A_a - A_b), \quad (8)$$

where  $A_a$  and  $A_b$  are the spring constant sums for substances  $a$  and  $b$ , respectively. Then,

$${}^{i1,i2,i3}\theta_{a-b} = \frac{\ln {}^{i2/i1}\alpha_{a-b}}{\ln {}^{i3/i1}\alpha_{a-b}} \approx \frac{\frac{1}{m_{i1}} - \frac{1}{m_{i2}}}{\frac{1}{m_{i1}} - \frac{1}{m_{i3}}}. \quad (9)$$

This expression is significant because it confirms that the exponents in mass fractionation laws are determined to first order by the masses of the isotopes, and are largely independent of temperature and material properties.

The applicability and accuracy of this expression are surprisingly broad. Matsuhisa et al. (1978) showed that  ${}^{16,17,18}\theta$  stays within 0.008 of the limiting value of 0.5305 for  ${}^{16}\text{O}$ ,  ${}^{17}\text{O}$ , and  ${}^{18}\text{O}$  fractionation between  $\text{CO}_2$  and  $\text{H}_2\text{O}$ , all the way down to 273.15 K, even though (1) several of the significant vibrational terms,  $u$  and  $u'$ , are considerably larger than  $2\pi$  over the lowest part of the temperature range, and (2) the relative mass difference  $(m_{18\text{O}} - m_{16\text{O}})/m_{18\text{O}}m_{16\text{O}}$ , at  $\sim 0.007 \text{ amu}^{-1}$ , is the largest of all elements with three or more stable or long-lived isotopes. The apparent  ${}^{16,17,18}\theta$  value in high-T terrestrial rocks ( $\sim 0.526$ – $0.529$ ) (e.g., Rumble et al. 2007, Pack & Herwartz 2014) is very similar to the high-T limit. The high-T exponent is thus a useful general reference for studies in multiple-isotope systems (e.g., Young et al. 2002). One caveat is that  $\theta$  can take on extreme values in equilibrium fractionations near “crossovers,” where the sign of fractionation between  $a$  and  $b$  changes with temperature (e.g., Skaron & Wolfsberg 1980, Deines 2003) as can be seen in the expression derived by Cao & Liu (2011) from the definitions of  $\theta$ ,  $\beta$ , and  $\alpha$ :

$${}^{i1,i2,i3}\theta_{a-b} = {}^{i1,i2,i3}\theta_{a\text{-atoms}} + \left( {}^{i1,i2,i3}\theta_{a\text{-atoms}} - {}^{i1,i2,i3}\theta_{b\text{-atoms}} \right) \frac{\ln {}^{i3/i1}\beta_b}{\ln {}^{i3/i1}\alpha_{a-b}}, \quad (10)$$

where the equilibrium  $a$ - $b$  fractionation factor appears alone in the denominator of the right-hand term. However, this unbounded behavior of the equilibrium  $\theta_{a-b}$  (at a crossover  $\ln {}^{i3/i1}\alpha_{a-b} \rightarrow 0$ ) does not translate into large deviations in isotope ratios. This is readily seen when the same equation is cast in terms of  $\Delta'$ :

$${}^{i2/i1}\Delta'_{a-b} = 10^3 \left( {}^{i1,i2,i3}\theta_{a\text{-atoms}} \ln {}^{i3/i1}\beta_a - {}^{i1,i2,i3}\theta_{b\text{-atoms}} \ln {}^{i3/i1}\beta_b - {}^{i1,i2,i3}\theta_{\text{reference}} \ln {}^{i3/i1}\alpha_{a-b} \right). \quad (11)$$

This expression makes it clear that even when there is a crossover,  $\Delta'$  converges in a well-behaved way as  $\ln {}^{i3/i1}\alpha$  vanishes, given the limited range of  $\theta_{a\text{-atoms}}$  and  $\theta_{b\text{-atoms}}$  expected at equilibrium.  $\Delta'$  chiefly scales with  $\beta$  values and the variation in their corresponding exponents. In the past 20 years, analytical techniques for several isotope systems have advanced to the point that it is now possible to quantify deviations from this high-T equilibrium exponent. Lower-temperature equilibrium exchange, kinetic processes, mixing, and distillation can all lead to such signatures.

**2.2.2. The low-temperature limit.** As temperature decreases and  $u = bv/(k_B T)$  increases, the assumptions made in the high-T derivation in the preceding section break down, and  $\theta$  varies

with temperature and material. Matsuhisa et al. (1978) noted that  $\theta$  approaches a low-temperature (low-T) limit, realized only at cryogenic conditions for typical materials, which depends solely on the ratio of zero-point energies for the isotopic species of interest. However, a derivation for this relationship is not given by Matsuhisa et al. (1978), so it seems worth providing here. To start, the Bigeleisen & Mayer (1947) reduced partition function ratio equation is simplified by assuming that all  $(1 - e^{-u})$  and  $(1 - e^{-u'})$  terms approach unity as  $u$  and  $u'$  become large. Rotational quanta are assumed to still be small relative to thermal energy. In this case the equation reduces to

$${}^{i2/i1}\beta_a(\text{low-T}) = \prod_j \frac{u_{j(i2)} e^{-u_{j(i2)}/2}}{u_{j(i1)} e^{-u_{j(i1)}/2}}, \quad (12)$$

$$\ln {}^{i2/i1}\beta_a(\text{low-T}) = \sum_j \ln \frac{u_{j(i2)}}{u_{j(i1)}} + \sum_j \frac{u_{j(i1)} - u_{j(i2)}}{2} \quad (13)$$

$$\approx \sum_j \frac{u_{j(i2)} - u_{j(i1)}}{u_{j(i1)}} + \frac{u_{j(i1)} - u_{j(i2)}}{2} \quad (14)$$

$$\approx \sum_j \frac{u_{j(i1)} - u_{j(i2)}}{2}. \quad (15)$$

Canceling the constant factors in the reduced frequencies  $u$  (Equation 6) yields

$${}^{i1,i2,i3}\theta_{a\text{-atoms}} = \frac{\sum_j \nu_{j(i1)} - \sum_j \nu_{j(i2)}}{\sum_j \nu_{j(i1)} - \sum_j \nu_{j(i3)}}. \quad (16)$$

Then  $\theta_{a-b}$  becomes

$${}^{i1,i2,i3}\theta_{a-b} = \frac{\left(\sum_j \nu_{j(i1)} - \sum_j \nu_{j(i2)}\right)_a - \left(\sum_k \nu_{k(i1)} - \sum_k \nu_{k(i2)}\right)_b}{\left(\sum_j \nu_{j(i1)} - \sum_j \nu_{j(i3)}\right)_a - \left(\sum_k \nu_{k(i1)} - \sum_k \nu_{k(i3)}\right)_b}. \quad (17)$$

Cao & Liu (2011) provided an elegant graphical analysis of this relationship using the example of fractionation between diatomic molecules (where there is only a single  $\nu$  for each isotopologue, and isotope effects can be determined by a simple analysis of the reduced mass) and atomic vapor (which lacks vibrations altogether), showing that deviations from the high-T exponent vanish when the bond partner of the isotopically substituted atom is very light, and that they are most significant when the bond partner is much more massive than the isotopically substituted atom. These results can be derived analytically from the low-T exponent equations above, noting that for a diatomic molecule

$$\nu = \frac{1}{2\pi} \sqrt{\frac{\kappa}{\mu}}, \quad (18)$$

where  $\kappa$  is the bond force constant and  $\mu$  is the reduced mass of the diatomic molecule. If the bond partner atom  $Y$  has mass  $m_Y$ , then the vibrational frequencies are determined by

$$\nu_{(i1)} = \frac{\sqrt{\kappa}}{2\pi} \sqrt{\left(\frac{1}{m_Y} + \frac{1}{m_{i1}}\right)}, \quad (19)$$

and so forth for the other isotopes. In the limit where  $m_Y$  is very small relative to the mass of the substituted atom, the approximation

$$\sqrt{z + \varepsilon} \approx \sqrt{z} + \frac{\varepsilon}{2\sqrt{z}} \quad (20)$$



for  $\varepsilon \ll z$  leads to

$$v_{(i1)} - v_{(i2)} \approx \frac{\sqrt{\kappa}}{4\pi} \frac{\frac{1}{m_{i1}} - \frac{1}{m_{i2}}}{\sqrt{\left(\frac{1}{m_Y} + \frac{1}{m_{i1}}\right)}}, \quad (21)$$

and the earlier low-T equilibrium exponent simplifies to

$${}^{i1,i2,i3}\theta_{a-b} \approx \frac{\frac{1}{m_{i1}} - \frac{1}{m_{i2}}}{\frac{1}{m_{i1}} - \frac{1}{m_{i3}}}. \quad (22)$$

This is identical to the high-T expression! Thus nonhydrogen atoms in molecules and solids dominated by bonding to hydrogen atoms (such as oxygen in water vapor) will show very little deviation from the high-T exponent. This convergence likely plays a role in determining the mass fractionation relationship of  $^{16}\text{O}$ ,  $^{17}\text{O}$ , and  $^{18}\text{O}$  in meteoric waters, which is similar to the value found in high-T rock samples ( $\sim 0.528$ ) (e.g., Luz & Barkan 2010). In the other extreme, where  $m_Y$  is much larger than the isotopic masses, all  $1/m_Y$  terms in the square root sign can be neglected, and the mass fractionation exponent becomes

$${}^{i1,i2,i3}\theta_{a\text{-atoms}} \approx \frac{\sqrt{\frac{1}{m_{i1}}} - \sqrt{\frac{1}{m_{i2}}}}{\sqrt{\frac{1}{m_{i1}}} - \sqrt{\frac{1}{m_{i3}}}}. \quad (23)$$

In these limiting cases in the oxygen isotope system, the mass fractionation exponents for reduced partition function ratios (corresponding to fractionation from an atomic vapor) are as follows: high T, 0.5305; low T and light bond partner, 0.5305; low T and massive bond partner, 0.5232. In practice, bond force constants are too small for the low-T, massive-bond partner limit to be reached in elements heavier than hydrogen, except at implausibly cryogenic temperatures. The expected range in natural systems should thus be considerably smaller. Cao & Liu (2011) pointed out that the isotopes of elements more massive than oxygen should typically deviate even less from the high-T equilibrium exponent, because one or both of  $u_{i1}$  and  $m_Y/m_{i1}$  will tend to be small. Indeed, theoretical models of sulfur isotope fractionation generally show a more restricted range of  ${}^{32,33,34}\theta$  in hydrogen sulfide, sulfite, and sulfate away from crossovers (e.g., Farquhar et al. 2003, Otake et al. 2008). This happens even though S–O and S–H bond force constants in these molecules are large, the vibrational frequencies are quite high, and sulfur is still a relatively low-mass element. Sulfur is likely the second or third most promising candidate for variable equilibrium mass fractionation relationships after oxygen and possibly silicon. Deviations in  $\Delta'$  from the high-T equilibrium reference will also decrease strongly at higher  $Z$  because  $\ln(\beta_{a\text{-atoms}})$  decreases, roughly as  $(m_{i2} - m_{i1})/m_{i1}m_{i2}$  (Bigeleisen & Mayer 1947), from  $\sim 100$  at  $25^\circ\text{C}$  for  $^{18}\text{O}/^{16}\text{O}$ ,  $^{30}\text{Si}/^{28}\text{Si}$ , and  $^{34}\text{S}/^{32}\text{S}$  (in sulfate) to  $\sim 20\text{--}30$  for  $^{26}\text{Mg}/^{24}\text{Mg}$  and  $\sim 10$  or less for  $^{44}\text{Ca}/^{42}\text{Ca}$ ,  $^{56}\text{Fe}/^{54}\text{Fe}$ , and most heavier elements. Stated otherwise, because the extent of isotopic fractionation in heavy elements is small, they provide less leverage to distinguish between mass fractionation laws.

Cao & Liu (2011) calculated exponents  $\theta_{a\text{-atoms}}$  ( $\kappa$ , in their notation) using first-principles electronic structure models of isotopic vibrational species in a variety of oxygen-bearing molecules and found that  $\theta$  was in the range  $\sim 0.525\text{--}0.528$  for many species at near-ambient temperatures, except for  $\text{H}_2\text{O}$ , which is close to 0.530 as expected. Barkan & Luz (2012) and Hofmann et al. (2012) subsequently measured deviations of the low-T  $\text{CO}_2\text{--H}_2\text{O}$  fractionation exponent from the high-T limit, finding qualitative agreement (**Figure 1**) with the predictions of Matsuhisa

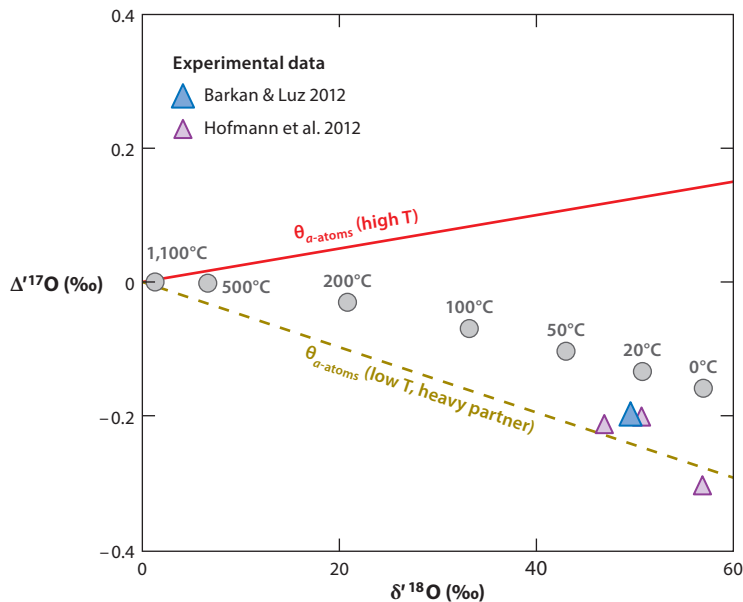


**Figure 1**

Equilibrium  $\text{CO}_2\text{-H}_2\text{O}_{(v)}$  fractionation relative to a 0.528 reference line, using theoretical  $^{16,17,18}\theta$  results from Cao & Liu (2011) and  $^{18/16}\alpha_{\text{CO}_2\text{-H}_2\text{O}}$  from Richet et al. (1977), shown with gray circles. The high-T and the low-T, heavy-bond partner mass fractionation relationships are also shown with solid red and dashed dark yellow lines, respectively. It should be noted that, in general,  $^{16,17,18}\theta$  can fall beyond the extreme high-T and low-T limits of  $^{16,17,18}\theta_{\alpha\text{-atoms}}$ . Experimental data from Barkan & Luz (2012) (*blue triangle*) and Hofmann et al. (2012) (*purple triangles*) indicate a somewhat larger deviation. These have been converted to expected equivalent  $\text{CO}_2\text{-H}_2\text{O}_{(v)}$  fractionations using the  $\text{H}_2\text{O}$  liquid-vapor fractionation data of Barkan & Luz (2005) and (for the Hofmann et al. 2012 results) Horita & Wesolowski (1994).

et al. (1978) and Cao & Liu (2011). Deines (2003), Otake et al. (2008), and Farquhar et al. (2003) performed similar studies for sulfur-bearing molecules, finding a limited but potentially detectable range of exponents  $^{32,33,34}\theta$  and/or  $^{32,36,34}\theta$ .

**2.2.3. Fractionation in mass-dependent potentials: gravity and centrifuges.** Though limited in occurrence in natural terrestrial systems (e.g., air in the interconnected pore space of a snowpack) (Craig et al. 1988, Severinghaus et al. 1996), the gravitational fractionation of isotopes in a stagnant column subject to a mass-dependent potential such as gravity is interesting as a thermodynamically and mathematically simple case, and because it yields the most extreme (lowest, for  $m_{i1} < m_{i2} < m_{i3}$ ) mass fractionation exponent of any mass-dependent process (Ono et al. 2006, Yeung et al. 2012). It is also mathematically similar to the fractionation process in a gas centrifuge, which has significant technological importance. Heavier isotopologues tend to concentrate toward the bottom of a stagnant column, and toward the outer margin of a centrifuge, in order to minimize the potential energy of the system, yielding the relationship

$$\ln^{i2/i1} \alpha_{z1-z2} = \frac{g(m_{i1} - m_{i2})(z1 - z2)}{k_B T}, \quad (24)$$

$${}^{i1,i2,i3}\theta_{z1-z2} = \frac{m_{i1} - m_{i2}}{m_{i1} - m_{i3}}. \quad (25)$$

Here  $z_1$  and  $z_2$  are heights in the column and  $g$  is the acceleration of gravity, and it is assumed that only one atom in each molecule experiences isotope substitution. For  $^{16}\text{O}$ ,  $^{17}\text{O}$ , and  $^{18}\text{O}$  the resulting exponent is 0.50104.

### 2.3. Diffusion and Kinetic Mass Fractionation Laws

Young et al. (2002) provided derivations and equations for the fractionation exponent for Graham's law (pinhole) diffusion:

$${}_{i1,i2,i3}\theta_{\text{diff}} = \frac{\ln\left(\frac{M_{i1}}{M_{i2}}\right)}{\ln\left(\frac{M_{i1}}{M_{i2}}\right)}. \quad (26)$$

Here  $M_{i1}$ ,  $M_{i2}$ , and  $M_{i3}$  are the masses of isotopically substituted molecules. The diffusive exponent is closest to the high-T equilibrium exponent for the case of atomic diffusion ( $M_{i1} = m_{i1}$ ), and diverges (downward if  $m_{i1} < m_{i1} < m_{i3}$ ) as the mass of the diffusing molecule increases (relative to the difference in isotope masses). In the high-molecular mass limit, the exponent approaches the gravitational fractionation exponent. However, the magnitude of overall fractionation also decreases as molecular masses increase. The exponent for atomic diffusion is roughly midway between the exponents for high-T equilibration and gravitational fractionation (or large- $M_{i1}$  diffusion). It should be noted that there is a report of an unusual mass fractionation relationship during thermal diffusion of  $\text{O}_2$  at low pressure (Sun & Bao 2011), and that the mass fractionation relationships for thermal diffusion and diffusion through dense phases are not yet as well understood as those for simple diffusion in the vapor phase.

Young et al. (2002) also considered a special case of the transition state theory (TST) of chemical kinetics, which describes activation energy-limited kinetic isotope fractionation. Young et al. (2002) further assumed that fractionation is dominated by the motion of atoms along a reaction coordinate, neglecting isotope effects on the activation energy:

$${}_{i1,i2,i3}\theta_{\text{TST}} = \frac{\ln\left(\frac{H_{i1}^*}{H_{i2}^*}\right)}{\ln\left(\frac{H_{i1}^*}{H_{i2}^*}\right)}. \quad (27)$$

Here the mass term is more complex, because multiple atoms in the reactant molecule(s) may be moving in the activation process; in TST this complex motion along the reaction coordinate is modeled as if it were a special vibrational mode with a negative force constant (and thus an imaginary vibrational frequency), with a corresponding reduced mass. Reactions where the isotope effect on activation energies dominates (i.e., where the substituted atom does not move vigorously along the reaction coordinate but does participate in bonds that strain, reorganize, form, or break during activation) are expected to more closely follow the relationships given above for equilibrium fractionation. In general, when  $m_{i1} < m_{i1} < m_{i3}$ , kinetic fractionation exponents are smaller than the canonical high-T equilibrium exponent (**Figure 2**).

### 2.4. Effects of Mixing and Distillation

In addition to providing derivations for equilibrium and kinetic fractionation mass fractionation law exponents, Young et al. (2002) noted that back reaction and cyclic reaction networks can combine to generate apparent mass fractionation relationships that diverge from those of the underlying elementary reactions. They focused on the oxygen isotope system in atmospheric  $\text{O}_2$ ,

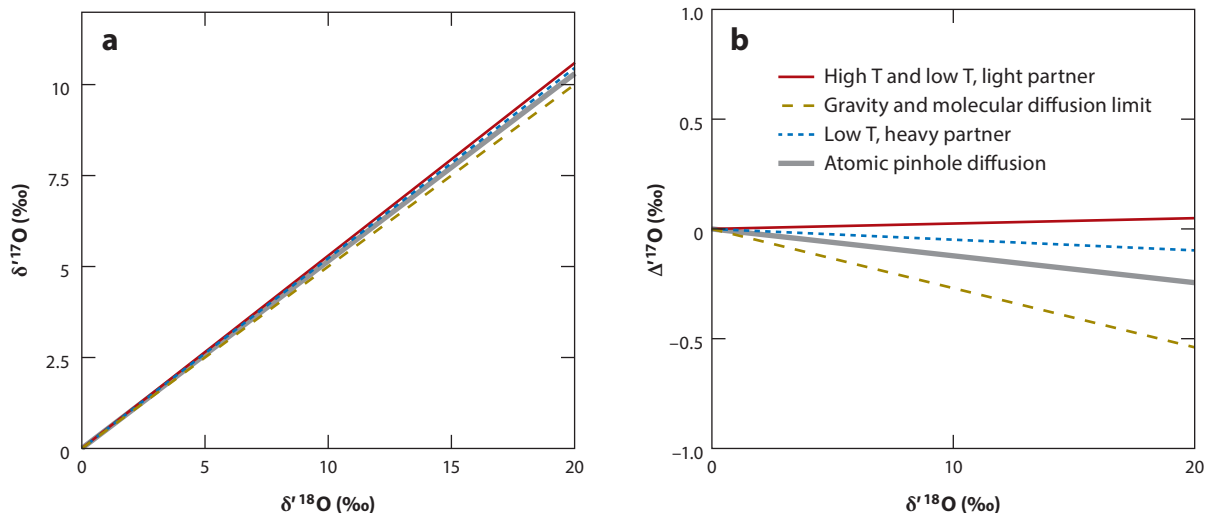


**Figure 2**

Mass fractionation relationships  $^{16,17,18}\theta_{a-b}$  for different elementary reaction types, acting in the oxygen isotope system ( $^{16}\text{O}$ ,  $^{17}\text{O}$ ,  $^{18}\text{O}$ ). Substance  $a$  is assumed to have  $\delta^{17}\text{O}$  and  $\delta^{18}\text{O}$  equal to zero, and  $10^3 \ln(^{18/16}\alpha_{a-b})$  is varied from 0‰ to 20‰. (a)  $\delta^{17}\text{O}$  versus  $\delta^{18}\text{O}$ . (b)  $\Delta^{17}\text{O}$  versus  $\delta^{18}\text{O}$ , against a reference exponent of 0.528.

but similar phenomena will have (usually more subtle) effects in other systems as well. Even simple mixing between two gas reservoirs will lead to variable apparent mass fractionation relationships, because of the slight difference between conventional  $\delta$  notation (in which all mixing lines are linear in the  $\delta^{i2/i1}$  versus  $\delta^{i3/i1}$  plane, but fractionations of varying  $^{i3/i1}\alpha$  at a given  $\theta$  form curved arrays) and logarithmic  $\delta$  notation (in which mixing lines are curved, but  $^{i3/i1}\alpha$  values at constant  $\theta$  will fall along a single straight line).

Similarly, distillation processes such as Rayleigh fractionation can lead to apparent mass fractionation exponents that differ from the  $^{i1,i2,i3}\theta$  value of the instantaneous fractionation process. This distinction has led to the introduction of the notation  $^{i1,i2,i3}\lambda$  to distinguish empirically observed  $\delta^{i2/i1}$  versus  $\delta^{i3/i1}$  slopes from mechanistically defined  $^{i1,i2,i3}\theta$  exponents (Miller 2002, Angert et al. 2003). A roughly analogous distinction between empirical, or effective, exponents and mechanistic exponents is also made in the alternative  $\beta$  notation descended from the work of Young et al. (2002). The field of isotope geochemistry is already rich in notations, and we only use  $\theta$  to denote slopes in three-isotope diagrams, whether they are empirically or mechanistically derived. As a word of caution, because processes like mixing or distillation can influence the apparent mass fractionation relationships, one cannot write mass-balance equations for  $\Delta'$  in the same manner as is done for  $\delta$  or  $\delta'$  (Miller 2002, Young et al. 2002, Assonov & Brenninkmeijer 2005, Ono et al. 2006, Tang & Dauphas 2012).

## 2.5. Mass Fractionation and Mass Spectrometry

To study radiogenic ingrowth or nucleosynthetic anomalies, one has to correct for stable isotopic fractionation. This is most often done by a combination of standard measurements performed under the same conditions as the samples and mass fractionation correction by internal normalization. When studying mass fractionation in natural systems, emphasis is put on understanding the processes at play, which are sometimes associated with specific mass fractionation laws. In

general, many processes can affect measured isotopic compositions, including isotopic fractionation imparted by natural processes, chromatographic separation, and mass spectrometry. Various empirical laws have been used for correcting for such mass fractionation. The exponential law is commonly encountered in thermal ionization mass spectrometry (TIMS) (Russell et al. 1978, Hart & Zindler 1989), multicollector inductively coupled plasma mass spectrometry (MC-ICPMS) (Maréchal et al. 1999), and secondary ionization mass spectrometry (SIMS) (Fahey et al. 1987a,b). It relates the measured isotopic ratio to the “true” ratio through

$$\left(\frac{i2}{i1}\right)_{\text{measured}} = \left(\frac{i2}{i1}\right)_{\text{“true”}} \left(\frac{m_{i2}}{m_{i1}}\right)^b, \quad (28)$$

where  $b$  is a free parameter (it is often written as  $\beta$ , but we have avoided this notation to prevent any confusion with the reduced partition function ratio in Equation 6). Connecting this equation to the formalism given above (Equation 3), we have for the exponential law

$${}_{i1,i2,i3}\theta_{\text{measured-“true”}} = \frac{\ln m_{i2} - \ln m_{i1}}{\ln m_{i3} - \ln m_{i1}}. \quad (29)$$

Maréchal et al. (1999) introduced another empirical law (the generalized power law) that encompasses most mass fractionation laws used for internal normalization:

$$\left(\frac{i2}{i1}\right)_{\text{measured}} = \left(\frac{i2}{i1}\right)_{\text{“true”}} g^{m_{i2}^n - m_{i1}^n}, \quad (30)$$

where  $g$  and  $n$  are two free parameters. When  $n \rightarrow 0$ , the limit of this law is the exponential law discussed above. Connecting this equation to the formalism of Equation 3, we have

$${}_{i1,i2,i3}\theta_{\text{measured-“true”}} = \frac{m_{i2}^n - m_{i1}^n}{m_{i3}^n - m_{i1}^n}. \quad (31)$$

A virtue of this law is that it does capture much of the mass dependences obtained based on first-principles considerations (Wombacher & Rehkämper 2003;  $n = -1$  gives Equations 9, 22;  $n = -1/2$  gives Equation 23;  $n = 1$  gives Equation 25;  $n \rightarrow 0$  gives Equation 27).

The manner in which internal normalization is applied is to fix one (or two for the generalized power law) isotopic ratio ( $i3/i1$  hereafter) to an assumed “true” value to calculate the parameters of the mass fractionation law. In the commonly used exponential law,  $b$  is given by

$$b = \frac{\ln(i3/i1)_{\text{measured}} - \ln(i3/i1)_{\text{“true”}}}{\ln m_{i3} - \ln m_{i1}}. \quad (32)$$

The  $i2/i1$  ratio corrected for mass fractionation by internal normalization is thus given by

$$\ln\left(\frac{i2}{i1}\right)_{\text{corrected}} = \left(\frac{i2}{i1}\right)_{\text{measured}} - \left[ \ln\left(\frac{i3}{i1}\right)_{\text{measured}} - \ln\left(\frac{i3}{i1}\right)_{\text{“true”}} \right] \frac{\ln m_{i2} - \ln m_{i1}}{\ln m_{i3} - \ln m_{i1}}. \quad (33)$$

If one uses an inappropriate law to correct for mass fractionation, this can create apparent anomalies (also called second-order fractionation). Two telltale signatures of inadequate mass fractionation correction are (1) correlations of apparent anomalies with the degree of isotopic fractionation and (2) correlations between apparent anomalies for various isotopes. Tang & Dauphas (2012) examined those two aspects using the formalism of the generalized power law. If one corrects isotopic fractionation using the generalized power law with exponent  $k$  while the true fractionation exponent is  $n$ , then the apparent anomaly in  $i2/i1$  (in  $\varepsilon$  units, the deviation between the corrected and the “true” isotopic ratios in parts per  $10^4$ ) is

$$\varepsilon_{i2/i1} = 5(n - k)(m_{i2}/m_{i1} - 1)(m_{i2} - m_{i3})F, \quad (34)$$

where  $F$  is the degree of isotopic fractionation in ‰ amu<sup>-1</sup>. If one considers another ratio  $i4/i1$ , also corrected for mass fractionation by internal normalization, then the apparent anomalies will correlate through (note that  $n$  and  $k$  are not present in this equation)

$$\varepsilon_{i2/i1} = \frac{(m_{i2} - m_{i1})(m_{i2} - m_{i3})}{(m_{i4} - m_{i1})(m_{i4} - m_{i3})} \varepsilon_{i4/i1}. \quad (35)$$

The choice of which mass fractionation law to use influences <sup>60</sup>Fe-<sup>60</sup>Ni systematics in chondrules from CB chondrites (Tang & Dauphas 2012) and <sup>26</sup>Al-<sup>26</sup>Mg systematics in refractory inclusions (Davis et al. 2015). Second-order mass fractionation corrections have also been applied in mass spectrometry in Cr (Lugmair & Shukolyukov 1998), Nd (Caro et al. 2003), and W (Touboul & Walker 2012) high-precision isotope measurements.

## 2.6. Emerging Use of Mass Fractionation Laws in Geochemistry

As technical improvements have increased the precision of isotope ratio measurements, potential applications of measuring variations in mass fractionation exponents have emerged. So far, these studies have been mainly limited to oxygen, sulfur, and magnesium, the three lowest-mass three- and four-isotope systems (e.g., Young et al. 2002, Deines 2003, Farquhar et al. 2003, Ono et al. 2006, Rumble et al. 2007, Levin et al. 2014, Pack & Herwartz 2014, Passey et al. 2014).

**2.6.1. The hydrological cycle.** Earth's hydrological cycle is among the most intensive subjects for study of variations in mass fractionation laws and of how they may be distinguished from mass-independent signatures inherited from other atmospheric species. An in-depth discussion is beyond the scope of the present review, so an abbreviated introduction is given here. Luz & Barkan (2000) first noted differences between the high <sup>16,17,18</sup>θ value, of ~0.529, characteristic of equilibrium evaporation and condensation and the lower <sup>16,17,18</sup>θ value found in evaporation to undersaturated air. Meijer & Li (1998), Landais et al. (2008), Luz & Barkan (2010), Uemura et al. (2010), and others have subsequently reported high-precision <sup>17</sup>O/<sup>16</sup>O and <sup>18</sup>O/<sup>16</sup>O measurements of water samples including water vapor in air, meteoric waters, ice cores, and seawater. These studies find well-defined δ<sup>17</sup>O/δ<sup>18</sup>O slopes of 0.528 for meteoric waters and ice, slightly offset and <sup>17</sup>O enriched (by ~0.04‰) relative to a seawater array with the same mass fractionation exponent. Seawater is found to be much more similar to the Vienna Standard Mean Ocean Water (VSMOW) standard (δ<sup>17</sup>O<sub>seawater</sub> ≈ -0.005‰). Luz & Barkan (2010) argued that the slight <sup>17</sup>O/<sup>16</sup>O enrichment in meteoric waters relative to seawater is a signature of disequilibrium fractionation of oxygen isotopes when liquid water evaporates into undersaturated air, and they were able to produce a similar signature in open-pan evaporation experiments. They further found that normal condensation processes have at most a weak effect on the <sup>17</sup>O excess, whereas crystallization of ice from very cold, supersaturated Antarctic air leads to a marked diminution of the <sup>17</sup>O excess, and highly evaporated lake waters also show lowered δ<sup>17</sup>O. These observations are consistent with a low, disequilibrium effective <sup>16,17,18</sup>θ for kinetically hindered phase changes far from equilibrium saturation conditions. The systematics point to potential uses of <sup>17</sup>O/<sup>16</sup>O measurements to constrain humidity in water-vapor sources or ancient precipitation preserved in ice core samples (e.g., Landais et al. 2008, 2012).

**2.6.2. O<sub>2</sub> in the troposphere.** Young et al. (2002) noted that mass fractionation laws for kinetic and equilibrium processes were distinct, with diffusive kinetic laws generally giving smaller exponents than the high-T limit of equilibrium fractionation. This led the authors to propose that θ values characteristic of selected suites of samples could be used to constrain the nature of the

fractionating process. They further showed that complex processes of mixing, reaction, and back reaction could affect apparent exponents and lead to  $\Delta'$  deviations. Angert et al. (2003) observed that the fractionation exponent associated with respiration of  $O_2$  ( $\sim 0.506$ – $0.516$ ) was substantially lower than in typical high-T and hydrological data sets, which cluster at values slightly lower than the high-T equilibrium limit ( $0.526$ – $0.529$  versus  $0.5305$ ). Because  $O_2$  respiration is the dominant cause of the Dole effect—i.e., the high  $\delta^{18}O$  of  $O_2$  in air relative to natural waters—the low  $^{16,17,18}\theta$  of respiration likely contributes significantly to the negative  $\Delta'^{17}O$  observed in air (Young et al. 2014).

**2.6.3. Paleoenvironment and provenance of chemical sediments.** The theoretical study of variations in  $^{16,17,18}\theta$  in molecules and molecular analogs for silicate and carbonate minerals by Cao & Liu (2011) has triggered interest in using highly precise  $\Delta'^{17}O$  measurements of sedimentary minerals to investigate the conditions of their formation. Levin et al. (2014), Pack & Herwartz (2014), and Passey et al. (2014) have recently reported systematic deviations of  $\Delta'^{17}O$  in low-T silicate and carbonate precipitates. Because  $^{16,17,18}\theta_{H_2O-atoms}$  closely approximates the high-T limit at ambient temperatures, the equilibrium  $\Delta'^{17}O$  value in crystals comprising chemical sediments will depend mainly on  $^{16,17,18}\theta_{mineral-atoms}$  and  $^{18}\beta_{mineral}$  (Cao & Liu 2011), and signatures in field samples will likely reflect a combination of the temperature of deposition, disequilibrium steps in the precipitation reaction, and the  $\Delta'^{17}O$  value of precipitating fluids. These dependencies suggest that it will be possible to obtain information that is complementary to established paleothermometers based on  $\alpha_{mineral-H_2O}$  versus temperature calibrations as well as to the recently developed  $^{13}C$ - $^{18}O$  clumped-isotope technique for carbonate minerals (e.g., Ghosh et al. 2006).

**2.6.4. Sulfur biogeochemistry.** Hulston & Thode (1965) established the theoretical and empirical mass fractionation exponents for sulfur. More recent high-precision analyses of  $^{33}S/^{32}S$  and even  $^{36}S/^{32}S$  ratios opened up the possibility of looking for small differences between samples with sulfur that has undergone isotopic partitioning via inorganic processes versus biological pathways. Farquhar et al. (2003) explored these possibilities using theory, experiments, and process-based modeling, proposing distinct mass fractionation relationships for components of biologically mediated dissimilatory sulfate reduction relative to the disproportionation of intermediate species in metastable oxidation states. Experimental sulfate reduction with *Archaeoglobus fulgidus* could be explained with a normal equilibrium  $^{32,33,34}\theta$  value of approximately 0.515. Relationships between bio(geo)chemical reaction networks, intrinsic fractionation mechanisms, and observed mass fractionation effects were explored further in subsequent papers (e.g., Ono et al. 2006, Johnston et al. 2008).

**2.6.5. Adsorption/condensation reactions.** Eiler et al. (2014) found an anomalously high  $^{32,33,34}\theta$  value of  $\sim 0.55$  (compared to 0.515 for the high-T equilibrium limit) during batch equilibration of  $SF_6$  between vapor and solid at temperatures of 137–173 K in laboratory experiments. In this temperature range, the solid has slightly lower  $^{33}S/^{32}S$  and  $^{34}S/^{32}S$  ratios than the vapor, likely because the strong intramolecular S–F bonds in the vapor weaken slightly as intermolecular F–F bonding interactions strengthen in the crystal. They explained the anomalous  $^{32,33,34}\theta_{crystal-vapor}$  in terms of a near-crossover relationship, with the condensed phase showing a slightly higher  $^{32,33,34}\theta_{crystal-atoms}$  because of the influence of lower-frequency (low- $u$ ) intermolecular vibrations, coupled to the small  $^{34/32}\alpha$  of both the vapor and crystalline phases (e.g., Skaron & Wolfsberg 1980).

### 3. MASS-INDEPENDENT FRACTIONATIONS IN OXYGEN AND SULFUR: WHERE THE WILD THINGS ARE

The oxygen and sulfur isotope systems have the most intensively studied and dramatic mass-independent chemical isotope fractionations of any elements. Prominent mass-independent fractionation phenomena in these systems are found in primitive meteoritic materials (e.g., Clayton et al. 1973), in ozone in the terrestrial stratosphere (e.g., Mauersberger 1987), and in sulfur extracted from ancient (2.4 Ga or older) terrestrial sediments (Farquhar et al. 2000). Although the mechanisms behind each of these prominent mass-independent fractionation signatures are not yet fully understood, the most widely favored hypotheses are that both the meteoritic oxygen isotope anomaly and the Archean–earliest Proterozoic sulfur isotope anomaly originate from abundance-dependent photochemical fractionation effects, in particular the phenomenon of self-shielding, whereas the oxygen isotope signature of stratospheric ozone is controlled by an isotope effect on the lifetimes of newly formed, vibrationally and rotationally excited ozone molecules. Each of these topics is the focus of ongoing, intensive study, and each has been the topic of recent reviews elsewhere (e.g., Thiemens 2006, Young et al. 2008, Johnston 2011, Thiemens et al. 2012). They are summarized only briefly here.

#### 3.1. Anomalous Oxygen Isotopes in Meteorites

In a study of mineral separates from meteorites, Clayton et al. (1973) discovered that refractory minerals from carbonaceous chondrites showed dramatically different  $^{17}\text{O}/^{16}\text{O}$  and  $^{18}\text{O}/^{16}\text{O}$  ratios relative to terrestrial rocks and samples from other rocky bodies in the Solar System, with depletions of up to 35‰ in both ratios. The range of variation has been extended to  $\delta^{17}\text{O} \approx \delta^{18}\text{O} \approx -75\text{‰}$  [relative to Standard Mean Ocean Water (SMOW); Earth has  $\delta^{17}\text{O} \approx +3\text{‰}$  and  $\delta^{18}\text{O} \approx 6\text{‰}$  on the same scale] by subsequent measurements of calcium-aluminum-rich inclusions (CAIs; millimeter- to centimeter-size inclusions that are found in chondrites and are made of ceramic-like refractory minerals), meteoritic hibonite grains, and a chondrule-like sample of the Acfer 214 chondritic meteorite (Kobayashi et al. 2003, Liu et al. 2009). Complementary, highly  $^{17}\text{O}$ - and  $^{18}\text{O}$ -enriched samples from the aqueously altered matrix of the Acfer 094 chondrite have also been measured, with  $\delta^{17}\text{O}$  and  $\delta^{18}\text{O}$  up to +180‰ (Sakamoto et al. 2008). Most remarkably, these fractionations fall along a  $\delta^{17}\text{O}$  versus  $\delta^{18}\text{O}$  array with a slope of one, contrary to the slope of  $\sim 0.50$ – $0.53$  for mass-dependent chemical fractionation processes such as those documented in terrestrial waters and rocks (and within some families of meteorites, as well as the Moon). The magnitude of fractionation and the unusual mass fractionation relationships in these samples were unmatched until the discovery a decade later of mass-independent fractionation of ozone toward  $^{16}\text{O}$ -depleted compositions in Earth's stratosphere (Mauersberger 1987). Initially, Clayton et al. (1973) proposed that the  $^{16}\text{O}$ -enriched,  $^{17}\text{O}$ - and  $^{18}\text{O}$ -depleted compositions of refractory minerals in carbonaceous chondrites were due to the presence of an exotic component with a distinct nucleosynthetic history that did not fully mix before the refractory grains condensed. This explanation predicts that oxygen in Earth, the Moon, Mars, and bulk meteorites, which are much more uniform in composition, represents the homogenized solar nebular composition and that the grains are anomalous. It is now known that the oxygen isotope composition of the Sun closely resembles the composition of refractory meteoritic inclusions with the most extreme isotopic compositions ( $\delta^{17}\text{O} \approx \delta^{18}\text{O} \approx -70\text{‰}$  relative to bulk Earth) (McKeegan et al. 2011) (Figure 3), and that presolar oxide grains rarely contain oxygen with the  $^{16}\text{O}$ -rich compositions required to explain the 1:1 oxygen isotope variations (e.g., Nittler et al. 1994). The prevailing view now is that the slope-one line is not nucleosynthetic in origin, but instead reflects a chemical process in the solar nebula, or perhaps in a molecular cloud environment: isotope fractionation



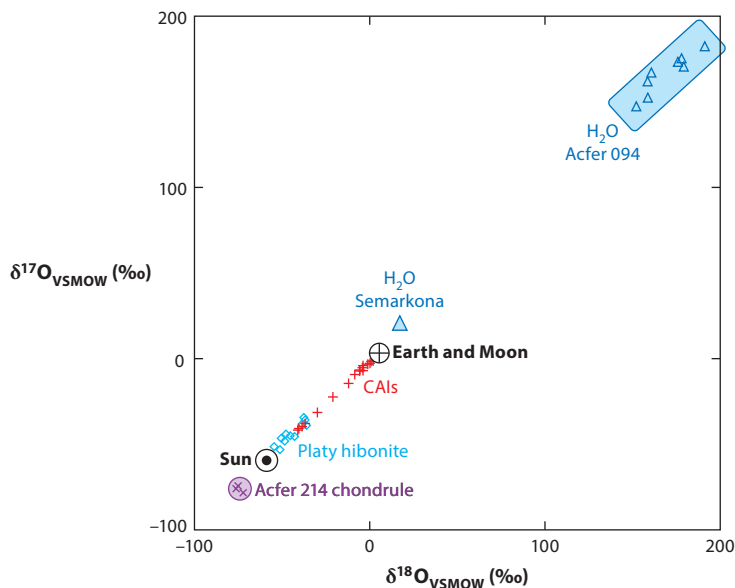


**Figure 3**

Oxygen isotope compositions of Solar System materials. Data for the Sun are from McKeegan et al. (2011), CAI data are from Young & Russell (1998), platy hibonite analyses are from Liu et al. (2009), and data for the very  $^{16}\text{O}$ -enriched Acfer 214 chondrule are from Kobayashi et al. (2003). Data for  $^{16}\text{O}$ -depleted meteoritic waters are from Sakamoto et al. (2008) and Choi et al. (1998). At this scale, the compositions of martian meteorites and ordinary chondrites are hidden behind the Earth and Moon symbols, even though they are measurably distinct (e.g., Clayton et al. 1976, Franchi et al. 1999). Abbreviations: CAI, calcium-aluminum-rich inclusion; VSMOW, Vienna Standard Mean Ocean Water.

in the photochemical destruction of carbon monoxide by far-UV light (Clayton 2002, Yurimoto & Kuramoto 2004, Lyons & Young 2005). Chemical fractionation processes involving dust grain surfaces and/or SiO vapor have also been proposed (e.g., Marcus 2004, Chakraborty et al. 2013). In the nebular CO self-shielding process, oxygen liberated by photochemical destruction of CO is thought to react with residual nebular material, eventually forming a 1:1  $^{17}\text{O}/^{16}\text{O}$  and  $^{18}\text{O}/^{16}\text{O}$  enriched reservoir, possibly through the formation of  $\text{H}_2\text{O}$  from photolysed CO and subsequent water-rock interactions. Self-shielding of UV photons by CO molecules has long been thought to be a cause of isotopic variation of CO in molecular clouds (e.g., Bally & Langer 1982). Variations in the isotopic composition of CO around the protostellar disk in VV CrA, which are consistent with nebular self-shielding, have also been observed astronomically (Smith et al. 2009). Self-shielding is a fractionating process that can occur when a parcel of material subject to photodissociation is optically thick, so that a significant fraction of the incoming photons at dissociating energies are absorbed before passing through the fractionating reservoir. Photons that react with the most common isotopologues will be absorbed most strongly, whereas photons that preferentially react with rare isotopologues will penetrate more deeply. For CO, in the (unrealistic) limit of perfect energy separation for reactive photons for each isotopologue, uniform intensity of photons over the relevant energy range, unit quantum yield, complete absorption at very high optical depth, and a high ratio of reactant to product, each isotopologue will photodissociate at the same absolute rate, and all isotopic ratios of the products will approach unity (i.e.,  $^{17}\text{O}/^{16}\text{O} \approx ^{18}\text{O}/^{16}\text{O} \approx ^{13}\text{C}/^{12}\text{C} \approx 1$ ). At intermediate optical depths, or in the presence of nonreactive, broad-spectrum absorbers or

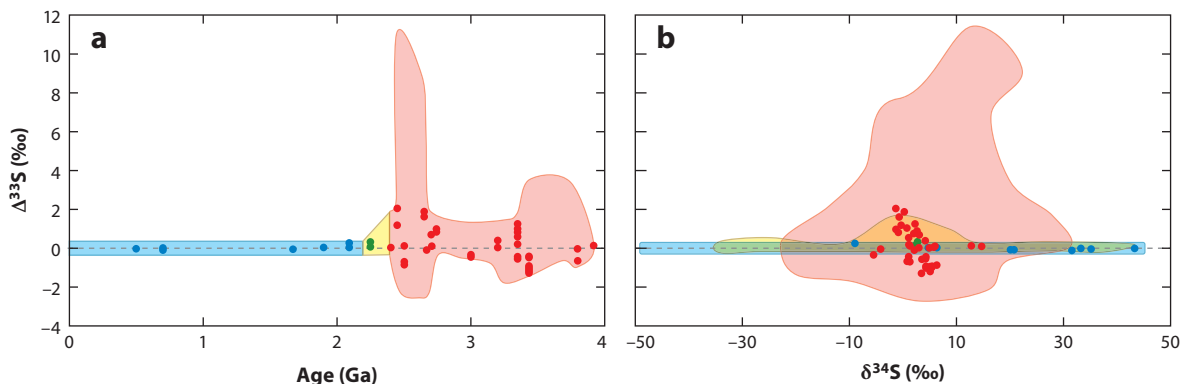


**Figure 4**

Mass-independent fractionation signatures in terrestrial sulfate and sulfide samples. Data points are from the discovery paper (Farquhar et al. 2000), with expanded envelopes to show the range in data collected subsequently (Johnston 2011 and references therein). (a)  $\Delta^{33}\text{S}$  versus sample age; (b)  $\Delta^{33}\text{S}$  versus  $\Delta^{34}\text{S}$ . Data and data envelopes are shown in red for samples 2.4 Ga and older, in green and yellow for 2.2–2.4 Ga samples, and in blue for <2.2 Ga samples.

scatterers such as dust, the reaction probabilities for photodissociation events involving rare isotopologues may be small enough that their relative contribution to the reaction products will be similar to the reactant composition, whereas common isotopologues will be partially shielded from reaction due to their greater effective optical depth for dissociating photons. This idealized intermediate case will give rise to a 1:1 mass fractionation relationship enriching rare isotopes in the reaction products. Realistic modeling of self-shielding effects must take account of overlap between the reactive photon energies of different isotopologues, variations in optical thickness across the reacting mass, and other complications (Lyons & Young 2005), as well as the details of the photochemical mechanism itself (e.g., Chakraborty et al. 2012), and these are topics of active study.

### 3.2. Mass-Independent Fractionation of Sulfur Isotopes

Although Hulston & Thode (1965) found that  $^{33}\text{S}/^{32}\text{S}$  and  $^{34}\text{S}/^{32}\text{S}$  ratios in most terrestrial and meteoritic samples closely follow a single mass fractionation line, Farquhar et al. (2000) discovered that terrestrial samples of sulfide and sulfate minerals formed near Earth's surface in the Archean and earliest Proterozoic eons before 2.4 Ga exhibit pronounced mass-independent fractionation signatures (Figure 4). They were able to reproduce similar fractionations by exposing sulfur-bearing molecules in the vapor phase to UV photons energetic enough to drive photochemical breakdown. The most likely candidate reactant for the Archean fractionation reaction is sulfur dioxide ( $\text{SO}_2$ ), and the fractionating mechanism is thought to be an atmospheric self-shielding process similar to the nebular process proposed for CO (Farquhar et al. 2001, Lyons 2007). Sulfur gases, including  $\text{SO}_2$ , are very rare and generally short lived in the modern oxidizing atmosphere of Earth, and the surficial sulfur reservoir is dominated by sulfate and sulfide in solution and chemical sediments. The modern stratosphere's ozone layer also strongly absorbs UV light, greatly attenuating photochemical breakdown of sulfur species in most of the atmosphere. More detailed chemical arguments, experiments, and reaction modeling (e.g., Farquhar et al. 2000, 2001; Pavlov & Kasting 2002) indicate that the strong signature of  $\text{SO}_2$  self-shielding observed in Archean sulfate and sulfide can only occur in an atmosphere in which  $\text{O}_2$  is a trace gas ( $p\text{O}_2 \approx 10^{-5}$  bar or less). The Archean sulfur isotope record, and the disappearance of the mass-independent signature after

this epoch, thus provides key evidence that the first appearance of O<sub>2</sub> as a significant component of air occurred at ~2.4 Ga. Mass-independent fractionation of sulfur in modern environments has also been noted, related to sulfate aerosols lofted to the stratosphere by extremely large volcanic eruptions (e.g., Savarino et al. 2003, Baroni et al. 2007, Bindeman et al. 2007, Martin & Bindeman 2009).

### 3.3. Mass-Independent Fractionation of Ozone in Earth's Stratosphere

Mass-independent fractionation of ozone (O<sub>3</sub>) was first observed in laboratory synthesis experiments using an electric discharge (Heidenreich & Thiemens 1986). In these experiments O<sub>3</sub> is enriched in <sup>17</sup>O and <sup>18</sup>O, with  $\delta^{17}\text{O} \approx \delta^{18}\text{O}$  up to +30‰ depending on the gas pressure and the presence of an inert gas. A similar signature of ozone in the stratosphere was first tentatively observed in balloon-collected samples by Mauersberger (1987), and it is now known that stratospheric ozone can show enrichments in <sup>17</sup>O- and <sup>18</sup>O-bearing molecules of 100‰ and more, with mass-49 (<sup>17</sup>O-bearing) and mass-50 (mostly <sup>18</sup>O-bearing) enrichments following a roughly 1:1 relationship (e.g., Schueler et al. 1990). This unusual isotopic signature influences the isotopic composition of the O<sub>2</sub> residue and is transferred to other molecules in the stratosphere through exchange reactions, leading to mass-independent signatures in several tropospheric molecular species, such as O<sub>2</sub> and CO<sub>2</sub> (Yung et al. 1991, Luz et al. 1999, Lyons 2001, Luz & Barkan 2010).

Unlike in meteoritic oxygen and Archean sulfur, the mass-independent fractionation in ozone is thought to stem mainly from the formation reaction (Morton et al. 1990). Photolysis reactions are likely to be secondary in importance (Krankowsky et al. 2007). When O<sub>2</sub> and O atom react to form ozone, the O<sub>3</sub> product molecule is initially highly excited vibrationally and rotationally, with enough energy to dissociate back into the reactant state. Stabilization of the product depends on inelastic collisions with other molecules (typically N<sub>2</sub>, in the case of air) that remove enough energy to prevent dissociation. The net formation rate of ozone thus depends critically on the intrinsic dissociation lifetime of newly formed ozone molecules, relative to the rate of collision with other molecules. Substitution of <sup>17</sup>O or <sup>18</sup>O into an ozone molecule strongly affects the dissociation lifetime, and the location of rare isotopes on the central or distal position of the ozone molecule is also important (e.g., Mauersberger et al. 1999). These considerations lead ozone to have high <sup>17</sup>O/<sup>16</sup>O and <sup>18</sup>O/<sup>16</sup>O ratios relative to atomic and molecular oxygen. The effect diminishes at high gas pressure (where collision rates with surrounding molecules become large and lifetime differences are less important). In detail, however, quantitatively reproducing laboratory experiments and environmental isotopic signatures with theoretical models has proven difficult (e.g., Gao & Marcus 2002), and studies are ongoing.

Apparent mass-independent  $\Delta^{17}\text{O}$  signatures in oxygen, derived from the fractionation of stratospheric ozone and from tropospheric chemical processes with varying mass fractionation exponents due to photosynthesis and respiration (e.g., Angert et al. 2003, Young et al. 2014), are of interest as tracers of oxygen in the ambient environment. For instance, Luz et al. (1999) proposed the use of  $\Delta^{17}\text{O}$  measurements to track photosynthetic productivity. More recently,  $\Delta^{17}\text{O}$  in chemical sediment and biominerals has been used as a proxy for atmospheric CO<sub>2</sub> abundance, tracking the O<sub>3</sub>-CO<sub>2</sub> exchange process (Bao et al. 2008, Pack et al. 2013).

## 4. CHEMICAL ISOTOPE EFFECTS DRIVEN BY PROPERTIES OTHER THAN MASS

The isotopic nuclei of a given element typically vary in size (i.e., the positive charges occupy different volumes of space), and nuclei with odd numbers of neutrons and/or protons also exhibit

magnetic moments and nonspherical shapes. In principle, these properties should lead isotopes to react at different rates, and to partition unequally between coexisting phases or species at equilibrium. Compared to isotopic abundance variations caused by differences in isotopic mass, however, these non-mass-dependent phenomena are little studied and poorly understood. In fact there is not an accepted term to describe these effects, because the term mass-independent fractionation has come to refer to any isotope effect that does not scale in *proportion* to mass differences in isotopes, and it usually describes phenomena where the underlying mechanism does in fact depend mainly on isotopic mass (e.g., ozone formation and self-shielding of O and S species). In atomic physics, the effects of nuclear size and shape on emission and absorption spectra are grouped together as nuclear field shift effects, distinguished from the effects of mass and hyperfine structure; field shift isotope fractionations were originally proposed for uranium (Bigeleisen 1996a, Nomura et al. 1996) and strontium (Nishizawa et al. 1995). Magnetic isotope effects are thought to occur in disequilibrium reactions where spin-forbidden pathways can be accessed by interactions between the spins of unpaired electrons and nuclei with nonzero magnetic moments (e.g., Buchachenko 1995, 2013); this mechanism is the leading candidate to explain large mass-independent fractionations observed in terrestrial mercury samples (Bergquist & Blum 2007). This section discusses recent progress in measuring and understanding isotope effects that depend on properties other than isotopic mass differences, with a particular focus on the field shift effect.

#### 4.1. Magnetic Isotope Effects

Isotope effects that depend on nuclear magnetic moments have been described in the chemistry literature, typically affecting organic reactions that form radical ion pairs as an intermediate step. These phenomena have been reviewed elsewhere (e.g., Turro 1983; Gould et al. 1984; Buchachenko 1995, 2013). In contrast to the field shift effect, which acts both at equilibrium and in kinetically hindered reactions (by changing activation energies, in the latter case), magnetic effects are purely kinetic, affecting the rates of formation and branching ratios of possible reaction products. Although there are scattered reports of magnetic isotope effects in laboratory experiments on oxygen- and sulfur-bearing compounds (e.g., Oduro et al. 2011), interest in magnetic isotope effects increased with the discovery of large mass-independent fractionation signatures in mercury, particularly in samples of biological tissues, and their reproduction in experiments in which Hg(II) species are photochemically reduced to elemental form (Bergquist & Blum 2007). Mass-independent fractionation of mercury has recently been reviewed in this journal (Blum et al. 2014). Although a magnetic mechanism is widely considered to be the most likely cause of these large fractionations, there is not yet a tractable quantitative theory to predict or explain the size of the effects observed, or why mercury compounds—particularly methylmercury(II) species—seem to be especially susceptible to magnetic isotope fractionation in natural environments.

#### 4.2. Nuclear Field Shift Effects

This section introduces basic principles governing nuclear field shift effects, and their potential role in causing isotopic signatures in planetary materials. The concepts and terminology of the nuclear field shift effect have been adopted from atomic physics, where it is manifested as shifts in the emission and absorption frequencies of isotopic atoms that cannot be explained by mass differences and hyperfine splitting (King 1984). Bigeleisen (1996a) and Nomura et al. (1996) adapted this concept to explain strange features observed in experiments on  $^{235}\text{U}$  enrichment using ion exchange columns. The experiments contained mixtures of oxidized and reduced uranium

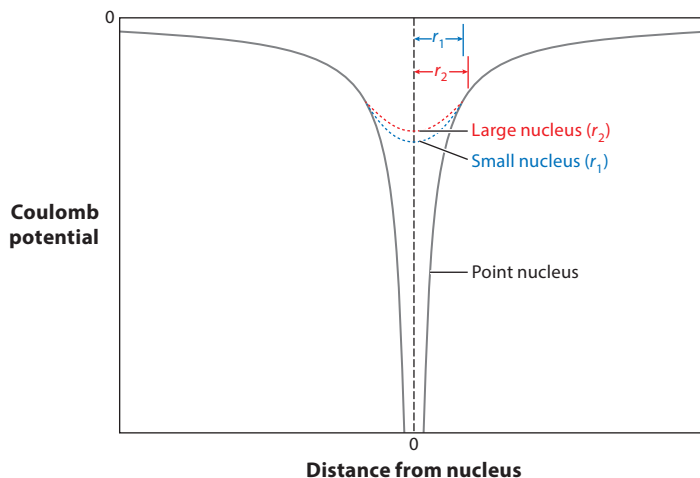


**Figure 5**

The electrostatic potential binding an electron to a nucleus is higher (weaker) for a larger nucleus than for a smaller nucleus. Here the radius difference is assumed to be 10%, much larger than typical differences between isotopes. Adapted with permission from Schauble (2007).

compounds [U(VI) versus U(IV)] (e.g., Fujii et al. 1989) and were designed to achieve isotopic equilibrium. The  $^{238}\text{U}$  isotope was found to be more concentrated in U(IV) species, even though U(VI) compounds are expected to form stronger, stiffer bonds and thus preferentially incorporate the most massive isotopes in mass-dependent equilibrium fractionation. Fujii et al. (1989) and Nomura et al. (1996) also observed that  $^{234}\text{U}/^{235}\text{U}$  ratios ( $|\Delta m| = 1.0030$  amu) fractionated much less than  $^{236}\text{U}/^{235}\text{U}$  ( $|\Delta m| = 1.0016$  amu) in the experiments, despite nearly identical mass differences, and much less than one-third as much as  $^{238}\text{U}/^{235}\text{U}$  ( $|\Delta m| = 3.0069$  amu). Bigeleisen (1996a) noted a resemblance between the relative  $^{233}\text{U}/^{238}\text{U}$ ,  $^{234}\text{U}/^{238}\text{U}$ ,  $^{235}\text{U}/^{238}\text{U}$ , and  $^{236}\text{U}/^{238}\text{U}$  fractionations and spectroscopically observed field shifts in atomic uranium vapor, and proposed that the nuclear field shift effect was the dominant control on the observed isotopic fractionation. He pointed out that measured field shifts had roughly the correct magnitude ( $\sim 1 \text{ cm}^{-1}$ , corresponding to  $\sim 10 \text{ J mol}^{-1}$ , which could drive isotopic fractionation of several per mil at the  $\sim 160^\circ\text{C}$  temperatures of the ion exchange studies). He also showed that the aspherical shape of the  $^{235}\text{U}$  nucleus is expected to have a much smaller effect on isotope fractionation than its size difference relative to  $^{234}\text{U}$  and  $^{238}\text{U}$ ; for this reason, most subsequent research has focused on the nuclear size (or volume) component of the field shift effect.

**4.2.1. Principles of field shift isotope fractionation.** The nuclear field shift effect (schematically illustrated in **Figure 5**) occurs because the positive charge in an atomic nucleus is spread over a finite volume of space with a radius typically  $\sim 1 \times 10^{-15}$  to  $6 \times 10^{-15}$  m (e.g., Fricke & Heilig 2004) rather than being concentrated at an infinitesimal point. The electrons of the atom interact with this volume: When an electron is inside the cloud of positive nuclear charge, the electrostatic attraction of the electron to the outermost shell of positive charge tends to pull in all directions, and thus largely cancels out. Because the net electrostatic attraction is diminished, the electron will not be bound as strongly to a finite-volume nucleus as it would be to a point-charge nucleus. Nuclei that take up more volume will overlap with more electron density, and the electrons will be even more weakly bound. Smaller nuclei hold onto electrons more tightly. An approximate quantitative expression is

$$\delta E_{A-B}^{\text{FS}} \approx \frac{2\pi Z e^2}{3} (|\Psi(0)_A|^2 - |\Psi(0)_B|^2) \Delta \langle r^2 \rangle, \quad (36)$$

$$\ln(\beta_{A-B}^{\text{FS}}) \approx \frac{\delta E_{A-B}^{\text{FS}}}{k_B T},$$

where  $\delta E_{A-B}^{\text{FS}}$  is the field shift energy driving fractionation of two isotopes between substance  $A$  and substance  $B$ ,  $Z$  is the atomic number,  $e$  is the electron charge,  $\Delta \langle r^2 \rangle$  is the difference in the mean square radius of the nuclear charge between two isotopes,  $|\Psi(0)_A|^2$  and  $|\Psi(0)_B|^2$  are the electron densities at the centers of the nuclei in substances  $A$  and  $B$ ,  $E_{A-B}^{\text{FS}}$  is the field shift contribution to isotope fractionation at equilibrium,  $k_B$  is the Boltzmann constant, and  $T$  is the absolute temperature. The equation is approximate because of variation in the nuclear charge density and electron density across the nucleus, and because the electronic structure will adjust when one isotope is substituted for another. However, the equation still serves to illustrate the chemical systematics that control field shift effects [as noted by Mioduski (1999) and others]:

1. Field shift fractionations will scale in proportion to the difference in mean square nuclear charge radius between isotopes, rather than in proportion to mass differences.
2. The field shift is directly sensitive only to electrons in orbitals that have significant density at the nucleus; these are mainly electrons in  $s$  orbitals. Electrons in  $p_{1/2}$  orbitals also have a small electron density at the nucleus (the  $1/2$  subscript indicates the total angular momentum,  $j$ ; two of the six electrons in each  $p$  orbital shell can have  $j = 1/2$ ).
3. Small (usually neutron-poor) isotopes will tend to partition into  $s$  electron-rich species, whereas larger isotopes will prefer to partition into species with fewer  $s$  electrons. Electrons in  $p$ ,  $d$ , and  $f$  orbitals screen  $s$  electrons, reducing their electron density inside nuclei, so they tend to have the opposite effect on isotope partitioning, meaning that large (usually neutron-rich) isotopes tend to partition into species with more  $p$ ,  $d$ , and  $f$  orbital electrons. Whether direct  $s$  electron effects or screening electrons predominate in a particular chemical or geochemical system will depend strongly on which chemical group an element belongs to. This dependence is described in more detail in rules 3a–c, below. Note that these rules are based on an atomic-ionic model of electronic structure; covalent and metallic bonding, including orbital (or band) hybridization, are not accounted for. Such bonding effects may well reverse these rules of thumb in particular cases, particularly for  $p$  block and transition elements.
  - a. For  $s$  block elements (group 1, 2, and 12 elements including the alkaline and alkaline earth elements, Zn, Cd, and Hg) the field shift effect will tend to concentrate large-nucleus (heavy) isotopes in oxidized species, which have fewer valence  $s$  electrons.
  - b. Transition elements, including lanthanides and actinides, tend to lose valence  $s$  electrons first when ionized to a positive charge. In this case, field shift fractionation might be expected to change direction through a range of oxidation states, favoring large-nucleus (heavy) isotopes in moderately positive oxidation states (I, II) lacking one or both valence  $s$  electrons, and favoring lighter isotopes in negative- and zero-oxidation-state species with greater  $s$  orbital occupation. In highly oxidized species, however, a reversal may occur after the valence  $s$  orbital is emptied and screening  $d$  and/or  $f$  electrons start to be removed, favoring lighter isotopes in the most oxidized species.
  - c.  $P$  block elements (groups 13–17, plus the noble gases Ne–Rn) lose screening  $p$  electrons first when ionized to a positive charge and lose  $s$  electrons only after all  $p$  electrons have already been removed. In this case, field shift fractionation is expected to slightly favor compact (light) isotopes in moderately oxidized species and to switch direction to favor voluminous (heavy) isotopes at the highest oxidation states. However, the propensities

for s-p hybridization and covalent bonding at high oxidation states are complicating factors.

4. Atomic spectroscopy shows that nuclear field shifts increase rapidly toward the bottom of the periodic table, suggesting that this mechanism could dominate isotope effects in the heaviest elements in environments where isotope exchange occurs (Bigeleisen 1996a; Knyazev & Myasoedov 2001; Schauble 2007; Abe et al. 2008a,b), but that field shift effects will be modest or undetectable for lighter elements. This occurs because the electron density at the nucleus of valence and near-valence s orbitals increases rapidly with increasing nuclear charge. The relativistic contraction of s orbitals at high atomic number plays an important role in this increase. Mass-dependent fractionations, in contrast, are expected to become less pronounced as atomic or molecular mass increases (Bigeleisen & Mayer 1947), scaling roughly as  $\delta m/m^2$  (at equilibrium) or  $\delta m/m$  (for some kinetic effects such as diffusion), where  $\delta m$  is the difference in mass between two isotopes and  $m$  is the average atomic mass.
5. Nuclear field shift fractionations are expected to show Van 't Hoff-type temperature sensitivity, scaling as  $T^{-1}$ , because most species remain in their ground electronic states even at elevated temperatures (Bigeleisen 1996b), whereas mass-dependent fractionation at equilibrium scales roughly with  $T^{-2}$  (Bigeleisen & Mayer 1947). Therefore, the relative importance of nuclear field shift effects should increase in high-T environments, including possibly in conditions relevant to metamorphic/igneous geochemistry or cosmochemistry.

**4.2.2. Detecting field shift patterns of fractionation in multiple-isotope elements.** In elements with more than two stable or long-lived isotopes, natural nuclear field shift isotope effects may be distinguished by detecting fractionations that track variations in nuclear volume rather than mass. Nuclei with odd numbers of neutrons, in particular, tend to have similar nuclear charge radii to their neighboring isotopes with one fewer neutron (**Figure 6**), with a larger radius step to the even-numbered isotope with one additional neutron. Nuclei with so-called magic numbers of neutrons may be more compact than expected from the radius trends seen in neighboring isotopes (e.g.,  $^4\text{He}$ ,  $^{40}\text{Ca}$ ,  $^{48}\text{Ca}$ ,  $^{50}\text{Ti}$ ,  $^{52}\text{Cr}$ ,  $^{86}\text{Kr}$ ,  $^{87}\text{Rb}$ ,  $^{88}\text{Sr}$ ,  $^{90}\text{Zr}$ ,  $^{92}\text{Mo}$ ,  $^{138}\text{Ba}$ ,  $^{140}\text{Ce}$ ,  $^{142}\text{Nd}$ ,  $^{144}\text{Sm}$ ,

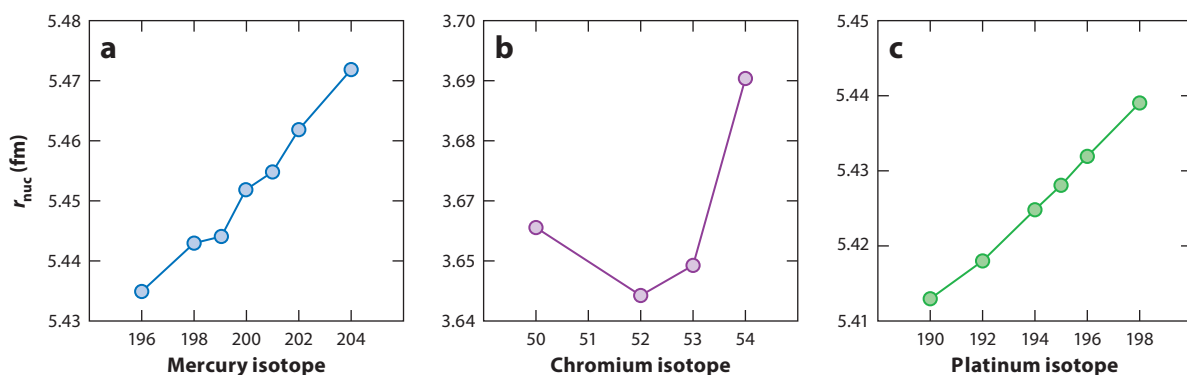


**Figure 6**

Characteristic patterns in root-mean-square nuclear charge radii ( $r_{\text{nuc}}$ ) for mercury, chromium, and platinum isotopes [from the tabulations of Fricke & Heilig (2004) for Hg and Pt and Angeli & Marinova (2013) for Cr]. (a) Mercury, showing the typical odd-even stair-step pattern of increasing radius in neutron-rich isotopes. (b) Chromium, with an anomalously small radius for  $^{52}\text{Cr}$ , a magic (28-neutron) isotope. (c) Platinum, showing nearly linear variation in radius with increasing neutron number across both even and odd isotopes.

$^{208}\text{Pb}$ ) (Fricke & Heilig 2004). Many elements are thus expected to show a characteristic stair-step odd-even pattern of fractionation, and some will show anomalies at particular even-numbered nuclei as well. Many examples of the interpretation of multiple-isotope fractionation patterns as suggestive of field shift effects in laboratory experiments have appeared [well summarized by Fujii et al. (2009) and Moynier et al. (2013)]. This approach has been applied to CAIs of the fractionated and unknown nuclear effects (FUN) type (Fujii et al. 2006b,c; Moynier et al. 2009), but the array of exotic nucleosynthetic anomalies in these samples makes such interpretations particularly tenuous. Comparison of nuclear radii of  $^{199}\text{Hg}$  and  $^{201}\text{Hg}$  with observed isotope fractionations also helped rule out nuclear field shift effects as the dominant cause of observed isotopic variations in mercury from some terrestrial environments (e.g., Blum et al. 2014).

Using the pattern of relative magnitudes of fractionation of different isotope pairs to detect field shift effects has the virtue of simplicity—one need only compare measured fractionations to tabulated nuclear charge radii (e.g., Fujii et al. 2006b) or directly to measured spectroscopic field shifts (Bigeleisen 1996a, Nomura et al. 1996). However, there are also important limitations to this technique. The most obvious is that it only works on elements with more than two long-lived isotopes, where the nuclear size and shape parameters depart from a linear relationship to the number of neutrons. This rules out almost all odd-numbered elements and many even-numbered ones. For instance, the six stable and long-lived platinum isotopes ( $^{190}\text{Pt}$ ,  $^{192}\text{Pt}$ ,  $^{194}\text{Pt}$ ,  $^{195}\text{Pt}$ ,  $^{196}\text{Pt}$ , and  $^{198}\text{Pt}$ ) follow a highly linear mass/nuclear volume relationship (Fricke & Heilig 2004) that makes the field shift pattern difficult to distinguish from mass-dependent fractionation, unless the fractionation is very large. High-precision measurements may resolve very small anomalies, but their interpretation as evidence of field shift effects still must contend with significant disagreements between published nuclear charge radii for some isotopes [e.g., see the discussion by Ghosh et al. (2008) on mercury isotope radii in Fricke & Heilig's (2004) versus Angeli's (2004) tabulations]. Another important limitation is that nuclear size variations tend to correlate with other nuclear properties, such as binding energy (Figure 7), which are important in nucleosynthetic processes. Patterns mimicking field shift effects are also found in more realistic nucleosynthetic models (e.g.,

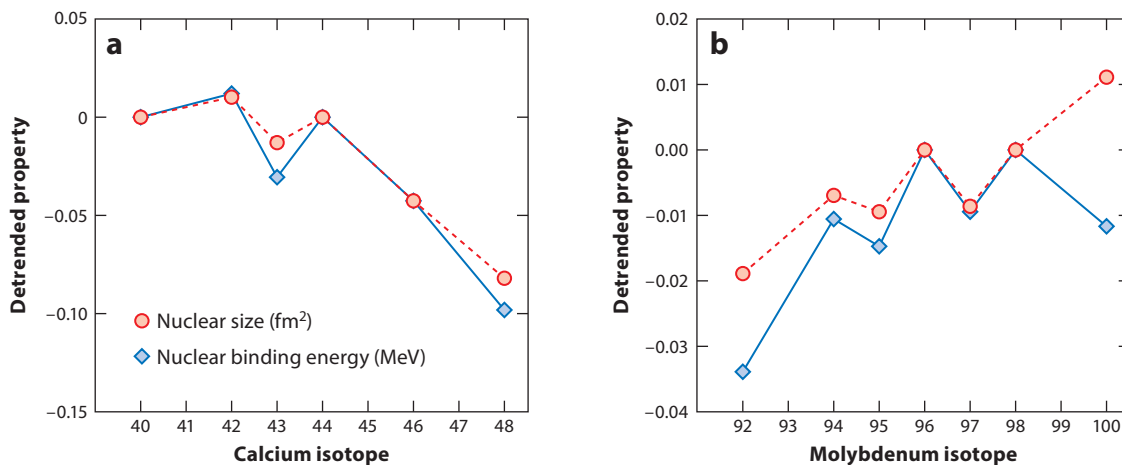


**Figure 7**

Comparison of variations in nuclear size ( $\delta r_{\text{nuc}}^2$ , in units of  $\text{fm}^2$ ; from Fricke & Heilig 2004) (red circles) and binding energy per nucleon (in units of MeV; isotope masses from Audi et al. 2003) (blue diamonds) for stable (a) calcium and (b) molybdenum isotopes. All properties are normalized to  $^{40}\text{Ca}$ ,  $^{44}\text{Ca}$ ,  $^{96}\text{Mo}$ , and  $^{98}\text{Mo}$  following Fujii et al. (2006b,c) and are scaled by differences in isotope number.



Rauscher et al. 2002). This means that, in theory, some types of nucleosynthesis signatures may mimic field shift effects (or vice versa), a particular concern in meteoritic samples (Moynier et al. 2009). In practice, the anomalies in meteorites are often large enough and carried by materials documented to host nucleosynthetic anomalies for other elements, so that there is no ambiguity on the nucleosynthetic nature of these anomalies (see Section 5.6). Because the field shift effect fractionates all isotopes, telltale signatures should be departures from mass-dependent fractionation that correlate with the magnitude and direction of fractionation of the normalizing isotope ratio, and a thermodynamically plausible relationship between the magnitude of fractionation and the temperature at which the fractionating process occurred.

**4.2.3. Electronic structure methods for estimating field shift effects.** To overcome these limitations, it is useful to make quantitative estimates of the magnitude of the nuclear field shift effect at equilibrium for relevant species at relevant temperatures. Bigeleisen (1996a) was able to show that field shifts measured in atomic uranium vapor are large enough to provide a thermodynamic driving energy for per mil-level fractionations at hydrothermal temperatures; the basic electronic structures of U(IV) ( $[\text{Rn}]5f^2$ ) and U(VI) ( $[\text{Rn}]$ ) are also consistent with the observed  $^{238}\text{U}/^{235}\text{U}$  enrichment in the reduced species. However, this argument depends on an assumption that field shift energies in atomic vapors correspond (at least roughly) to ground state isotopic energy shifts between more complex uranium compounds in solution. Over the past decade it has become possible to test this assumption through electronic structure models, which have now been applied to a handful of elements.

Ab initio electronic structure theory has been applied to understanding spectroscopic field shifts for decades (e.g., Wilson 1968). These models have been important for determining nuclear size and shape parameters from the spectral lines in atomic and ionic vapors. Atomic models incorporating relativistic effects were adapted to make the first survey of likely field shift effects in the chemical fractionation of isotopes (Knyazev & Myasoedov 2001) and an early study of  $^{238}\text{U}/^{235}\text{U}$  fractionation between U(IV) and U(III) species (Abe et al. 2008a). Though often thought of as somewhat exotic for ab initio chemical modeling for geochemical and geophysical studies, relativity is an important consideration for accurately simulating the near-nucleus electronic structure of high-atomic number elements (i.e., one must attempt to solve the Dirac equation, rather than the Schrödinger equation). The first relativistic, molecular models of field shift isotope fractionation were reported by Schauble (2007), for mercury and thallium, and by Abe et al. (2008b, 2010), for uranium. These authors noted that field shift effects in molecules share many qualitative characteristics with analogous atoms and atomic ions but are modified and often muted by covalent bonding and coordination. The combined theoretical and experimental study of Wiederhold et al. (2010) took these observations a step further, quantitatively correlating modeled field shifts in Hg(II) species with the ionicity of the bonds as determined by the atomic polar tensor model (Cioslowski 1989), and with measured fractionations on thiol ( $-\text{SH}$ )-containing chelating resins. Relativistic molecular models have now been constructed for select nickel-, zinc-, and lead-bearing species (Fujii et al. 2010, 2011a,b; Yang & Liu 2015), and simple models of this type have also been used to rule out significant field shift isotope fractionation effects in magnesium, sulfur, and strontium (Schauble 2007, 2011; Widanagamage et al. 2014).

Relativistic electronic structure theory is computationally difficult because of the four-component electron/positron wave functions described by the Dirac equations. In practical terms this limits model calculations to small molecules and molecular ions containing up to  $\sim 12$  nonhydrogen atoms, depending on molecular symmetries. Ghosh et al. (2013), Schauble (2013b), and Nemoto et al. (2015) sought to overcome this limit by comparing fully relativistic models against models generated using more simplified methods. Ghosh et al. (2013) adopted a similar approach

to that of Wiederhold et al. (2010), creating a linear regression of nuclear field shift energies versus the orbital population of the valence 6s orbitals in simple mercury-bearing molecules. Using the regression line and previous model results, they were able to estimate the field shift effect in liquid mercury, a metallic material that would be very difficult to model as a small molecule. Their estimate matches well with experiments in which mercury vapor is equilibrated with liquid mercury (Estrade et al. 2009, Ghosh et al. 2013). This regression technique is most likely to be useful for elements where s orbitals are the main participants in chemical bonds (i.e., alkaline elements and alkaline earth elements as well as Zn, Cd, Hg, and, possibly, oxidized species of Ga, In, and Tl). Schauble (2013b) made a regression comparing two types of electronic structure models: relativistic field shift models and density functional theory calculations using the projector augmented wave (PAW) method (Blöchl 1994). The PAW technique is well suited to periodic boundary condition calculations, and so can be applied to solids and liquids as well as to small vapor-phase molecules. Because it describes all valence orbitals, the PAW method is not limited to elements with a particular type of bonding orbital. The technique was applied to reexamine field shift effects in liquid mercury, as well as to predict fractionations in a variety of mercury-, tin-, and cadmium-bearing compounds. Nemoto et al. (2015) adapted the simplified Douglas-Kroll-Hess treatment of relativistic electronic structure (Douglas & Kroll 1974, Hess 1986) to greatly speed up predictions of uranium isotope fractionations in molecular ions. Douglas-Kroll-Hess calculations also have the advantage of being implemented in many widely used molecular electronic structure modeling software codes. Schauble (2013b) also showed that isomer shifts determined by Mössbauer spectroscopy could inform estimates of field shift effects in elements with one or more Mössbauer-suitable isotopes (e.g., iron, zinc, and tin).

### 4.3. Natural Occurrences

**4.3.1. Mercury.** The most convincing examples of magnetic isotope fractionation in natural samples are found in the mercury isotope system (Blum et al. 2014). Briefly, high-precision analytical and experimental studies (e.g., Bergquist & Blum 2007) strongly suggest that magnetic isotope effects in photochemical reduction are the most likely candidate for generating large ( $\geq 1\%$ ) apparent mass-independent fractionations of the odd isotopes  $^{199}\text{Hg}$  and  $^{201}\text{Hg}$  in biological materials, and in inorganic samples that derive their mercury from organic sources. Notably, the pattern of mass-independent fractionation of these two isotopes is quite variable, and does not correlate well with their nuclear charge radii, as would be expected for a field shift effect; the magnitude of the apparent mass-independent fractionation is also much larger than the  $\sim 0.1\%$  to  $0.6\%$  effects predicted by electronic structure models of nuclear field shifts (Schauble 2007, Wiederhold et al. 2010). Samples from mercury ores, minerals, and hydrothermal deposits show much more subtle apparent mass-independent fractionation, however, that is consistent with the field shift effect in magnitude ( $\Delta^{199}\text{Hg} \leq 0.5\%$ ), but they show relatively poorly resolved  $\Delta^{199}\text{Hg}/\Delta^{201}\text{Hg}$  ratios that may not be consistent with the 1.6 ratio expected from the nuclear volume effect (Fricke & Heilig 2004, Blum et al. 2014). A polluted site at the former ore-processing facility of the New Idria mine in California, however, appears to show the expected  $\Delta^{199}\text{Hg}/\Delta^{201}\text{Hg}$ , and other contaminated sites may show similar signatures (Wiederhold et al. 2013, 2015).

**4.3.2. Thallium.** Thallium is likely the first element in which field shift isotope fractionations were measured in terrestrial samples, though it took several years to recognize its importance. In an early reconnaissance study, Rehkämper & Halliday (1999) observed variability in  $^{205}\text{Tl}/^{203}\text{Tl}$  ratios; the largest fractionations were found in samples of Fe-Mn crusts from the seafloor. Subsequent work showed an  $\sim 2\%$  characteristic offset between high  $^{205}\text{Tl}/^{203}\text{Tl}$  Fe-Mn crusts and

low  $^{205}\text{Tl}/^{203}\text{Tl}$  seawater (Rehkämper et al. 2002), and demonstrated that altered oceanic crust was likely to be a complementary reservoir, with lower  $^{205}\text{Tl}/^{203}\text{Tl}$  ratio than seawater (Nielsen et al. 2006b). This systematic offset between the two major sinks of oceanic thallium enabled a proxy study of hydrothermal fluxes through oceanic crust (Nielsen et al. 2006b), among other applications (e.g., Nielsen et al. 2006a). Thallium has only two stable isotopes ( $^{203}\text{Tl}$  and  $^{205}\text{Tl}$ ), and distinguishing the field shift effect from mass-dependent fractionation in the thallium isotope system is difficult from observations alone but can be inferred based on relativistic electronic structure modeling (Schauble 2007). The model results indicated that  $^{205}\text{Tl}/^{203}\text{Tl}$  in highly oxidized Tl(III) species would be offset by  $\sim 3\%$  from coexisting Tl(I) species at equilibrium at ambient temperatures, in reasonable agreement with the observed offset between Fe-Mn crusts and altered basalt. Mass-dependent fractionation is unlikely to generate such large isotope abundance variations but does somewhat enhance field shift fractionation by favoring high  $^{205}\text{Tl}/^{203}\text{Tl}$  in Tl(III) species, accounting for roughly one-fourth of the total redox fractionation at ambient temperatures (Schauble 2007). Experiments on the hexagonal form of the manganese oxide mineral birnessite confirm a predominantly oxidized, Tl(III) speciation in equilibrium with Tl(I)-dominated aqueous solutions (Peacock & Moon 2012), with high  $^{205}\text{Tl}/^{203}\text{Tl}$  in the birnessite-adsorbed thallium reservoir (Nielsen et al. 2013). Recent work has suggested that sulfide minerals may host Tl(I) species in altered oceanic crust (Coggon et al. 2014).

**4.3.3. Uranium.** Although the field shift effect was first proposed for isotope fractionation of uranium in the laboratory (Bigeleisen 1996a), it took another decade before the first high-precision analyses of natural materials appeared (Stirling et al. 2007, Weyer et al. 2008). These reconnaissance studies showed that  $^{238}\text{U}/^{235}\text{U}$  ratios are variable in terrestrial samples, particularly those influenced by low-T water-rock interactions. Weyer et al. (2008) found a characteristic enrichment of  $^{238}\text{U}/^{235}\text{U}$  by up to  $1\%$  in sediments deposited in anoxic environments, relative to seawater and typical igneous samples. This systematic oxidation/reduction pattern is consistent with the experiments discussed above in which U(IV) species show high  $^{238}\text{U}/^{235}\text{U}$  relative to U(VI) species (Fujii et al. 1989, Nomura et al. 1996). A series of theoretical studies (Schauble 2006; Abe et al. 2008a,b, 2010; Nemoto et al. 2015) investigated likely field shift effects (and corresponding mass-dependent fractionations) associated with U(IV)  $\leftrightarrow$  U(VI) equilibrium. These predict  $\sim 1\text{--}2\%$  higher  $^{238}\text{U}/^{235}\text{U}$  in U(IV) in equilibrium with a variety of  $\text{UO}_2^{2+}$ -bearing aqueous species, in rough agreement with the largest natural fractionations measured (see Tissot & Dauphas 2015 for a recent compilation). As predicted by Bigeleisen (1996a) and Mioduski (1999), the models show that large nuclear field shift effects overwhelm smaller mass-dependent fractionation in the opposite direction (**Figure 8**). Recent laboratory experiments indicate an equilibrium U(IV) versus U(VI) fractionation of approximately  $1.6\%$  in aqueous solution at low pH (Wang et al. 2015b), and a somewhat smaller fractionation of  $1.1\%$  during aqueous oxidation of U(IV) $\text{O}_2$  (Wang et al. 2015a). In contrast, uranium from oxidizing sediments, including Fe-Mn crusts, typically shows somewhat lower  $^{238}\text{U}/^{235}\text{U}$  ratio than seawater. Birnessite adsorption studies reproduce this  $^{238}\text{U}/^{235}\text{U}$  depletion, and extended X-ray absorption fine structure spectra suggest that the formation of a strained surface complex is responsible (Brennecke et al. 2011).

Terrestrial  $^{238}\text{U}/^{235}\text{U}$  signatures, most likely reflecting various processes of exchange or partial reaction between U(VI) and U(IV) near Earth's surface, have also been reported in low-T hydrothermal uranium ores and refined ore products (e.g., Bopp et al. 2009, Brennecke et al. 2010a), in groundwater systems (Bopp et al. 2010, Murphy et al. 2014), and in the mantle sources of oceanic basalts (Andersen et al. 2015). Large variations in  $^{238}\text{U}/^{235}\text{U}$  (of uncertain origin) have also been reported in igneous mineral separates (Hiess et al. 2012). In contrast, many meteorite

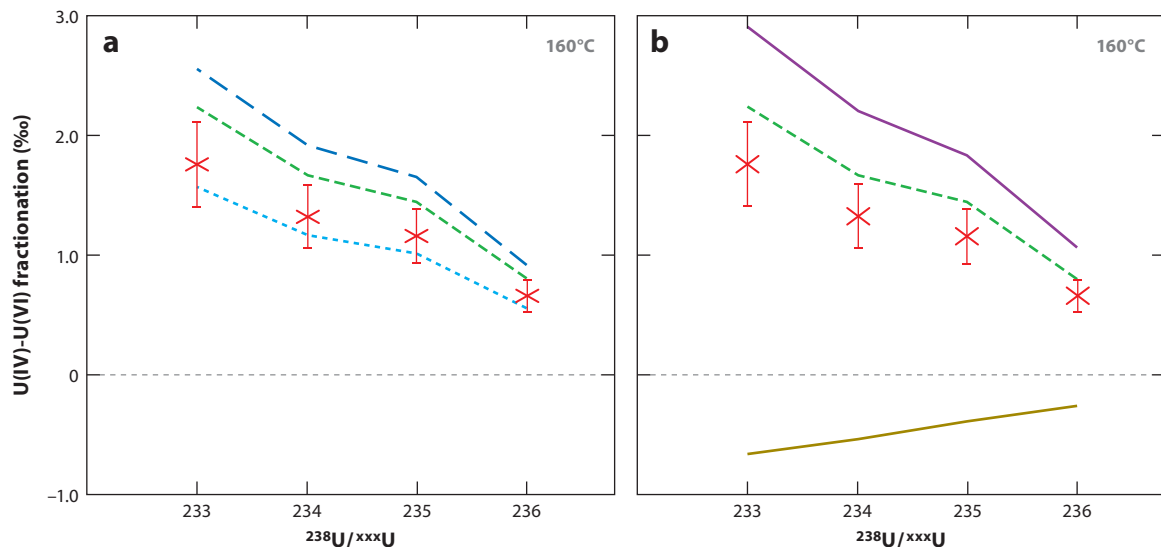


**Figure 8**

Uranium isotope fractionation between U(IV) and U(VI) species during hydrothermal ion exchange separation at 160°C, studied by Fujii et al. (1989, 2006a) and Nomura et al. (1996), compared to theoretical models. Experimental fractionations (*diagonal crosses*) are determined by scaling the equilibrium  $^{238}\text{U}/^{235}\text{U}$  fractionation factor reported by Fujii et al. (2006a) for other isotope pairs using Nomura et al.'s (1996) tabulation. (a) The dashed light blue line represents theoretical fractionation combining the estimated  $\text{UCl}_4\text{-UO}_2\text{Cl}_4^{2-}$  nuclear volume effect from Abe et al. (2010) and mass-dependent effects from Bigeleisen (1996a). The dashed green line represents total  $\text{U}(\text{H}_2\text{O})_{8-9}^{4+}$  versus  $\text{UO}_2\text{Cl}_3(\text{H}_2\text{O})_2^-$  fractionation from Schauble (2006) using nuclear charge radii tabulated by Angeli & Marinova (2013). The dashed dark blue line represents total  $\text{U}(\text{H}_2\text{O})_{8-9}^{4+}$  versus  $\text{UO}_2\text{Cl}_3(\text{H}_2\text{O})_2^-$  fractionation from Schauble (2006) using nuclear radii tabulated by Fricke & Heilig (2004). (b) Total  $\text{U}(\text{H}_2\text{O})_{8-9}^{4+}$  versus  $\text{UO}_2\text{Cl}_3(\text{H}_2\text{O})_2^-$  fractionation from Schauble (2006) (*dashed green line*) using nuclear radii tabulated by Angeli & Marinova (2013), showing mass-dependent (*solid dark yellow line*) and nuclear volume (*solid purple line*) components.

classes and materials appear to be quite uniform in composition (e.g., Goldmann et al. 2015), except for refractory inclusions that display isotopic variations associated with  $^{247}\text{Cm}$  decay and U condensation/evaporation (Brennecka et al. 2010b, Tissot et al. 2016).

**4.3.4. Lighter elements.** There have not yet been unambiguous detections of nuclear field shift effects in any elements with  $Z < 80$  in natural samples. Theoretical studies suggest that field shift effects should become increasingly subtle at lower atomic numbers (Knyazev & Myasoedov 2001, Schauble 2007) but still may yield detectable signatures in elements such as europium (Abe et al. 2008a); ruthenium (Schauble 2007); tin (Schauble 2013b); molybdenum, platinum, and rhenium (Schauble 2008, 2013b; Miller et al. 2015); and tungsten (Schauble 2013a; also see below).

## 5. CARRIERS OF NUCLEOSYNTHETIC ANOMALIES AND THEIR MANIFESTATIONS

It was found early on that meteorites had noble gas isotopic compositions that could not be related to the solar composition by mass-dependent fractionation. Some of these variations were rightfully ascribed to decay of short-lived radionuclides such as  $^{129}\text{I}$  or  $^{244}\text{Pu}$  that produce  $^{129}\text{Xe}$  and heavy fissionogenic xenon ( $^{131}\text{Xe}$ ,  $^{132}\text{Xe}$ ,  $^{134}\text{Xe}$ , and  $^{136}\text{Xe}$ ) (Jeffery & Reynolds 1961, Rowe & Kuroda

1965). Other isotopic variations could not be explained by radioactive decay and must reflect the presence of signatures inherited from stellar nucleosynthesis. Lewis et al. (1987) and Bernatowicz et al. (1987) were first able to isolate the carriers of these isotopic anomalies as presolar grains (e.g., nanodiamonds and silicon carbides) that condensed in the outflows of stars that lived and died before the Solar System was formed (Anders & Zinner 1993, Clayton & Nittler 2004, Lodders & Amari 2005). Other meteoritic materials such as hibonite grains, CAIs, and acid leachates also display isotopic anomalies of nucleosynthetic origin, albeit of much smaller magnitude. Below, we review the nature of the presolar grains that have been identified and discuss their isotopic manifestations at a macroscopic scale.

## 5.1. Presolar Grain Types and Their Signatures

Presolar grains are usually detected in undifferentiated (nonmolten) meteorites by the fact that they have nonsolar/nonterrestrial isotopic compositions (Anders & Zinner 1993, Zinner 2003, Clayton & Nittler 2004, Lodders & Amari 2005), so the sampling is somewhat biased in the sense that grains with near-solar composition would be overlooked. Much of the early work focused on isotopic anomalies for noble gases in grains that were resistant to harsh chemical treatments (Huss & Lewis 1995). Subsequent work by ion probe allowed isotopic mapping of meteorite sections to find anomalous grains, which led to the discovery of presolar grains that were less chemically resistant, such as silicates or nanospinel (Messenger et al. 2003, Nguyen & Zinner 2004, Dauphas et al. 2010, Qin et al. 2011b). Studies of presolar grains, their structures, their major and trace element compositions, and their isotopic compositions have provided considerable information on stellar nucleosynthesis, mixing within stars, and condensation in stellar outflows, which complements remote spectroscopic observations and informs modeling of stellar evolution. In-depth discussions of the zoo of isotopic anomalies can be found in recent reviews (Zinner 2003, Clayton & Nittler 2004, Lodders & Amari 2005, Davis 2011). Below we give a brief overview of the nature of isotopic signatures found in presolar grains.

**5.1.1. Nanodiamonds.** Presolar nanodiamonds were discovered by Lewis et al. (1987). They are isolated by digestion of meteorites in acids, to recover the most chemically resistant grains (Lewis et al. 1987, Amari et al. 1994). They are small grains (2.8 nm median diameter; i.e.,  $\sim 1,800$  atoms of carbon) that contain Xe with a characteristic isotopic pattern that is enriched in the heavy and light Xe isotopes (hence the name Xe-HL). Recent work showed that the nanodiamond separates are actually mixtures of bona fide nanodiamond and glassy carbon (Stroud et al. 2011). As a whole, they have solar-like C and N isotopic composition and the majority ( $\sim 1,400$  ppm in abundance in the Murchison CM chondrite) may have a solar origin (Xe is a poor tracer of provenance because, on average, there is approximately one Xe atom per million diamond grains). Anomalies were found for tellurium (Richter et al. 1998), but the grains were not characterized beyond that due to the analytical challenges of measuring such small grains and contamination of the nanodiamond separates with other presolar phases.

**5.1.2. Silicon carbides.** Presolar SiC ( $\sim 30$  ppm in Murchison) were discovered by Bernatowicz et al. (1987). They are isolated in the residue after digesting away less chemically resistant phases (Amari et al. 1994). These grains range in size from a few nanometers to a few tens of micrometers, are crystalline of cubic (3C) and hexagonal (2H) structures (Daulton et al. 2003), and are among the most studied presolar grains. They are classified into various subgroups on the basis of their  $^{13}\text{C}/^{12}\text{C}$ ,  $^{15}\text{N}/^{14}\text{N}$ , and  $^{30}\text{Si}/^{28}\text{Si}$ - $^{29}\text{Si}/^{28}\text{Si}$  ratios, which show very large variations covering many orders of magnitude (Hynes & Gyngard 2009). In the zoo of presolar grains, two populations have

been the focus of most studies. X grains are thought to come from core-collapse supernovae, which are the endpoints of the evolution of massive stars [ $>8$  solar masses ( $M_{\odot}$ )] when they have finished burning their fuels and collapse onto their inert Fe-Ni cores to bounce back into violent explosions. The most common presolar silicon carbides are mainstream grains. They are thought to come from AGB stars (AGB, for asymptotic giant branch, refers to a region of the color-magnitude diagram used for stellar classification), which are the site of the slow process of neutron capture ( $s$ -process). Stars that are 1 to 8  $M_{\odot}$  enter the AGB phase after they have finished burning He in their core. AGB stars have a shell structure, with a CO core (the product of He burning), He- and H-burning shells, and a convective envelope. At regular intervals, the convective envelope mixes with the region between the He- and H-burning shells. This brings together protons from the envelope and  $^{12}\text{C}$  produced by He burning to make  $^{13}\text{C}$ . The  $^{13}\text{C}$  thus produced can then react with helium ( $\alpha$  particles) to make neutrons ( $n$ ) through the reaction  $^{13}\text{C} + \alpha \rightarrow ^{16}\text{O} + n$ . Another source of neutrons comes from the  $^{22}\text{Ne} + \alpha \rightarrow ^{25}\text{Mg} + n$  reaction, where  $^{22}\text{Ne}$  is made through  $\alpha$  capture on  $^{14}\text{N}$  produced in the CNO cycle. These reactions are neutron sources for the  $s$ -process. Studies of mainstream SiC have provided a wealth of information on the  $s$ -process path and grain condensation in AGB winds. A good example is given by the Ru isotopic analyses performed on mainstream SiC using a resonant ionization mass spectrometer (Savina et al. 2004). These measurements revealed the presence of large Ru nucleosynthetic anomalies characterized by enrichment in  $s$ -process isotopes. The grain data could be reproduced only if one assumed that the short-lived nuclide  $^{99}\text{Tc}$  ( $t_{1/2} = 2.11$  kyr) had condensed in the grains when they formed.  $^{99}\text{Tc}$  is a pure  $s$ -process nuclide whose detection by Merrill (1952) in stellar spectra gave credence to the theory of stellar nucleosynthesis outlined by B<sup>2</sup>FH (Burbidge et al. 1957) and Cameron (1957). Other SiC grain types (AB, Y, Z, nova) are thought to come from more exotic stars such as J stars, born-again AGBs, AGB stars of metallicities lower than solar, and novae.

**5.1.3. Graphite.** Presolar graphite grains (10 ppm in Murchison) were discovered by Amari et al. (1990). They often contain subgrains of refractory carbide and metal (Croat et al. 2014). They have anomalous  $^{13}\text{C}/^{12}\text{C}$  ratios but near-solar  $^{15}\text{N}/^{14}\text{N}$  ratios, presumably reflecting contamination by meteoritic or terrestrial nitrogen during residence in the parent body or during processing with harsh reagents in the laboratory. Approximately two-thirds by mass of presolar graphite comes from core-collapse supernovae, and approximately one-third comes from AGB stars (Amari et al. 2014). Presolar graphite is often separated into low- and high-density fractions. The low-density fractions contain a larger proportion of supernova grains (Amari et al. 2014).

**5.1.4. Silicon nitride.** Mapping of chemically resistant residues from meteorites has revealed the presence of rare presolar silicon nitride grains that are thought to originate from core-collapse supernovae as these grains have an isotopic signature similar to that of type X SiC grains (Nittler et al. 1995).

**5.1.5. Oxides.** Various types of oxides have been identified by mapping acid residues for their oxygen isotopic compositions (Nittler et al. 1997). The presolar mineral phases identified comprise aluminum oxide, hibonite, spinel, chromite, and  $\text{TiO}_2$ . The majority of presolar oxides (90%) come from AGB stars, and 10% come from core-collapse supernovae. Of particular relevance to this article are presolar nanospinel rich in  $^{54}\text{Cr}$  that were discovered in fine-grained size separates from the Murchison meteorite (Dauphas et al. 2010, Qin et al. 2011b). Rotaru et al. (1992) showed that acid leachates of primitive meteorites had variable  $^{54}\text{Cr}$  abundance. The difficulty with identifying the carrier of these anomalies was that the carrier was chemically labile (i.e., digested in hot HCl) and was very fine grained (the largest anomalies were found in a colloidal fraction with a mode

in the grain size distribution of  $\sim 30$  nm). Isotopic imaging of the  $^{54}\text{Cr}$ -rich fraction revealed the presence of Cr-bearing nanospinel that were very enriched in  $^{54}\text{Cr}$  (up to 3.6 times solar, and possibly up to 50 times solar after correction for contamination with solar composition from the surrounding grains due to the finite size of the ion probe primary beam). Such large enrichments can be produced in both type Ia (presumably binary systems whereby a white dwarf accretes matter from a more massive companion star) and type II (core-collapse) supernovae. A difficulty with type Ia is that no grain is expected to survive the explosion and no grains have been observed spectroscopically in type Ia supernova remnants (Nozawa et al. 2011). However, it is conceivable that  $^{54}\text{Cr}$ -rich matter ejected from type Ia supernovae would condense onto preexisting grains in the interstellar medium.

**5.1.6. Silicates.** Grains in the interstellar medium comprise a significant fraction of silicates, which are primarily amorphous (Draine 2009). The original method for separating presolar grains was compared to burning the haystack to find the needle, meaning that most of the meteorite was digested in acids to concentrate chemically resistant phases. It is only through the advent of high-spatial-resolution nanoSIMS that presolar silicates were identified by isotopic mapping of pristine (weakly altered and metamorphosed) meteorites and interplanetary dust particles of presumed cometary origin (Messenger et al. 2003, Nguyen & Zinner 2004). For the most part, presolar silicates have the same signatures as presolar oxides and come from similar stellar environments.

All the presolar grains mentioned above are susceptible to destruction during metamorphism on meteorite parent bodies (Huss & Lewis 1995). As metamorphism increases, the grains disappear and the isotopic compositions become uniform. Nevertheless, the macroscopic isotopic anomalies that the grains may have imparted to the bulk meteorites remain unchanged during metamorphism.

## 5.2. Hibonite Grains and Refractory Inclusions

The isotopic anomalies found in presolar grains are usually very large, in some instances covering several orders of magnitude. More subtle isotopic effects are found in macroscopic objects. In some instances, the presolar carriers of these anomalies have been identified, such as in the case of noble gases (nanodiamonds, graphite, silicon carbide) (Huss & Lewis 1995) or  $^{54}\text{Cr}$  (nanospinel) (Dauphas et al. 2010, Qin et al. 2011b). In most cases, however, the macroscopic anomalies cannot be tied to a special carrier. Several categories of planetary materials display macroscopic anomalies that are presented hereafter.

**5.2.1. Hibonite-rich inclusions.** Hibonite ( $\text{CaAl}_{12-2x}\text{Mg}_x\text{Ti}_x\text{O}_{19}$ ;  $\text{Ti}^{4+}$  and  $\text{Mg}^{2+}$  are mainly incorporated through a coupled substitution with  $2\text{Al}^{3+}$ , but Ti also exists as  $\text{Ti}^{3+}$ ) is a highly refractory mineral that is found in meteorites in refractory inclusions and as isolated grains in the matrix of primitive meteorites. Hibonite grains have typical sizes of 50 to 100  $\mu\text{m}$  and have been most extensively studied in the Murchison CM carbonaceous chondrite, as this meteorite is particularly rich in hibonite inclusions. Ireland (1988) identified three main subtypes of hibonite inclusions. Spinel-hibonite inclusions (SHIBs) range in size from 50 to 300  $\mu\text{m}$  and contain several minerals in addition to hibonite, such as spinel and perovskite. Platy hibonite crystals (PLACs) are  $\sim 70$  to 150  $\mu\text{m}$  in size and are composed of colorless crystal fragments of hibonite. Blue aggregates (BAGs) are small grains ( $< 80$   $\mu\text{m}$ ) composed of blue hibonite. For the most part, the oxygen isotopic compositions of hibonite inclusions plot close to the compositions of larger CAIs (Fahey et al. 1987a, Liu et al. 2009, Kööp et al. 2016), which may correspond to the composition of the Sun (McKeegan et al. 2011). Magnesium isotopes also show limited variations relative to the

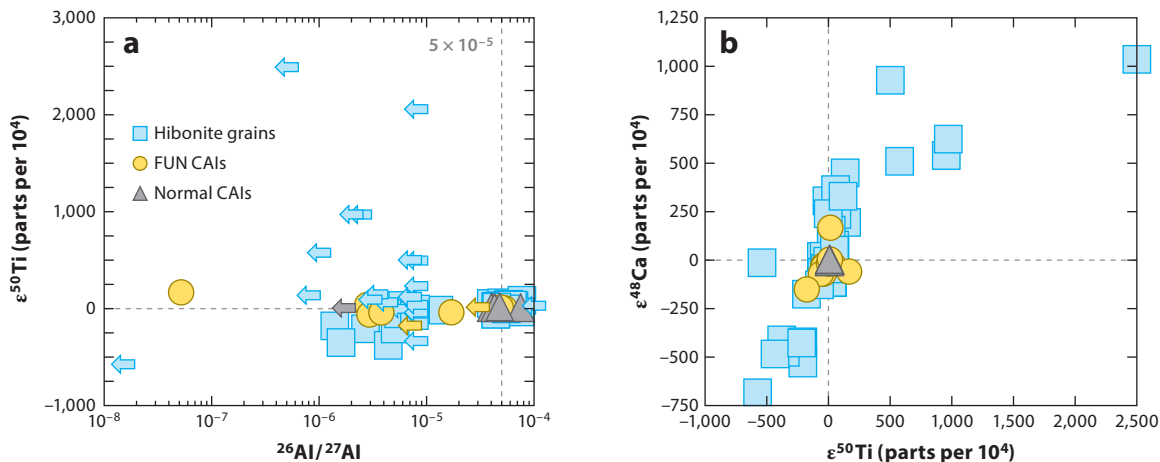


**Figure 9**

Ca and Ti isotopic anomalies in hibonite grains, FUN CAIs, and normal CAIs. The variations found in refractory materials in primitive chondrites affect predominantly the neutron-rich isotopes  $^{48}\text{Ca}$  and  $^{50}\text{Ti}$ . (a) The samples that have a canonical  $^{26}\text{Al}/^{27}\text{Al}$  initial ratio of  $\sim 5 \times 10^{-5}$  display limited variations in  $\epsilon^{50}\text{Ti}$  values, between  $-57$  and  $+86$  parts per  $10^4$ , whereas the samples with lower  $^{26}\text{Al}/^{27}\text{Al}$  initial ratios ( $< 0.7 \times 10^{-5}$ ) show much more variable  $\epsilon^{50}\text{Ti}$  values, between  $-574$  and  $+2,491$  parts per  $10^4$ . (b) The anomalies in  $^{48}\text{Ca}$  and  $^{50}\text{Ti}$  are roughly correlated. The following notations are used:  $\epsilon^{48}\text{Ca} = [({}^{48}\text{Ca}/{}^{44}\text{Ca})_{\text{sample}}^*/({}^{48}\text{Ca}/{}^{44}\text{Ca})_{\text{standard}}^* - 1] \times 10^4$ , and  $\epsilon^{50}\text{Ti} = [({}^{50}\text{Ti}/{}^{47}\text{Ti})_{\text{sample}}^*/({}^{50}\text{Ti}/{}^{47}\text{Ti})_{\text{standard}}^* - 1] \times 10^4$ , where standard refers to the terrestrial compositions and the asterisk denotes the fact that the ratios are internally normalized by fixing the  $^{42}\text{Ca}/{}^{44}\text{Ca}$  and  $^{49}\text{Ti}/{}^{47}\text{Ti}$  ratios to constant values. Data sources: Lee & Papanastassiou (1974), Esat et al. (1979), Lee et al. (1979), Niederer et al. (1981, 1985), Niemeyer & Lugmair (1981, 1984), Armstrong et al. (1984), Jungck et al. (1984), Niederer & Papanastassiou (1984), Zinner et al. (1986), Fahey et al. (1987a,b), Papanastassiou & Brigham (1989), Brigham (1990), Ireland (1990), Ireland et al. (1991), Loss et al. (1994), Sahijpal et al. (2000), Hsu et al. (2006), MacPherson et al. (2007), Liu et al. (2009), H.W. Chen et al. (2010), Holst et al. (2013), Park et al. (2013, 2014), Schiller et al. (2015); G. Huss (personal communication). Abbreviations: CAI, calcium-aluminum-rich inclusion; FUN, fractionated and unknown nuclear effects.

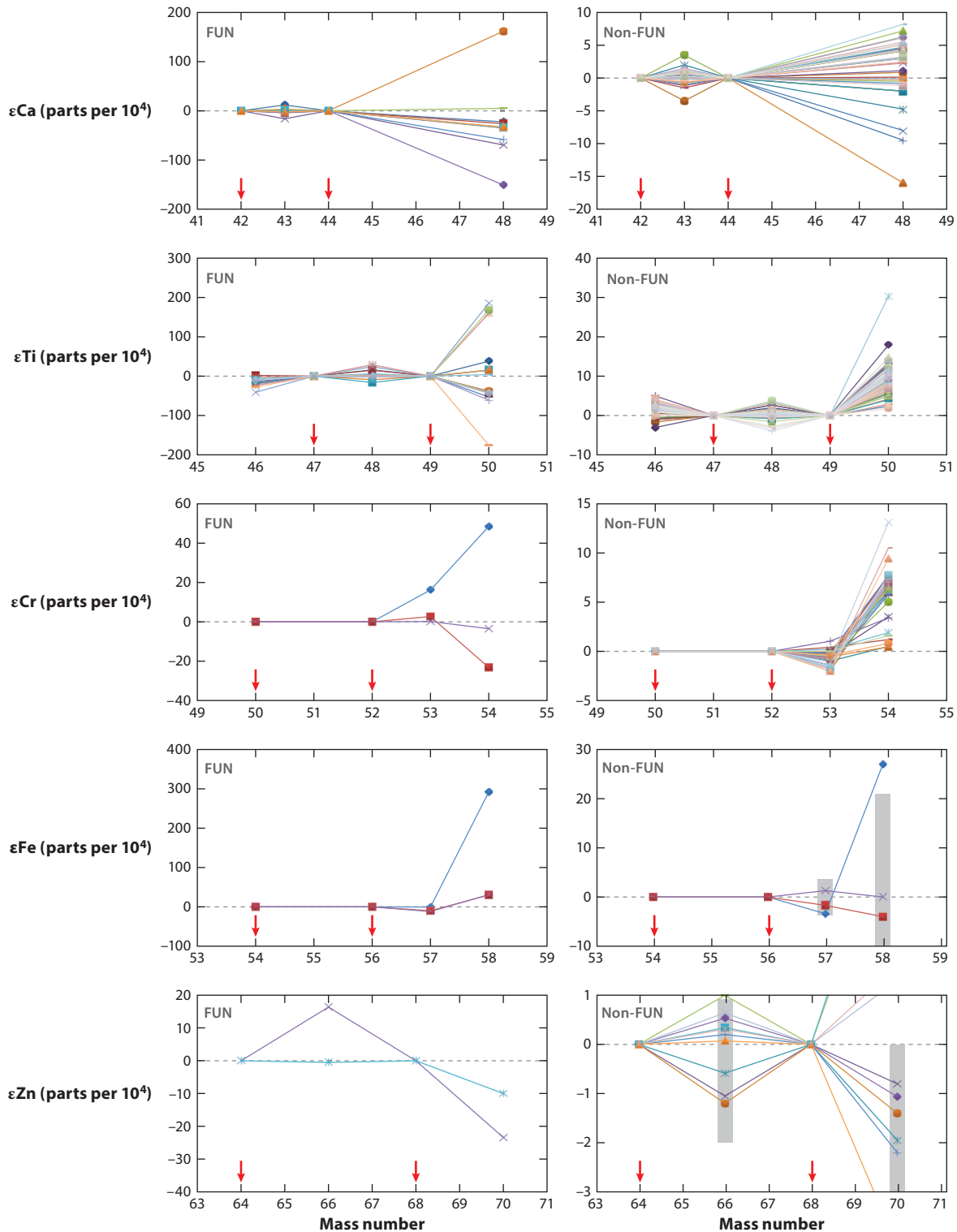
terrestrial (solar) composition, except for those arising from  $^{26}\text{Al}$  decay (Fahey et al. 1987b, Ireland 1990, Sahijpal et al. 2000, Liu et al. 2009, Kööp et al. 2016). The refractory elements Ca and Ti show large isotopic variations in hibonite inclusions that require the presence of multiple (four or more) nucleosynthetic components to explain the data. The most marked anomalies concern the neutron-rich isotopes  $^{48}\text{Ca}$  and  $^{50}\text{Ti}$  (Zinner et al. 1986; Fahey et al. 1987a,b; Ireland 1990; Ireland et al. 1991; Sahijpal et al. 2000; Liu et al. 2009; Kööp et al. 2016). The anomalies in  $\epsilon^{50}\text{Ti}$  (deviation relative to Earth of the  $^{50}\text{Ti}/{}^{47}\text{Ti}$  ratio after correction of mass fractionation by internal normalization to a fixed  $^{49}\text{Ti}/{}^{47}\text{Ti}$  ratio) range from approximately  $-500$  to  $+2,800$  parts per  $10^4$  and correlate grossly with variations in  $\epsilon^{48}\text{Ca}$  (deviation relative to Earth of the  $^{48}\text{Ca}/{}^{44}\text{Ca}$  ratio after internal normalization to a fixed  $^{42}\text{Ca}/{}^{44}\text{Ca}$  ratio) (**Figure 9**).  $^{50}\text{Ti}$  can be produced in both core-collapse and type Ia supernovae (see Section 5.1 for definitions), but  $^{48}\text{Ca}$  is difficult to produce in environments other than type Ia supernovae (Woosley 1997). Hibonite inclusions are small, and the isotopic compositions of trace elements are unknown. A striking feature of hibonite grains that is also relevant to macroscopic CAIs is that the scale of the nucleosynthetic anomalies correlates with the presence or absence of  $^{26}\text{Al}$  at the time of formation ( $^{26}\text{Al}$  is a short-lived radionuclide that decays into  $^{26}\text{Mg}$  with a half-life of 0.7 Myr and was present in the early Solar System when meteorites formed) (**Figure 9a**). The hibonite grains and CAIs that have a  $^{26}\text{Al}/^{27}\text{Al}$  ratio of  $5 \times 10^{-5}$  (the so-called canonical value as it is found in most CAIs) show relatively subdued variations in  $\epsilon^{50}\text{Ti}$  (and  $\epsilon^{48}\text{Ca}$ ), with values that range between  $-60$  and  $+60$  parts per



$10^4$ . In contrast, samples with  $^{26}\text{Al}/^{27}\text{Al}$  that is not detectable or below  $8 \times 10^{-6}$  have much more varied  $\epsilon^{50}\text{Ti}$  (and  $\epsilon^{48}\text{Ca}$ ) isotopic compositions, with values that range between  $-572$  and  $+2,537$  parts per  $10^4$ . The data points show a clear dichotomy in  $^{26}\text{Al}/^{27}\text{Al}$  ratios. There are two possible explanations for these observations (Fahey et al. 1987b, Liu et al. 2009). One is that the hibonite grains and CAIs with low  $^{26}\text{Al}/^{27}\text{Al}$  initial ratios were formed  $\sim 2$  Myr after those with an initial  $^{26}\text{Al}/^{27}\text{Al}$  ratio of  $5 \times 10^{-5}$ . The difficulty with this interpretation is that, whereas one would expect the refractory materials condensed later to have formed from a disk that had homogenized so that they should show more subdued anomalies compared to those formed earlier, in fact the opposite is observed. The preferred interpretation is that  $^{26}\text{Al}$  was heterogeneously distributed in the protosolar disk, and that the samples with a low abundance of  $^{26}\text{Al}$  were formed early, before homogenization of  $^{26}\text{Al}$  in the disk, whereas the samples with the subdued  $^{50}\text{Ti}$  anomalies and high  $^{26}\text{Al}/^{27}\text{Al}$  ratio are more representative of the average composition of the disk. A challenge with this second scenario is that it does not explain readily why early-formed hibonite and CAIs formed early did not sample portions of the disk that had  $^{26}\text{Al}/^{27}\text{Al}$  ratios much higher than the canonical value of  $5 \times 10^{-5}$ .

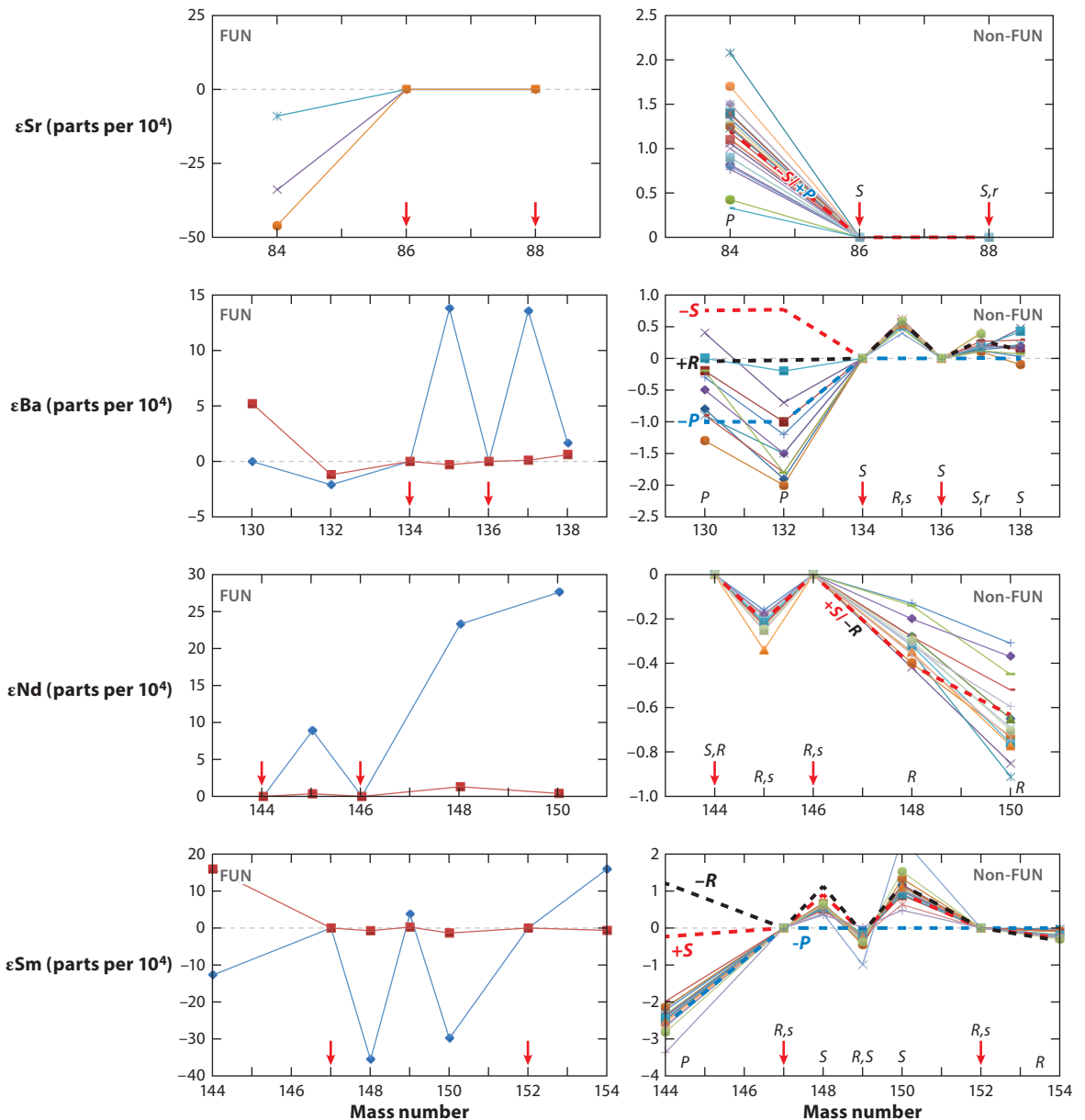
**5.2.2. FUN and regular CAIs.** CAIs are refractory mineral assemblages whose chemistry corresponds to that expected for condensation at high temperature of gas of solar composition (Grossman 1972). Refractory lithophile elements like light rare earth elements have concentrations that are enriched 20-fold relative to CI chondrites (Ivuna-type carbonaceous chondrites, a type of meteorite that matches well the solar composition measured by spectroscopy) because 95% of the condensable elements in CI chondrites were not condensed under the high-temperature conditions relevant to CAI formation. Several lines of evidence support the fact that CAIs condensed from gas of solar composition, notably their  $^{16}\text{O}$ -rich solar-like oxygen isotopic compositions (Clayton et al. 1973, McKeegan et al. 2011); the elevated concentrations of reduced  $\text{Ti}^{3+}$ , consistent with reducing nebular-like conditions (Beckett 1986, Grossman et al. 2008); and the concentrations of refractory lithophile elements that are in solar proportions (Mason & Taylor 1982). However, CAIs also contain nucleosynthetic anomalies relative to Earth's composition (**Figure 10**). From the point of view of isotopic compositions, two main types of CAIs are recognized. FUN inclusions are rare CAIs that often display large nucleosynthetic anomalies as well as large mass-dependent fractionation (consistent with evaporation/condensation processes). Normal CAIs also often display nucleosynthetic anomalies, but the effects are more subdued and the extent of mass-dependent isotopic fractionation is also smaller. As in hibonite grains, there is a relationship between the presence or absence of  $^{26}\text{Al}$  (Lee & Papanastassiou 1974, Esat et al. 1979, Armstrong et al. 1984, Fahey et al. 1987b, Brigham 1990, Hsu et al. 2006, MacPherson et al. 2007, Holst et al. 2013, Park et al. 2013) and the scale of the isotopic anomalies in CAIs (Niederer et al. 1981, 1985; Fahey et al. 1987b; Papanastassiou & Brigham 1989; Park et al. 2014) (**Figure 9a**). FUN CAIs have low  $^{26}\text{Al}$  and display large isotopic anomalies, whereas non-FUN CAIs display smaller anomalies and have a canonical  $^{26}\text{Al}/^{27}\text{Al}$  ratio ( $5 \times 10^{-5}$ ).

For Ca, Ti, Cr, Fe, and Ni, the isotopic anomalies in both FUN and non-FUN CAIs affect preferentially the neutron-rich isotopes  $^{48}\text{Ca}$  (Lee et al. 1979, Jungck et al. 1984, Niederer & Papanastassiou 1984, Papanastassiou & Brigham 1989, Loss et al. 1994, H.W. Chen et al. 2010, Moynier et al. 2010, Huang et al. 2012, Park et al. 2014, Schiller et al. 2015),  $^{50}\text{Ti}$  (Niemeyer & Lugmair 1981, 1984; Niederer et al. 1981, 1985; Fahey et al. 1987b; Papanastassiou & Brigham 1989; Loss & Lugmair 1990; Loss et al. 1994; Leya et al. 2009; Trinquier et al. 2009; Park et al. 2014; Zhang 2012),  $^{54}\text{Cr}$  (Birck & Allègre 1984, 1988; Papanastassiou 1986; Birck & Lugmair 1988; Loss et al. 1994; Bogdanovski et al. 2002),  $^{58}\text{Fe}$  (Völkening & Papanastassiou 1989), and

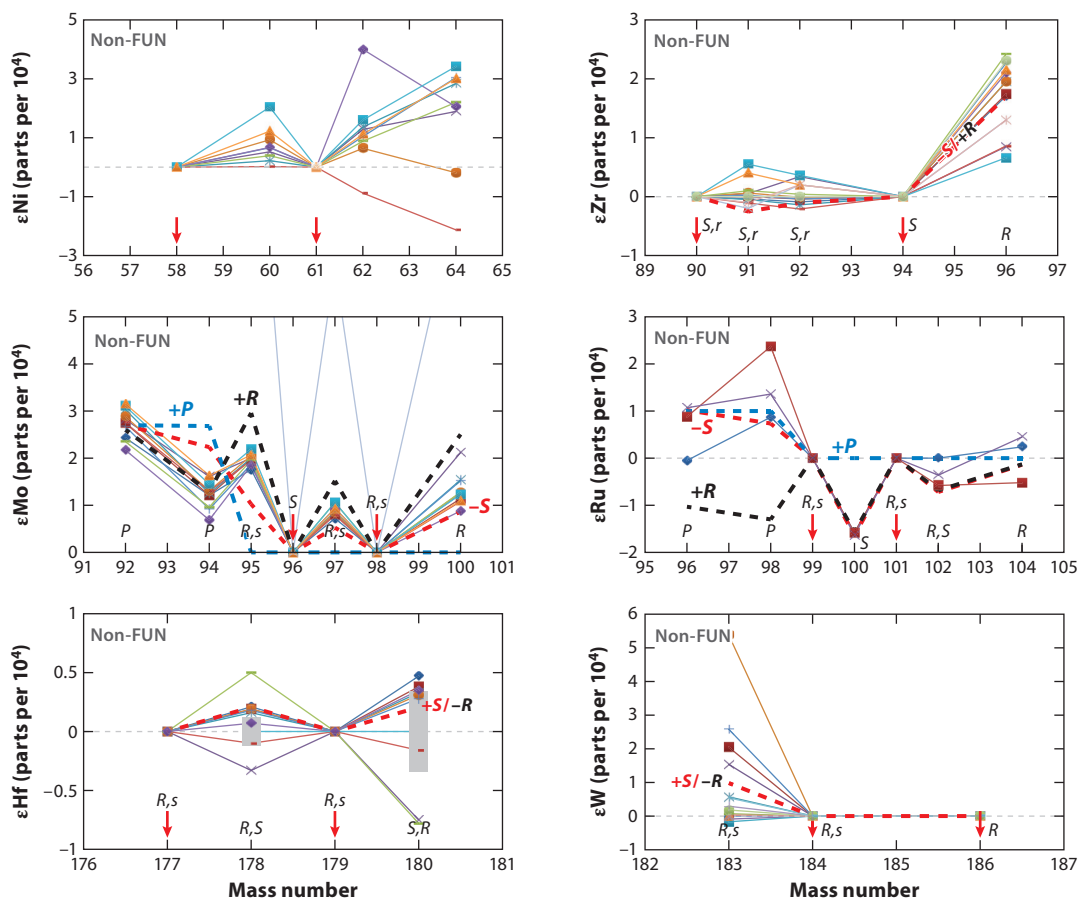


$^{64}\text{Ni}$  (Loss & Lugmair 1990, Völkening & Papanastassiou 1990). Such isotopic anomalies can be produced either in type Ia supernovae (see Section 5.1 for a definition) (Woosley 1997) or possibly in electron-capture core-collapse supernovae ( $\sim 8\text{--}10 M_{\odot}$  progenitor stars in which the collapse is initiated by electron capture in the O+Ne-Mg core; in more massive stars, core collapse is initiated by iron photodisintegration in the Fe core) (Wanajo et al. 2013).

Heavier elements display anomalies that correspond to variations in the  $p$ -,  $s$ -, and  $r$ -processes of nucleosynthesis. The  $s$ -process is a slow neutron-capture process that is introduced in Section 5.1. The  $r$ -process is a rapid neutron-capture process (rapid relative to the rates of radioactive decay)



that produces neutron-rich isotopes and actinides but whose astrophysical setting is still uncertain. The  $p$ -process ( $p$  stands for proton) is most likely a photodisintegration process that takes place in supernovae. For elements that have isotopes produced by all three processes, it is possible to figure out which process is responsible for the isotopic variations because each process leads to a specific pattern (Dauphas et al. 2002b,c). This is because variations in, say, the  $s$ -process due to the presence of mainstream SiC will leave the  $p$ - and  $r$ -process isotopes in solar proportions. **Figure 10** shows the patterns measured in CAIs together with synthetic spectra obtained by varying the contribution of a single nucleosynthetic process at a time. Except for Sr, which shows variations in  $^{84}\text{Sr}$  (Papanastassiou & Wasserburg 1978, Loss et al. 1994, Moynier et al. 2012, Brennecka et al. 2013, Hans et al. 2013, Paton et al. 2013, Shollenberger et al. 2015), the  $p$ -process alone cannot be responsible for the isotopic anomalies measured in CAIs for most elements (Ba, Nd, Sm, Zr, Mo, Ru, Hf, and W) (McCulloch & Wasserburg 1978a,b; Harper et al. 1991b, 1992; Schönbächler et al. 2003; J. Chen et al. 2010; Sprung et al. 2010; Burkhardt et al. 2011; Akram et al. 2013; Brennecka et al. 2013; Kruijter et al. 2014a; Shollenberger et al. 2015). The  $s$ -process is more successful, but it misses the mark on several aspects. Notably, it predicts positive anomalies in  $\epsilon^{130}\text{Ba}$  and  $\epsilon^{132}\text{Ba}$  (see the **Figure 9** caption for definitions of the  $\epsilon$  notation), when in fact no such anomalies are found. It also fails to reproduce the kink in the Mo isotopic pattern at  $^{94}\text{Mo}$ . The  $r$ -process can explain the kink at  $^{94}\text{Mo}$ , but it fails in other respects, most notably in that it cannot



be the cause of the  $^{84}\text{Sr}$  anomalies and it predicts positive anomalies for  $^{144}\text{Sm}$ , when in fact large negative ones are observed. The end-member nucleosynthetic compositions that would need to be admixed with solar composition to explain the isotopic patterns measured in CAIs are plotted in **Figure 11**. Any composition along the lines that connect the nucleosynthetic end-members and the solar composition can be added to or subtracted from the solar composition to reproduce the CAI composition. This diagram reasserts that a single nucleosynthetic component cannot explain isotopic anomalies measured in CAIs. This is true for both FUN and non-FUN (normal) CAIs. Brennecka et al. (2013) noted that CAIs tend to have positive  $r$ -process anomalies (enrichments) in elements of mass number below 140 and negative  $r$ -process anomalies (deficits) in elements of mass number above 140. There is indeed a stark contrast between Zr, which shows an  $r$ -process enrichment, and Nd, which shows an  $s$ -process enrichment, in non-FUN CAIs. However, given the complexity of the patterns observed, it is difficult to interpret the CAI isotopic compositions in terms of  $r$ -process variations alone, and more elements need to be analyzed to get a more holistic view of isotopic variations in refractory inclusions.

### 5.3. Meteorite Acid Leachates and Residues

Isolating presolar grains by digesting away most of the meteorite through various chemicals has been compared to burning the haystack to find the needle. Significant information on the origins of

**Figure 10**

Isotopic anomalies in FUN and non-FUN CAIs. All isotopic compositions are normalized to the terrestrial composition, which is at zero in all these diagrams. Most of the studied CAIs come from the Allende CV carbonaceous chondrite. FUN inclusions represent a small fraction of all the CAIs from Allende (probably less than a few percent), but they display large isotopic anomalies and have been the focus of many studies. For elements such as Ca, Ti, Cr, and Fe, the anomalies in FUN inclusions affect primarily the neutron-rich isotopes. For heavier elements, the anomalies in FUN inclusions correspond to variations in the  $s$ -,  $r$ -, and  $p$ -processes of nucleosynthesis. Similar variations, albeit of much smaller magnitude, are also found in non-FUN (normal) CAIs. The isotopes used for internal normalization are marked with red arrows. For some elements for which no anomalies were detected or the results were marginally significant, typical error bars are shown as gray vertical bands.  $\epsilon E = (R_{\text{sample}}^*/R_{\text{Earth mantle}}^* - 1) \times 10^4$ , where  $R_{\text{sample}}^*$  and  $R_{\text{Earth mantle}}^*$  are the isotopic ratios in the sample and terrestrial mantle, respectively, and the asterisk indicates that the isotopic ratios were corrected by internal normalization to a fixed ratio. Radiogenic isotopes (e.g.,  $^{142}\text{Nd}$ ,  $^{143}\text{Nd}$ ,  $^{176}\text{Hf}$ ,  $^{182}\text{W}$ ) and some very-low-abundance isotopes (e.g.,  $^{46}\text{Ca}$ ,  $^{180}\text{W}$ ) are not plotted because the variations can result from radioactive decay or the data are not available. The red, black, and blue dashed lines are synthetic spectra corresponding to addition to or subtraction from solar composition of  $s$ -,  $r$ -, and  $p$ -processes, respectively (Dauphas et al. 2004, 2014b); the decomposition of solar into  $s$ -,  $r$ -, and  $p$ -processes from Arlandini et al. (1999) was used. Uppercase versus lowercase type in the  $S/s$ ,  $R/r$ , and  $P/p$  labels indicates whether the process is a major or minor contributor, respectively, to the nucleosynthesis of a particular isotope. The following ratios are depicted (the ratios in parentheses are the ones used for internal normalization):  $^i\text{Ca}/^{44}\text{Ca}$  ( $^{42}\text{Ca}/^{44}\text{Ca}$ );  $^i\text{Ti}/^{47}\text{Ti}$  ( $^{49}\text{Ti}/^{47}\text{Ti}$ );  $^i\text{Cr}/^{50}\text{Cr}$  ( $^{52}\text{Cr}/^{50}\text{Cr}$ );  $^i\text{Fe}/^{56}\text{Fe}$  ( $^{54}\text{Fe}/^{56}\text{Fe}$ );  $^i\text{Zn}/^{64}\text{Zn}$  ( $^{68}\text{Zn}/^{64}\text{Zn}$ );  $^i\text{Sr}/^{88}\text{Sr}$  ( $^{86}\text{Sr}/^{88}\text{Sr}$ );  $^i\text{Ba}/^{136}\text{Ba}$  ( $^{134}\text{Ba}/^{136}\text{Ba}$ );  $^i\text{Nd}/^{144}\text{Nd}$  ( $^{146}\text{Nd}/^{144}\text{Nd}$ );  $^i\text{Sm}/^{152}\text{Sm}$  ( $^{147}\text{Sm}/^{152}\text{Sm}$ );  $^i\text{Ni}/^{58}\text{Ni}$  ( $^{61}\text{Ni}/^{58}\text{Ni}$ );  $^i\text{Zr}/^{90}\text{Zr}$  ( $^{94}\text{Zr}/^{90}\text{Zr}$ );  $^i\text{Mo}/^{96}\text{Mo}$  ( $^{98}\text{Mo}/^{96}\text{Mo}$ );  $^i\text{Ru}/^{101}\text{Ru}$  ( $^{99}\text{Ru}/^{101}\text{Ru}$ );  $^i\text{Hf}/^{179}\text{Hf}$  ( $^{177}\text{Hf}/^{179}\text{Hf}$ );  $^i\text{W}/^{184}\text{W}$  ( $^{186}\text{W}/^{184}\text{W}$ ). Data sources: Ca: Lee et al. (1979), Jungck et al. (1984), Niederer & Papanastassiou (1984), Loss et al. (1994), Papanastassiou & Brigham (1989), H.W. Chen et al. (2010), Moynier et al. (2010), Huang et al. (2012), Park et al. (2014), Schiller et al. (2015); Ti: Niemeyer & Lugmair (1981, 1984), Niederer et al. (1981, 1985), Fahey et al. (1987b), Papanastassiou & Brigham (1989), Loss & Lugmair (1990), Loss et al. (1994), Leya et al. (2009), Trinquier et al. (2009), Zhang (2012), Park et al. (2014); Cr: Birck & Allègre (1984, 1988), Papanastassiou (1986), Birck & Lugmair (1988), Loss et al. (1994), Bogdanovski et al. (2002); Fe: Völkening & Papanastassiou (1989); Zn: Loss & Lugmair (1990), Völkening & Papanastassiou (1990); Sr: Papanastassiou & Wasserburg (1978), Loss et al. (1994), Moynier et al. (2012), Brennecka et al. (2013), Hans et al. (2013), Paton et al. (2013), Shollenberger et al. (2015); Ba: McCulloch & Wasserburg (1978a), Harper et al. (1992), Brennecka et al. (2013); Nd: McCulloch & Wasserburg (1978a), Brennecka et al. (2013), Shollenberger et al. (2015); Sm: McCulloch & Wasserburg (1978b), Brennecka et al. (2013), Shollenberger et al. (2015); Ni: Birck & Lugmair (1988); Zr: Harper et al. (1991b), Schönbächler et al. (2003), Akram et al. (2013); Mo: Burkhardt et al. (2011), Brennecka et al. (2013); Ru: J. Chen et al. (2010); Hf: Sprung et al. (2010), Akram et al. (2013); W: Kruijjer et al. (2014a). Abbreviations: CAI, calcium-aluminum-rich inclusion; FUN, fractionated and unknown nuclear effects.

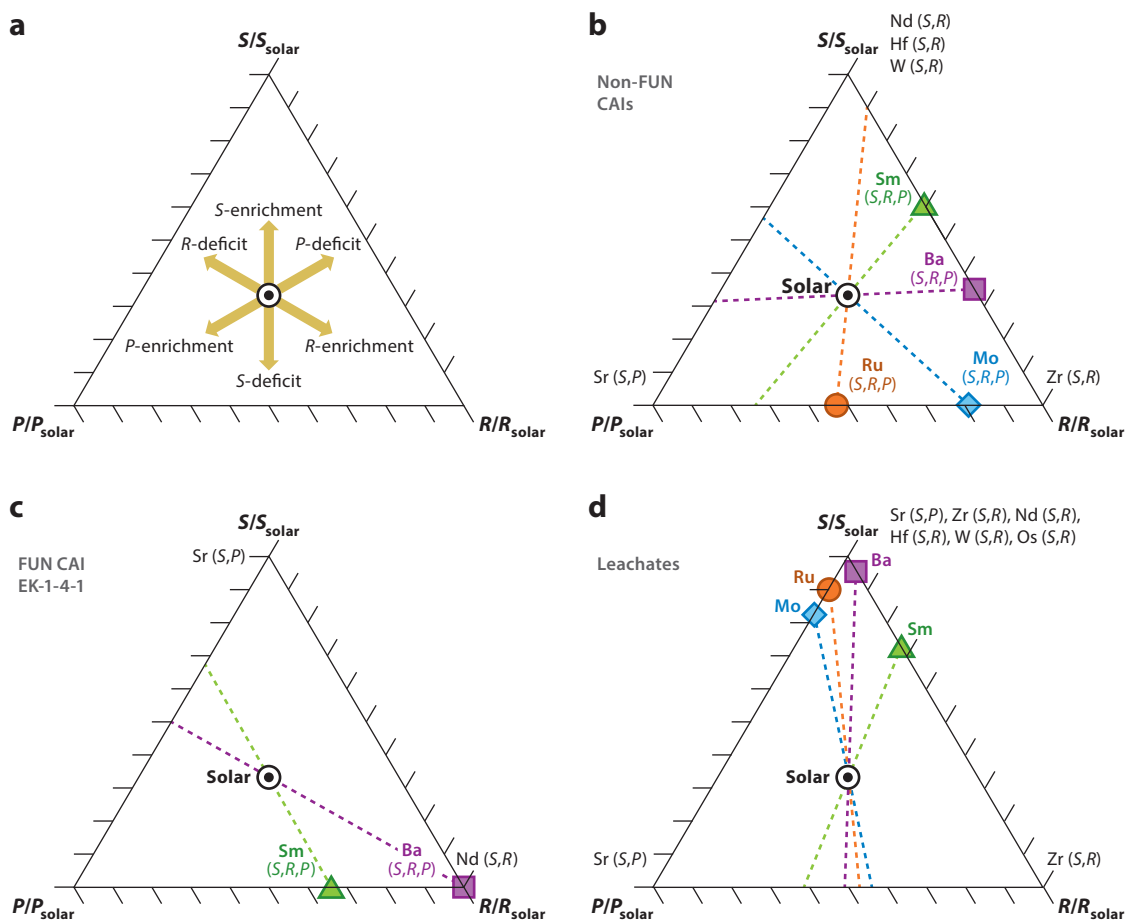


**Figure 11**

(a) Compositions of the nucleosynthetic end-members that need to be admixed with solar composition to explain the isotopic patterns measured in (b) non-FUN CAIs, (c) FUN inclusion EK-1-4-1, and (d) meteorite leachates. The apexes of these ternary diagrams are the *s*-, *r*-, and *p*-process end-members. Taking molybdenum as an example, the solar abundances normalized to  $10^6$  Si are (0.378, 0.236, 0.406, 0.425, 0.244, 0.615, 0.246) for ( $^{92}\text{Mo}$ ,  $^{94}\text{Mo}$ ,  $^{95}\text{Mo}$ ,  $^{96}\text{Mo}$ ,  $^{97}\text{Mo}$ ,  $^{98}\text{Mo}$ ,  $^{100}\text{Mo}$ ) (Anders & Grevesse 1989). The *s*-process component is (0, 0.014, 0.169, 0.425, 0.134, 0.446, 0.001) (Nicolussi et al. 1998, Arlandini et al. 1999). The *r*- and *p*-process components are obtained by subtracting the *s*-process component from solar, and they are (0, 0, 0.237, 0, 0.110, 0.169, 0.245) and (0.378, 0.222, 0, 0, 0, 0), respectively. Mixing those three components in equal proportions produces Mo of solar isotopic composition. The Mo point in panel a corresponds to mixing of 81% of the *r*-process component and 19% of the *p*-process component: (0.0718, 0.0422, 0.192, 0, 0.0891, 0.137, 0.198). Any composition along the dashed lines (mixing between solar and the nucleosynthetic end-members) can be added to (segment tying the solar and calculated nucleosynthetic end-members) or subtracted from (segment away from the solar and calculated nucleosynthetic end-members) the solar composition to reproduce the isotopic anomalies measured in CAIs or in acid leachates. The main processes responsible for the nucleosynthesis of each element are also indicated. For the elements that are only produced by two processes, the position of the element near an apex means that the isotopic anomalies correspond to an enrichment in that process (e.g., Nd in CAIs is enriched in the *s*-process relative to solar). For the leachates, the end-members correspond to relatively chemically resistant leaching steps (*s*-process enrichments; red dashed lines in Figure 10). The end-members for the most soluble fractions would plot at the other ends of mixing lines (*s*-process depletions; blue dashed lines in Figure 10). Abbreviations: CAI, calcium-aluminum-rich inclusion; FUN, fractionated and unknown nuclear effects.

nucleosynthetic anomalies in meteorites can also be gleaned by measuring the isotopic composition of the smoke that is coming off the haystack. This approach was first applied to chromium isotopic analyses by Rotaru et al. (1992). They treated samples of primitive carbonaceous chondrites, including CI chondrites, with acids of increasing strengths: (1) 0.4 M acetic acid for 30 min at 20°C, (2) 8.5 M acetic acid for 1 day at 20°C, (3) 4 M nitric acid for 7 days at 20°C, (4) HCl 3 M–HF 13.5 M for 4 days at 100°C, and (5) HNO<sub>3</sub> 15 M–HF 1 M for 10 days at 150°C. The first leaching steps dissolve minerals that are soluble, such as sulfates and carbonates, and the last ones digest more refractory phases, such as spinel. A motivation for the leachate study was to establish the abundance of the extinct radionuclide <sup>53</sup>Mn ( $t_{1/2} = 3.7$  Myr) at the time when these meteorites were formed by accessing fractions with variable Mn/Cr ratios through partial dissolution. Instead, the leachate fractions showed variable <sup>54</sup>Cr isotopic compositions. Taking the CI chondrite Orgueil as an example, the first three leachates revealed subsolar  $\epsilon^{54}\text{Cr}$  reaching approximately  $-7 \epsilon$  units, and the last two leaching steps revealed positive anomalies reaching approximately  $+100 \epsilon$  units. The isotopic anomalies could be ascribed unambiguously to variations in the neutron-rich isotope <sup>54</sup>Cr rather than any other isotope involved in forming the ratio <sup>54</sup>Cr/<sup>52</sup>Cr or involved in correction of mass-dependent fractionation (<sup>50</sup>Cr/<sup>52</sup>Cr) because  $\epsilon^{53}\text{Cr}$  shows rather subdued variations compared to  $\epsilon^{54}\text{Cr}$ . Dauphas et al. (2002c) used the same leaching approach for molybdenum on the Orgueil meteorite and showed that heavier elements produced by the *s*-, *r*-, and *p*-processes were also variable among meteorite leachates. In the case of Mo, the isotopic anomalies are mainly controlled by variations in the *s*-process (enrichments and deficits) (**Figure 12**). Those studies demonstrated that the solar isotopic composition is actually a mixture, even at a macroscopic scale, of components that have complementary isotopic compositions. Large isotopic anomalies are only found in meteorites that have experienced little parent-body metamorphism. For instance, the CV3.2 chondrite Allende shows no intrinsic heterogeneity in either Cr or Mo isotopes in different leachate fractions, which is understandable because it was heated to a higher degree than CI chondrites by decay of <sup>26</sup>Al, so most presolar grains were likely destroyed (Huss & Lewis 1995) and the isotopic composition was homogenized.

Leachates of primitive meteorites have revealed the presence of isotopic anomalies not only for Cr (Rotaru et al. 1992, Podosek et al. 1997, Qin et al. 2011a) and Mo (Dauphas et al. 2002c, Burkhardt et al. 2012b) but also for Ca (Moynier et al. 2010), Sr (Qin et al. 2011a, Paton et al. 2013, Yokoyama et al. 2015), Zr (Schönbächler et al. 2005), Ru (Fischer-Gödde et al. 2014), Ba (Hidaka et al. 2003, Hidaka & Yoneda 2011, Qin et al. 2011a), Nd (Qin et al. 2011a, Boyet & Gannoun 2013), Sm (Qin et al. 2011a), Hf (Qin et al. 2011a), W (Burkhardt et al. 2012b, Burkhardt & Schönbächler 2015), and Os (Reisberg et al. 2009, Yokoyama et al. 2010). The use of these anomalies to constrain nucleosynthetic processes and to help search for and identify new types of presolar grains is discussed in Section 6.2. Isotopic anomalies in leachate fractions of primitive (minimally metamorphosed) chondrites arise from the fact that mineral grains of different origins display different resistance to the reagents used. This can be a problem when one is trying to retrieve the bulk composition of a meteorite. Indeed, if one uses a chemical digestion technique that cannot completely dissolve some of the most chemically resistant phases, the measured isotopic composition may not be representative of the bulk. Brandon et al. (2005) digested chondrites of various kinds using a Carius tube technique whereby inverse aqua regia is introduced in a borosilicate glass tube containing the sample and the tube is sealed to be then heated to 270°C for 72 h. They found that metamorphosed chondrites showed no or little Os isotopic anomalies because the presolar grains were destroyed by heating on the parent body, whereas primitive meteorites showed large Os isotopic anomalies due to incomplete digestion of a presolar phase rich in *s*-process Os. To get an isotopic composition that is representative of the bulk object, one should therefore use extra care to make sure that even the most chemically

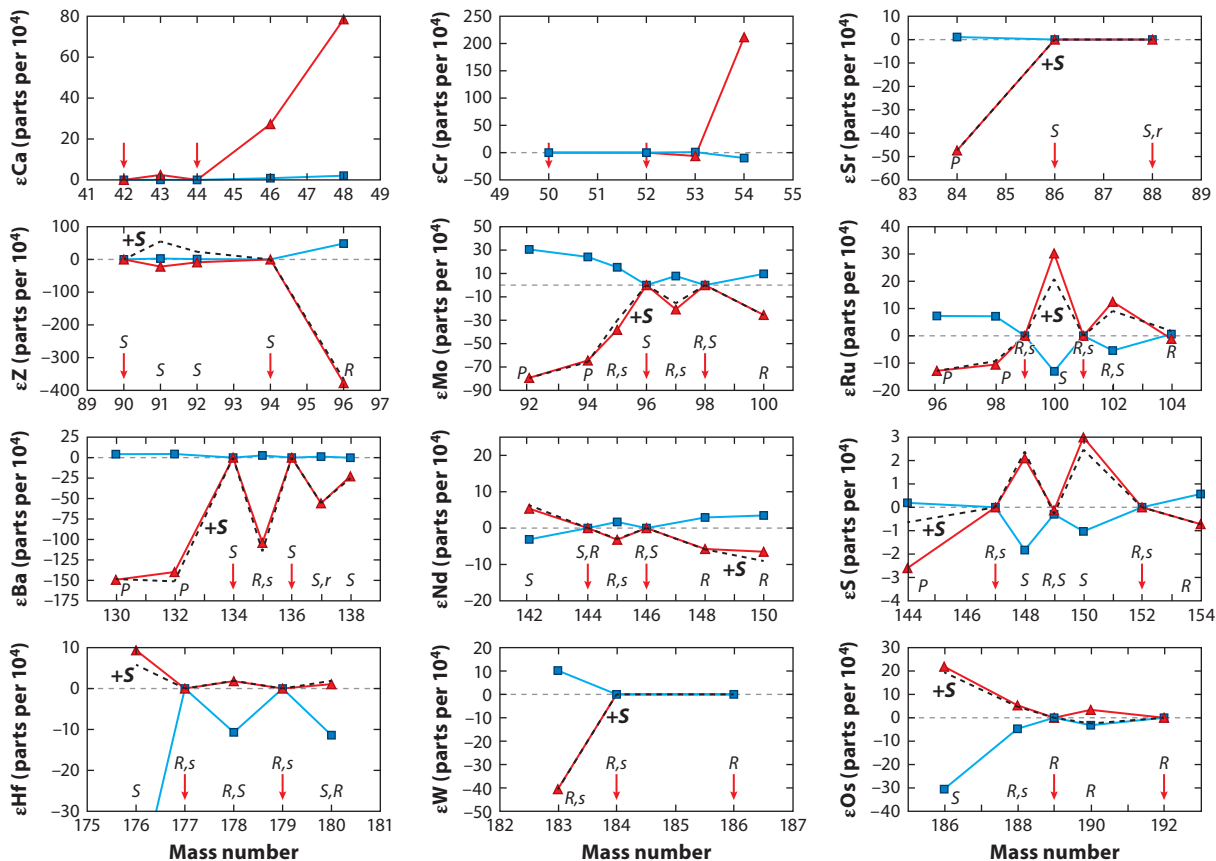


**Figure 12**

Isotopic anomalies in acid leachates and residues of primitive chondrites. For each element, the two most extreme isotope patterns were identified. The blue patterns correspond to relatively mild leaching steps that dissolve easily soluble phases. The red patterns correspond to more aggressive steps or digestion of acid residues. The black dashed patterns are synthetic spectra corresponding to *s*-process enrichments calculated using the predictions of Arlandini et al. (1999) and the mixing equations of Dauphas et al. (2004, 2014b). For most elements, the patterns measured in acid leachates and residues correspond to enrichments or depletions in the *s*-process. Uppercase versus lowercase type in the *S/s*, *R/r*, and *P/p* labels indicates whether the process is a major or minor contributor, respectively, to the nucleosynthesis of a particular isotope. Data sources: Ca: Schiller et al. (2015); Cr: Rotaru et al. (1992), Podosek et al. (1997), Qin et al. (2011a); Sr: Qin et al. (2011a), Paton et al. (2013), Yokoyama et al. (2015); Zr: Schönbächler et al. (2005); Mo: Dauphas et al. (2002c), Burkhardt et al. (2012b); Ru: Fischer-Gödde et al. (2014), M. Fischer-Gödde (personal communication); Ba: Hidaka et al. (2003), Hidaka & Yoneda (2011), Qin et al. (2011a); Nd: Qin et al. (2011a), Boyet & Gannoun (2013); Sm: Qin et al. (2011a); Hf: Qin et al. (2011a); W: Burkhardt et al. (2012b), Burkhardt & Schönbächler (2015); Os: Reisberg et al. (2009), Yokoyama et al. (2010). For Cr, Sr, Zr, Mo, Ru, Ba, Nd, Sm, Hf, and W, the isotope pairs used for internal normalization are the same as in **Figure 10**. For Os, the ratios are  $^{187}\text{Os}/^{189}\text{Os}$  internally normalized to a fixed  $^{192}\text{Os}/^{189}\text{Os}$  ratio.

resistant phases are digested; the safest way to do so is through fusion of the sample before acid digestion (Burkhardt et al. 2011). For metamorphosed chondrites and differentiated meteorites, this is not an issue because presolar grains were destroyed by metamorphism and magmatism.

**Figure 12** plots representative patterns of isotopic anomalies in acid leachates and residues of chondrites (for each meteorite the two most extreme end-member compositions were selected). As is seen in CAIs, the isotopic anomalies for chromium affect primarily the neutron-rich isotope  $^{54}\text{Cr}$ . For heavier elements, the isotopic anomalies in the harsher leaching steps or acid residues are well



reproduced by *s*-process addition to solar composition. For the elements that have contributions of *s*-, *r*-, and *p*-process isotopes, the patterns can be used to identify which nucleosynthetic process is responsible for the isotopic variations. The nucleosynthetic end-members that can explain the isotopic variations for Mo, Ru, Ba, and Sm all plot very close to the *s*-process end-member in the *S-R-P* ternary diagram (**Figure 11**). This clearly demonstrates that one or several carriers of *s*-process anomalies must be responsible for the isotopic variations documented in leachates and acid residues. In that respect, the nucleosynthetic anomalies revealed in leachates, as well as bulk meteorites, are distinct from the isotopic anomalies measured in CAIs, as the latter tend to involve an end-member that is closer to the *r*-process. This is clearly illustrated with Mo, as *r*-process variations lead to an isotopic pattern that has a kink at mass 94 that is seen in CAIs (**Figure 10**), whereas *s*-process variations do not produce such a kink, which is consistent with measurements of meteorite leachates and bulk (**Figure 12**).

Dauphas et al. (2002b,c) showed that from a mass-balance point of view, presolar SiC could explain the Mo isotopic variations measured in leachates and bulk meteorites. A difficulty with this interpretation is that a relatively mild leaching step in the Orgueil carbonaceous chondrites (HCl 3M–HF 13.5 M at 100°C for 4 days) releases an *s*-process-enriched component, while these conditions are not expected to fully digest the micrometer-sized SiC. However, small-sized SiC could possibly be digested in milder acid, as is observed in the case of nanospinels that carry large <sup>54</sup>Cr anomalies (Dauphas et al. 2010, Qin et al. 2011b). Presolar SiC was also invoked as the carrier of *s*-process isotopic anomalies for Sr, Mo, Ba, W, and Os measured in acid leachates and residues (Brandon et al. 2005, Yokoyama et al. 2010, Qin et al. 2011a, Burkhardt et al. 2012b, Paton et al. 2013). Schönbachler et al. (2005) and Reisberg et al. (2009) pointed out that SiC alone cannot explain the large *s*-deficits documented in mild acid leachates, and they argued that other carrier phases must be involved. Presolar SiC grains have been extensively studied using in situ techniques because they are easily isolated, but AGB stars (see Section 5.1 for a definition) also produce copious amounts of other types of dust, such as silicates and oxides (the nature of the condensed dust is influenced by the C/O ratio, which changes as the star ages and becomes more carbon rich). Such grains have been found in meteorites (in particular, presolar silicates seem to be very abundant; see Section 5.1), and phases other than SiC could also control the scale of isotopic anomalies in bulk meteorites, acid leachates, and residues.

## 6. PLANETARY-SCALE ISOTOPE ANOMALIES AND THEIR USE

### 6.1. Macroscopic Anomalies: Presolar Inheritance, Thermal Processing, and Size Sorting

While attempting to establish the temperature of formation of CAIs using oxygen stable isotope thermometry on mineral separates, Clayton et al. (1973) found that the oxygen isotope compositions of these objects did not follow the laws of mass-dependent fractionation, revealing an ~40‰ enrichment in <sup>16</sup>O (**Figure 3**). Subsequent work showed that similar O isotope anomalies, albeit of smaller magnitude, were also present in bulk planetary materials (Clayton 1993, 2003). The currently preferred interpretation is that these reflect the imprint of self-shielding photochemical processes or nebular condensation chemistry (see Section 3.1). Niemeyer (1988) found the first nucleosynthetic anomalies in bulk chondrites for a refractory element in the form of <sup>50</sup>Ti excesses in bulk carbonaceous chondrites; these were subsequently confirmed by Trinquier et al. (2009) and Zhang et al. (2012). After the  $\epsilon^{50}\text{Ti}$  values (see Section 5.2.1 for a definition) are converted to a <sup>49</sup>Ti/<sup>47</sup>Ti normalization, the values that Niemeyer (1988) obtained for CI, CM, CO, and CV chondrites are +1.5, +2.4, +3.0, and +3.0 parts per 10<sup>4</sup>, respectively, whereas more recent

and higher-precision measurements give  $\epsilon^{50}\text{Ti}$  values of +1.9, +3.0, +3.8, and +3.7 parts per  $10^4$ , respectively, for the same meteorite groups (Trinquier et al. 2009, Zhang et al. 2012). These anomalies were found in undifferentiated meteorites, and it was unclear whether such effects would also be present at the scale of bulk planetary objects. Dauphas et al. (2002b) showed that nucleosynthetic anomalies were present for Mo in magmatic iron meteorites, which are thought to be the cores of differentiated planetary bodies whose size can be estimated at 10–100 km in diameter based on metallographic cooling rates (Chabot & Haack 2006). This work demonstrated that nucleosynthetic anomalies were present at a bulk planetary scale for refractory elements. Burkhardt et al. (2012b) confirmed those measurements and extended the database of Mo isotope measurements to most meteorite groups. Planetary-scale isotopic anomalies have now been documented for a wide range of elements, and the list is expanding each year (**Figure 13**) (see **Supplemental Table 1** and its caption for values and references; follow the **Supplemental Material link** in the online version of this article or at <http://www.annualreviews.org>). For elements that possess *p*-process (in addition to *r*- and *s*-process) isotopes in high enough abundance to allow high-precision measurements (Mo and Ru), the isotopic patterns point to an *s*-process deficit of  $\sim 0.01\%$  (Dauphas et al. 2002b, 2004; Burkhardt et al. 2012b; Fischer-Gödde et al. 2015), as is seen, though of larger magnitude, in the leachates.

Several explanations can be considered to explain the presence of  $\epsilon$ -level isotopic anomalies at a macroscopic scale (Dauphas et al. 2002b). One is that they are directly inherited from some large-scale isotopic heterogeneity that was present in the molecular cloud core that collapsed to form the Solar System (Dauphas et al. 2002b). Visser et al. (2009) tracked the fate of different parcels of matter during collapse, and as shown in **Figure 14**, they found that regions of the disk that are further away from the central star and from the midplane tend to originate from more external regions of the cloud core. Significant mixing undoubtedly took place during the evolution of the solar nebula, but isotopic anomalies would not have been completely erased (Boss 2004).

A second category of explanations is that the disk or cloud core started off as isotopically uniform, and that the anomalies measured in bulk planetary materials result from dust processing (Dauphas et al. 2002a). Two processing mechanisms have been envisioned: dynamical and thermal. In the dynamical processing scenario, the carriers of small presolar grains can be decoupled from the carriers of coarser grains that have more averaged compositions, so that material enriched in fine dust could have an isotopic composition distinct from that of material enriched in coarser particles (Dauphas et al. 2010). Inward particle transport associated with gas drag, settling of dust onto the midplane, and turbulences would have provided plenty of opportunities to induce size sorting and create isotopic anomalies. Different chondrite classes have different chondrule and refractory inclusion sizes, presumably reflecting aerodynamical sorting. For example, Murchison has smaller chondrules (millimeter- to centimeter-sized spheres found in abundance in chondrites and thought to have formed in the early Solar System as rapidly quenched molten droplets) and CAIs than Allende even though CAIs seem to have formed up to 3 Myr before chondrules. The second possibility is that thermal processing was responsible for imparting different isotopic compositions to different planetary bodies (Trinquier et al. 2009, Burkhardt et al. 2012b, Burkhardt & Schönbachler 2015, Mayer et al. 2015). Presolar grains condensed at relatively high temperature in the outflows of massive stars. As such, they tend to be more refractory than average Solar System material. The existence of high-*T* constituents such as chondrules and CAIs demonstrates that much of the material in meteorites was processed through high temperatures that induced melting and volatilization. It is conceivable that the carriers of isotopic anomalies, being more refractory, would tend to survive while thermally labile phases were destroyed, producing gas and solid reservoirs with complementary isotopic anomalies.

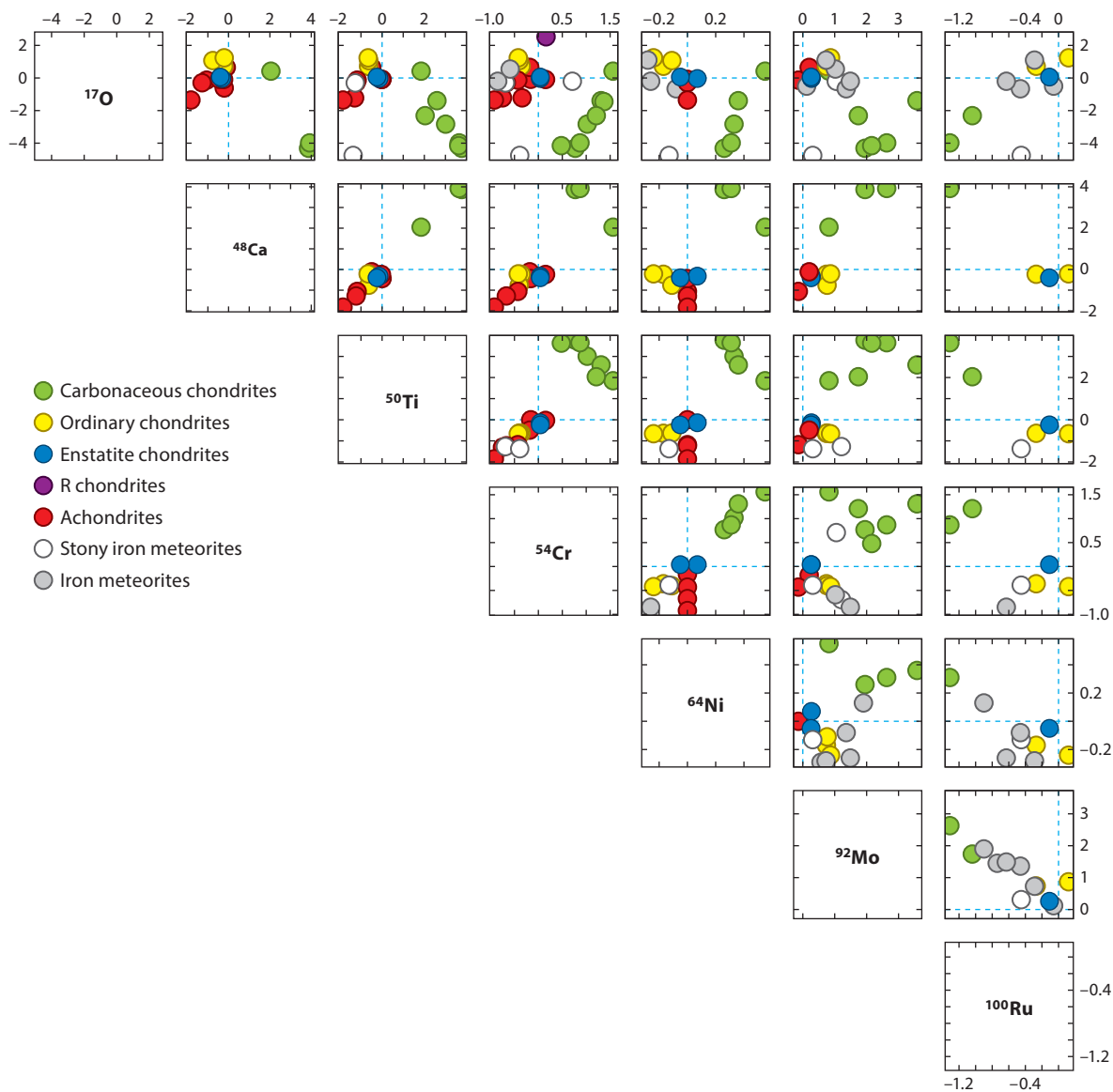


**Figure 13**

Scatter plot matrix of isotopic anomalies in bulk planetary materials. The  $^{17}\text{O}$  anomalies are in  $\Delta$  notation [per mil (‰) variation], whereas all other anomalies are in  $\epsilon$  notation (parts per  $10^4$  variation). The composition of the silicate Earth is at the intersection of the two dashed light blue lines in each panel. The values and associated references are in **Supplemental Table 1**; follow the **Supplemental Material link** in the online version of this article or at <http://www.annualreviews.org>.

The first scenario of grain-size sorting can be tested by looking for correlations between isotopic anomalies and grain-size proxies such as chondrule diameter or matrix fraction (Qin et al. 2010a). Matrix fraction does not correlate with chondrule diameter (Scott & Krot 2005), so the two proxies record different things. Given that we are interested in fractionation of fine-grained presolar dust from coarser average Solar System material, matrix fraction is probably a better proxy. Broad

Supplemental Material

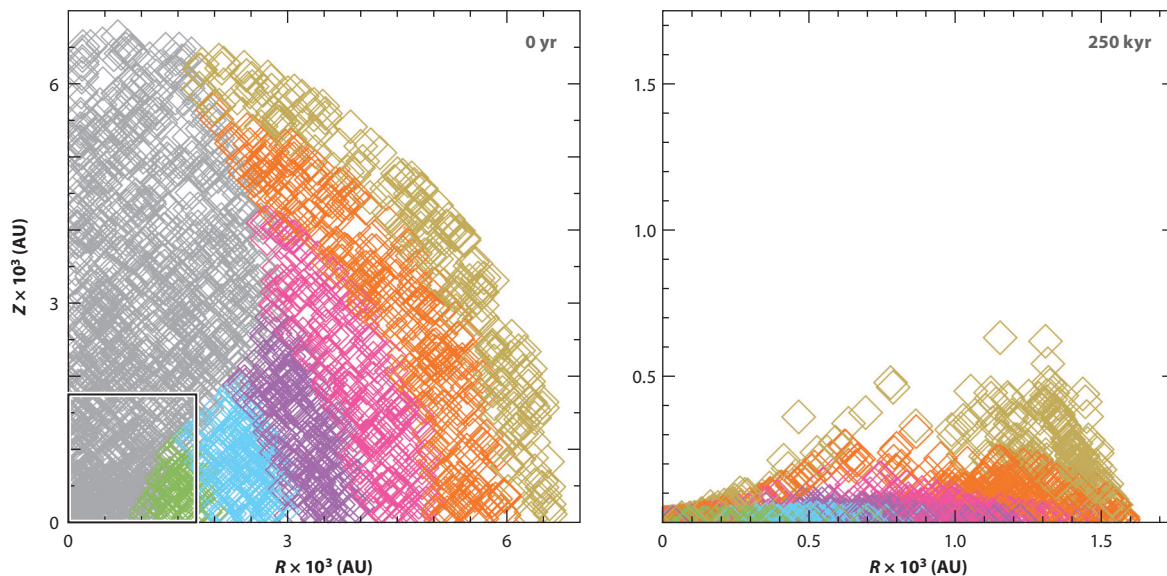


**Figure 14**

Positions of parcels of material during collapse of a molecular cloud core. The left and right panels show the cloud at the onset of collapse and 250 kyr after, respectively. The gray particles in the left panel are the ones that either end up in the central star or are lost through outflows. The other colors trace the fate of different parcels of material during cloud collapse to form a disk. This figure shows that at least until 250 kyr after the onset of collapse, heterogeneities would not have been completely erased. Modified with permission from Visser et al. (2009).

**Supplemental Material**

correlations can be found between some isotopic anomalies ( $^{48}\text{Ca}$ ,  $^{50}\text{Ti}$ ,  $^{62,64}\text{Ni}$ ,  $^{84}\text{Sr}$ ) and matrix percent (**Supplemental Table 1**) that mainly reflect the fact that carbonaceous chondrites are rich in matrix and tend to carry larger isotopic anomalies than other meteorites.

The second scenario of volatility-controlled gas-dust decoupling is more difficult to test because isotopic anomalies also affect refractory lithophile elements, such as Ca and Ti, that are not measurably enriched or depleted in meteorites. One possible way to test this idea is to combine measurements of stable isotopic fractionation with isotopic anomalies, as the evaporation/condensation processes responsible for gas-solid separation are likely to have fractionated the stable isotopic compositions of the elements. Such work has not yet been done.

A striking feature of bulk isotopic anomalies is the dichotomy in composition between carbonaceous and noncarbonaceous chondrites (**Figure 13; Supplemental Table 1**) (Warren 2011). A similar contrast is found in the fractionation pattern of the refractory lithophile element thulium. Whereas carbonaceous chondrites have  $\text{Tm}/\text{Tm}^*$  anomalies ( $\text{Tm}^*$  is the abundance of Tm predicted from interpolation of neighbor rare earth elements) close to CI chondrites, ordinary enstatite chondrites, achondrites, and samples from Earth, Mars, and Vesta display deficits in Tm of  $\sim 3\text{--}4\%$  relative to CI chondrites, which is interpreted to reflect the greater incorporation of refractory dust in carbonaceous chondrites relative to noncarbonaceous chondrites (Dauphas & Pourmand 2015, Barrat et al. 2016). The contrasting compositions of carbonaceous and noncarbonaceous chondrites suggest that the nebular reservoirs from which those objects formed were separated either in time or, more likely, in space and were never allowed to exchange, as intermediate compositions are not found (e.g.,  $\text{Tm}/\text{Tm}^*$  anomalies and  $^{50}\text{Ti}\text{--}^{54}\text{Cr}$  systematics). One possibility is that those reservoirs were physically separated by the opening of a gap in the protoplanetary disk associated with Jupiter formation.

## 6.2. Tracers of Stellar Nucleosynthesis

Presolar grains condensed in the outflows of massive stars that lived and died before the Solar System was formed. While Solar System abundances result from the mixture of multiple nucleosynthetic components (e.g., *s*-, *r*-, and *p*-process components), presolar grains carry almost pure nucleosynthetic signatures, and as such, they are particularly well suited to test our understanding of stellar nucleosynthesis. When they are available, presolar grain samples are almost always preferable to macroscopic samples for studies of stellar nucleosynthesis. However, the carriers of some isotopic anomalies are yet to be identified (e.g.,  $^{48}\text{Ca}$ ), and some elements are too dilute in presolar grains to be measured using in situ techniques. In those cases, studies of leachates or other isotopic anomalies can provide information that would otherwise not be accessible. One such example is osmium, which has not yet been measured in presolar grains. Understanding the nucleosynthesis of osmium is important because production and decay of *r*-process  $^{187}\text{Re}$  into  $^{187}\text{Os}$  ( $t_{1/2} = 41.2$  Gyr) are a potential nuclear cosmochronometer that can help estimate the age of the Galaxy and the duration of stellar nucleosynthesis (Yokoi et al. 1983, Clayton 1988). An important parameter in this calculation is the amount of cosmoradiogenic  $^{187}\text{O}$  in Solar System abundances that comes from decay of  $^{187}\text{Re}$  during the presolar history of the Galaxy (as opposed to primary production of  $^{187}\text{O}$  in stars). To estimate this amount, one has to subtract the amount of  $^{187}\text{Os}$  that comes from *s*-process nucleosynthesis from the solar abundance of  $^{187}\text{Os}$ , meaning that one needs to know precisely and accurately the *s*-process  $^{187}\text{Os}/^{186}\text{Os}$  ratio ( $^{186}\text{Os}$  is a pure *s*-process nuclide).

Brandon et al. (2005) digested various chondrites and measured their Os isotopic compositions. They found that metamorphosed samples had small or unresolvable anomalies, in contrast to samples that had not experienced much metamorphism. This reflects incomplete digestion of chemically resistant presolar grains. Based on these data, Humayun & Brandon (2007) constrained the  $^{190}\text{Os}/^{188}\text{Os}$  ratio of the Maxwellian averaged neutron-capture cross sections (at a given temperature, the energies of the neutrons follow a Maxwell distribution that is used to calculate an average cross section relevant to that temperature) to be  $0.859 \pm 0.042$ . Humayun & Brandon (2007) assumed that the local approximation was valid ( $dN/dt \approx 0$ , so cross section  $\times$  abundance  $\sigma N = \text{constant}$ ) and neglected *s*-process contributions on the normalizing isotopes  $^{189}\text{Os}$  and  $^{192}\text{Os}$ . Reisberg et al. (2009) and Yokoyama et al. (2010) built on this study and analyzed the osmium isotopic composition of leachates of primitive chondrites to try to reduce the contribution of average Solar System composition to the measurement and thus better define the nature of the anomalous component. This, together with improvements in the treatment of the *s*-process, allowed Reisberg et al. (2009) to revise the *s*-process  $^{190}\text{Os}/^{188}\text{Os}$  ratio to  $1.275 \pm 0.043$ , which can only be reproduced in an *s*-process calculation using a ratio for the neutron-capture cross sections of  $\sigma^{190}\text{Os}/\sigma^{188}\text{Os} = 0.69 \pm 0.08$ . Bao et al. (2000) reported a Maxwellian averaged cross section at 30 keV for  $^{190}\text{Os}$  of  $295 \pm 45$  mb, and Mosconi et al. (2010) obtained a cross section for  $^{188}\text{Os}$  of  $294 \pm 14$  mb, corresponding to a  $\sigma^{190}\text{Os}/\sigma^{188}\text{Os}$  ratio of  $1.00 \pm 0.16$ . There is thus a discrepancy between the cross sections obtained from nuclear physics experiments and those obtained from meteorite measurements that has not yet been resolved.

Isotopic anomalies in macroscopic samples and leachates also help guide the search for presolar grains. Measurements of noble gases led to the discovery of presolar grains, and more recently, nanospinel of supernova origin were found through analyses of  $^{54}\text{Cr}$  in leachates and meteorite residues (Dauphas et al. 2010, Qin et al. 2011b).  $^{54}\text{Cr}$  anomalies were detected in a fraction of primitive carbonaceous chondrites that was digested in hot HCl (Rotaru et al. 1992). Further work on the leaching procedure led to the concentration of the carrier of  $^{54}\text{Cr}$  anomalies in some fractions

that exhibited anomalies as high as +1.7%. A microscopic characterization of the samples revealed that the grains were very small, <200 nm and typically ~30 nm, and that the Cr-bearing grains were of spinel mineralogy. Analysis by nanoSIMS showed that some grains in this fraction indeed contain large excess  $^{54}\text{Cr}$  (Dauphas et al. 2010, Qin et al. 2011b). Although spinels are usually thought to be resistant to hot HCl, the nanospinels are of such small size that they can be digested in hot HCl, releasing large  $^{54}\text{Cr}$  anomalies. Further work is needed to tell whether those grains come from type Ia or core-collapse supernovae, but these studies illustrate the importance of leachate studies in the search for new types of presolar grains.

### 6.3. Planetary Genetics

**6.3.1. Meteorite taxonomy.** Isotopic anomalies, in particular  $\Delta^{17}\text{O}$ , are widely used for classification purposes (Clayton 1993, Franchi 2008). In a  $\delta^{17}\text{O}$ - $\delta^{18}\text{O}$  diagram, all meteorites from a single group tend to form a cluster elongated along a line of slope 1/2 (mass-dependent fractionation) characterized by a single  $\Delta^{17}\text{O}$  value relative to the terrestrial fractionation line. A limitation with oxygen is that iron meteorites are often devoid of O or contain O in such low abundance that O measurements are not possible. Other elements with isotopic anomalies, such as Mo, have some chemical affinity with metal, so they can be used to infer relationships among a broader range of meteoritic materials (Dauphas et al. 2004, 2002a,b; Burkhardt et al. 2011). Molybdenum isotope measurements are more challenging than oxygen isotope measurements and are not used routinely for taxonomy purposes, but this may change in the future as analytical capabilities improve. The only isotope anomalies that are used relatively routinely for classification purposes are  $^{17}\text{O}$  (Clayton 1993),  $^{54}\text{Cr}$  (Shukolyukov & Lugmair 2006a, Trinquier et al. 2007, Qin et al. 2010a), and, increasingly,  $^{50}\text{Ti}$  (Trinquier et al. 2009, Zhang et al. 2012). We mention above that for a meteorite to belong to a specific group, it needs to have the isotopic anomaly ( $\Delta^{17}\text{O}$ ,  $\varepsilon^{50}\text{Ti}$ , and  $\varepsilon^{54}\text{Cr}$ ) characteristic of that group. This is not completely true, as a certain level of isotopic scatter is allowed. The most striking examples of that are Ibitira and a few other anomalous eucrites (PCA91007, Pasamonte, A-881394, Bunburra R) that are chemically and mineralogically similar to other eucrites yet show  $\Delta^{17}\text{O}$  isotopic anomalies that can reach +0.15‰ relative to other HED meteorites (Wiechert et al. 2004, Scott et al. 2009). These anomalous eucrites have petrology and ages compatible with the eucrite group (except possibly Ibitira) (Mittlefehldt 2005). When plotted in  $^{53}\text{Mn}$ - $^{53}\text{Cr}$  ( $t_{1/2} = 3.7$  Myr) (Lugmair & Shukolyukov 1998, Trinquier et al. 2008) or  $^{60}\text{Fe}$ - $^{60}\text{Ni}$  ( $t_{1/2} = 2.6$  Myr) (Tang & Dauphas 2012) diagrams, they plot on the same bulk meteorite isochrons as other HED meteorites, suggesting that they differentiated at the same time. HED meteorites are differentiated meteorites, meaning that their parent body, presumably Vesta (Drake 2001, McSween et al. 2013), must have been at least partially molten. In the process of melting, one would expect the isotopic anomaly signatures to be homogenized, so that a given body should have a fixed anomaly. At the present time, it is unknown whether this statement is correct, so that the anomalous eucrites come from a different parent body, or whether isotopic heterogeneities can survive partial melting and magmatic differentiation processes. Geochronologic inferences support derivation of anomalous and nonanomalous eucrites from the same parent body, suggesting that isotopic heterogeneities can survive planetary differentiation processes.

**6.3.2. Planetary genetics and relationships between Earth and meteorites.** Processes taking place on planetary bodies, at both low and high temperatures, can impart stable isotopic variations to rocks. However, for the most part (exceptions to this rule are nuclear field shift effects and other exotic processes discussed in Sections 3 and 4), those variations are mass dependent, meaning that the isotopic anomalies do not change. Isotope variations can thus help us see through subsequent

planetary processes to identify the nature of the material that made Earth and other planets. Among large planetary bodies, the isotopic compositions are known precisely for Earth (at least its mantle, because, as discussed below, it need not be representative of the bulk planet for siderophile elements), the Moon, and Mars. A prerequisite for some assemblage of meteorites to be considered as building blocks of Earth is that they should reproduce its isotopic composition. Models attempting to reproduce the composition of planets usually start with chondrites. Achondrites are not included because the bulk chemical compositions of their parent bodies are very uncertain. For Mars, Lodders & Fegley (1997) considered a model comprising 85% H + 11% CV + 4% CI, whereas Sanloup et al. (1999) considered a model comprising 55% H + 45% EH. Tang & Dauphas (2012) showed that Sanloup et al.'s (1999) mixture is viable, as it reproduced the isotopic composition of Mars for most isotopic systems, but that Lodders & Fegley's (1997) mixture fails to reproduce the  $\Delta^{17}\text{O}$  value of SNC meteorites. Even if a specific chondrite mixture reproduces the composition of a planet, it does not mean that the planet is made of that material. In the case of Earth, it is well documented that the isotopic compositions of enstatite chondrites match those of Earth for most isotopic systems:  $^{17}\text{O}$ ,  $^{48}\text{Ca}$ ,  $^{50}\text{Ti}$ ,  $^{54}\text{Cr}$ ,  $^{64}\text{Ni}$ ,  $^{92}\text{Mo}$ , and  $^{100}\text{Ru}$  (**Figure 13**) (Dauphas et al. 2014b). This led Javoy and coworkers to suggest that Earth was made of enstatite chondrites (Javoy 1995, Javoy et al. 2010). Because isotopic anomalies in these elements are not all correlated (**Figure 13**), it is difficult to imagine that the similarity in isotopic composition between Earth and enstatite chondrites could be just a coincidence, and Dauphas et al. (2014b) showed that, indeed, no chondrite mixture can reproduce the terrestrial isotopic composition unless the mixture comprises >80% enstatite-like meteorites. A major difficulty, however, is that enstatite chondrites have low Mg/Si ratios, while the silicate Earth has a high Mg/Si ratio, which would require an unrealistic amount of Si in Earth's core (20–30 wt%, whereas geophysical observations constrain that number to <11 wt%; Hirose et al. 2013) or the presence of a hidden Si-enriched reservoir in the deep mantle (Javoy et al. 2010, Kaminski & Javoy 2013). Most likely, Earth-forming material and enstatite chondrites formed from the same isotopic reservoir but diverged in their chemical evolutions due to nebular processes, such as forsterite-gas decoupling (Dauphas et al. 2014a, 2015b).

Earth is thought to have formed by collisions of embryos that formed at various planetary radii (Chambers & Wetherill 1998). The embryos, in contrast, are thought to have formed from relatively narrow feeding zones, such that their compositions should match that of the protosolar nebula at the time and place at which they formed (Wetherill & Stewart 1989, Kokubo & Ida 1998). If the disk were isotopically heterogeneous, then the various embryos that formed Earth would have had different compositions, and the Earth that grew from them would not look like any of them (Pahlevan & Stevenson 2007). Instead, Earth's composition matches well that of a meteorite group: enstatite chondrites. The easiest explanation for this similarity is that the inner part of the Solar System (all the way to the present orbit of Mars) had uniform isotopic composition similar to that of Earth and enstatite chondrites but that the building blocks of Earth had different chemical composition than enstatite chondrites and are missing entirely from meteorite collections (Dauphas et al. 2014a,b).

Isotopic anomalies in Mo and Ru can also help constrain the nature of the material that fell on Earth before and after completion of core formation (Dauphas et al. 2004). Molybdenum is a moderately siderophile element, meaning that when the core formed, a significant amount of Mo stayed behind in the mantle. In contrast, Ru is a highly siderophile element, meaning that when the core formed, it was completely scavenged in Earth's core. The mantle was replenished in Ru and other highly siderophile elements by accretion of a late veneer after the completion of core formation. Molybdenum and ruthenium in Earth's mantle thus record different epochs of Earth's accretion history. Taking *W* as a proxy for Mo in the model of Rubie et al. (2011), Mo

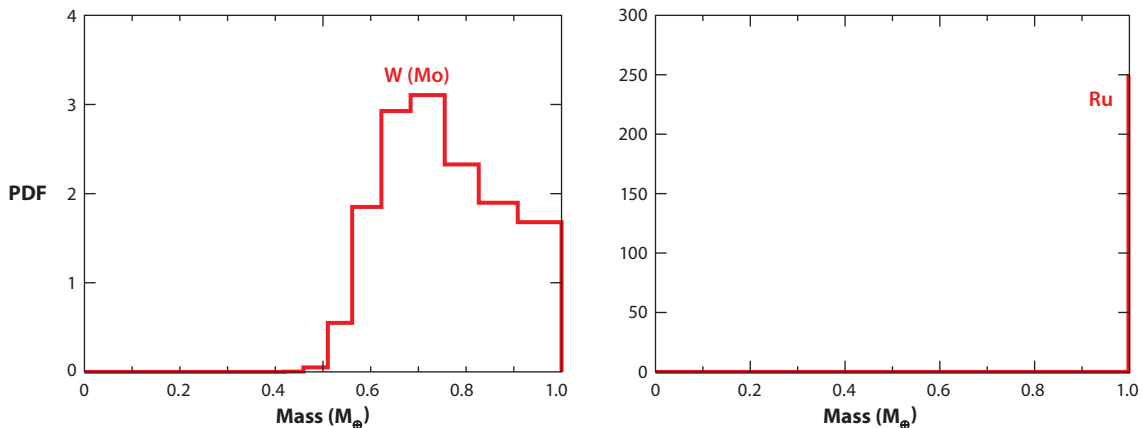


**Figure 15**

Mass (age) spectra of Mo and Ru in Earth's mantle. The W (taken as a proxy for Mo) curve was calculated using the model output of Rubie et al. (2011). These curves give the probability for atoms in Earth's mantle to have come from a given period in Earth's mass accretion history (mass is given as a proxy for time in this diagram). For example, the fraction of Mo atoms in Earth's mantle that were delivered during the first half of Earth's mass accretion history is given by the integral  $\int_0^{0.5} \text{PDF}(m)dm$ . This shows that Mo was delivered to Earth's mantle during the second half of Earth's history, whereas Ru was delivered as part of a later veneer during the last 0.4% of Earth's accretion history. The atoms delivered before those time periods partitioned into metal and were scavenged into Earth's core. Abbreviation: PDF, probability distribution function.

would have been delivered to Earth mostly during the second half of Earth's accretion history (**Figure 15**). Before that, Mo would have been scavenged into Earth's core. Ruthenium would have been scavenged into Earth's core throughout its history, except for the last 0.1–0.5% late veneer delivery (Chou 1978, Dauphas & Marty 2002, Walker 2009).

In meteorites,  $\epsilon^{92}\text{Mo}$  and  $\epsilon^{100}\text{Ru}$  isotope anomalies form a tight correlation that corresponds to a deficit in the *s*-process, consistent with a heterogeneous distribution of mainstream SiC among planetary bodies at the ~20% level (Dauphas et al. 2002b,c, 2004; J. Chen et al. 2010; Burkhardt et al. 2011; Fischer-Gödde et al. 2015) (**Figure 16**). Usually, binary mixing in such an isotopic diagram is characterized by a curve whose curvature coefficients are given by  $(\text{Mo/Ru})_1/(\text{Mo/Ru})_2$ , where 1 and 2 correspond to the two mixing end-members (solar and *s*-process in this case). The reason why mixing is depicted as a straight line is that the isotopic variations in bulk meteorites represent a very small fraction of the isotopic range spanned by the two mixing end-members. This is formalized in the following equation (Dauphas et al. 2004, 2014b), which relates  $\epsilon$ -level anomalies (A and B are two elements; the isotopic ratios  ${}^j\text{A}/{}^i\text{A}$  and  ${}^q\text{B}/{}^p\text{B}$  are corrected by internal normalization by fixing  ${}^k\text{A}/{}^i\text{A}$  and  ${}^r\text{B}/{}^p\text{B}$  ratios, respectively, to constant values):

$$\epsilon^{j/i}\text{A} = \frac{\rho_{\text{A}}^{j/i} - \frac{\mu_{j/i}}{\mu_{k/i}} \rho_{\text{A}}^{k/i}}{\rho_{\text{B}}^{q/p} - \frac{\mu_{q/p}}{\mu_{r/p}} \rho_{\text{B}}^{r/p}} C_{\text{pB}}^{i\text{A}} \epsilon^{q/p}\text{B}, \quad (37)$$

where  $\rho_{\text{E}}^{j/i} = ({}^j\text{E}/{}^i\text{E})_{\text{star}}/({}^j\text{E}/{}^i\text{E})_{\text{Sun}} - 1$ ,  $\mu_{\text{E}}^{j/i} = \ln(m_{j\text{E}}/m_{i\text{E}})$  arises from the internal normalization procedure, and  $C_{\text{pF}}^{i\text{E}} = ({}^i\text{E}/{}^p\text{F})_{\text{star}}/({}^i\text{E}/{}^p\text{F})_{\text{Sun}}$  is the curvature coefficient.

If one considers two isotopic ratios  ${}^j\text{A}/{}^i\text{A}$  and  ${}^q\text{A}/{}^i\text{A}$  of the same element, both internally normalized by fixing the ratio  ${}^k\text{A}/{}^i\text{A}$  to a constant value, then the relationship becomes

$$\epsilon^{j/i}\text{A} = \frac{\rho_{\text{A}}^{j/i} - \frac{\mu_{j/i}}{\mu_{k/i}} \rho_{\text{A}}^{k/i}}{\rho_{\text{A}}^{q/i} - \frac{\mu_{q/i}}{\mu_{k/i}} \rho_{\text{A}}^{k/i}} \epsilon^{q/i}\text{A}. \quad (38)$$



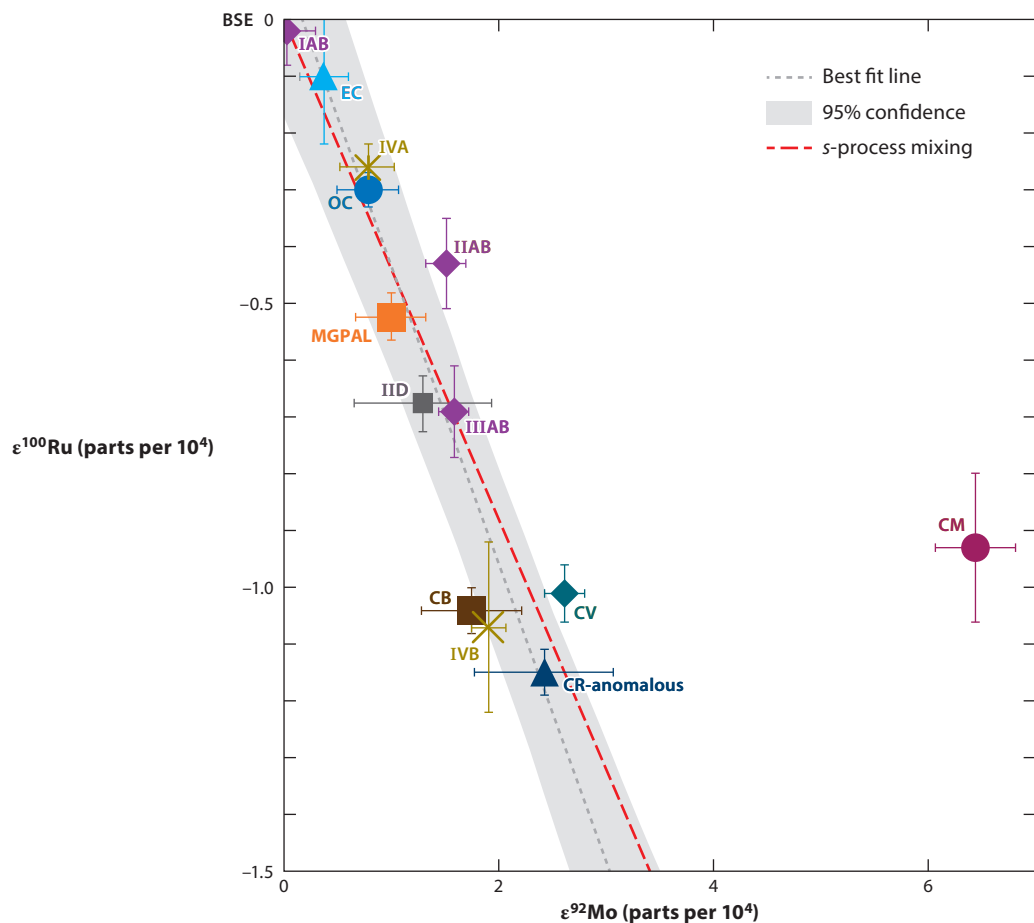


**Figure 16**

Correlation between nucleosynthetic anomalies for Mo and Ru. Mo in Earth's mantle was delivered in the second half of Earth's accretion history, whereas Ru was delivered as part of the late veneer during the last 0.4% of Earth's accretion (**Figure 15**). The fact that Earth's mantle plots on the correlation line defined by meteorites [(0,0) coordinates] suggests that the material accreted by Earth before and after completion of core formation did not change drastically in its isotopic characteristics (Dauphas et al. 2004, Fischer-Gödde et al. 2015). Data sources: Dauphas et al. (2002a,b, 2004), J. Chen et al. (2010), Burkhardt et al. (2011), Fischer-Gödde et al. (2015).

The Mo-Ru anomalies can be used to evaluate whether the material that was accreted by Earth changed when Earth accreted the last 50% or 0.5% of its mass (**Figure 15**). Because Mo and Ru were delivered to Earth's mantle at different stages of its accretion, there is no requirement for Earth's mantle to plot on the cosmic correlation defined by meteorites (**Figure 16**). For instance, let us consider a scenario whereby Earth starts accreting enstatite-like material and the late veneer is made of CV chondrites. In such a case, the  $\epsilon^{92}\text{Mo}$  value would be that of enstatite chondrites ( $\sim 0$ ) (Dauphas et al. 2002a, Burkhardt et al. 2011), whereas the  $\epsilon^{100}\text{Ru}$  value would be that of CV chondrites ( $-1$ ) (J. Chen et al. 2010, Fischer-Gödde et al. 2015), and the silicate Earth would plot off the Mo-Ru correlation. Instead, the measurements show that the silicate Earth plots on the correlation, suggesting that the material that was accreted by Earth before and after the completion of core formation did not change in its isotopic characteristics.

**6.3.3. Relationship between Earth and the Moon.** The most successful model to account for the characteristics of the Earth–Moon system, notably its angular momentum, the mass of the Moon, and the small core of the Moon, is impact between a Mars-sized embryo at a velocity that just exceeds the mutual escape velocity and an impact angle of around 45° (Hartmann & Davis 1975, Cameron & Ward 1976, Canup & Asphaug 2001). A strong appeal of this model, which is known as the canonical giant impact model, is that those conditions are likely for collisions between protoplanets and embryos when terrestrial planets formed. A prediction of this model is that most of the Moon (>80%) would have been derived from the impactor, named Theia (Canup et al. 2013). If Theia had a different composition than the proto-Earth for any of the elements that display isotopic anomalies, as was proposed by Pahlevan & Stevenson (2007), then the Moon should have inherited this composition and should be distinct from Earth. A difficulty in conjecturing Theia’s composition is that the isotopic gradient of the protoplanetary disk is unknown. To constrain it, Pahlevan & Stevenson (2007) took the compositions of Earth and Mars as anchors. They examined the outcomes of *n*-body simulations and fixed the gradient in  $\Delta^{17}\text{O}$  so as to reproduce the Earth–Mars difference in  $\Delta^{17}\text{O}$  between Earth and Mars analogs. Based on this inferred  $\Delta^{17}\text{O}$  gradient, they were able to look at the statistical likelihood of giant impacts with an impactor that has the same isotopic composition as the proto-Earth. They concluded that this was very unlikely. To reconcile the very similar  $\Delta^{17}\text{O}$  values of Earth and the Moon (Clayton & Mayeda 1975, Wiechert et al. 2001, Spicuzza et al. 2007, Hallis et al. 2010, Herwartz et al. 2014), Pahlevan & Stevenson (2007) proposed a new model whereby the impactor had an isotopic composition distinct from that of the proto-Earth but the terrestrial magma ocean equilibrated with the protolunar disk in the aftermath of the giant impact. This model predicted that the Moon should have Si isotopic composition distinct from that of Earth (due to  $\text{SiO}_{\text{gas}}$ -silicate liquid isotopic fractionation) (Pahlevan et al. 2011), which has not been found (Armytage et al. 2012). Furthermore, this equilibration scenario involving gas-mediated exchange should work only for elements that are relatively volatile. Refractory elements such as Ca or Ti would not be able to equilibrate isotopically because they have low vapor pressures, and the timescale for transfer between the molten protolunar disk and the Earth–Moon atmosphere would be comparable to the lifetime of the lunar disk (Zhang et al. 2012). Thus, if the proto-Earth and Theia had distinct isotopic compositions for refractory elements such as Ti, a difference should be detectable between Earth and the Moon. Zhang et al. (2012) measured at high precision the Ti isotopic composition of lunar rocks. A complication with these samples is that they were exposed to galactic cosmic rays for an extended time, and capture of secondary neutrons produced by interaction between galactic cosmic rays and lunar rocks modified the isotopic composition of Ti. Indeed, Zhang et al. (2012) showed that the isotopic composition of Ti correlated with isotopic variations in Sm and Gd, which are highly sensitive to neutron capture. After correcting for these cosmogenic effects, Zhang et al. (2012) found that Earth and the Moon have identical  $\epsilon^{50}\text{Ti}$  isotopic compositions within uncertainty ( $\pm 0.04$  parts per  $10^4$ ), whereas variations documented among various meteorite groups cover a range of 6 parts per  $10^4$  (**Figure 17**). The Moon also has the same  $\epsilon^{54}\text{Cr}$  isotopic composition as Earth (Lugmair & Shukolyukov 1998; Qin et al. 2010a,b), and recent measurements have failed to detect any difference in the  $\epsilon^{48}\text{Ca}$  isotopic compositions of terrestrial and lunar rocks (Dauphas et al. 2015a). This level of similarity for highly refractory elements such as Ti or Ca is difficult to reconcile with the view that the impactor had a composition different from that of the proto-Earth, and that the more volatile elements equilibrated isotopically in the aftermath of the giant impact.

To solve the lunar isotopic crisis, Čuk & Stewart (2012) and Canup (2012) proposed new versions of the giant impact scenario. Čuk & Stewart (2012) proposed that the Moon formed by a hypervelocity impact ( $20 \text{ km s}^{-1}$ ) of a small-sized impactor ( $0.05 M_{\oplus}$ ) on a fast spinning

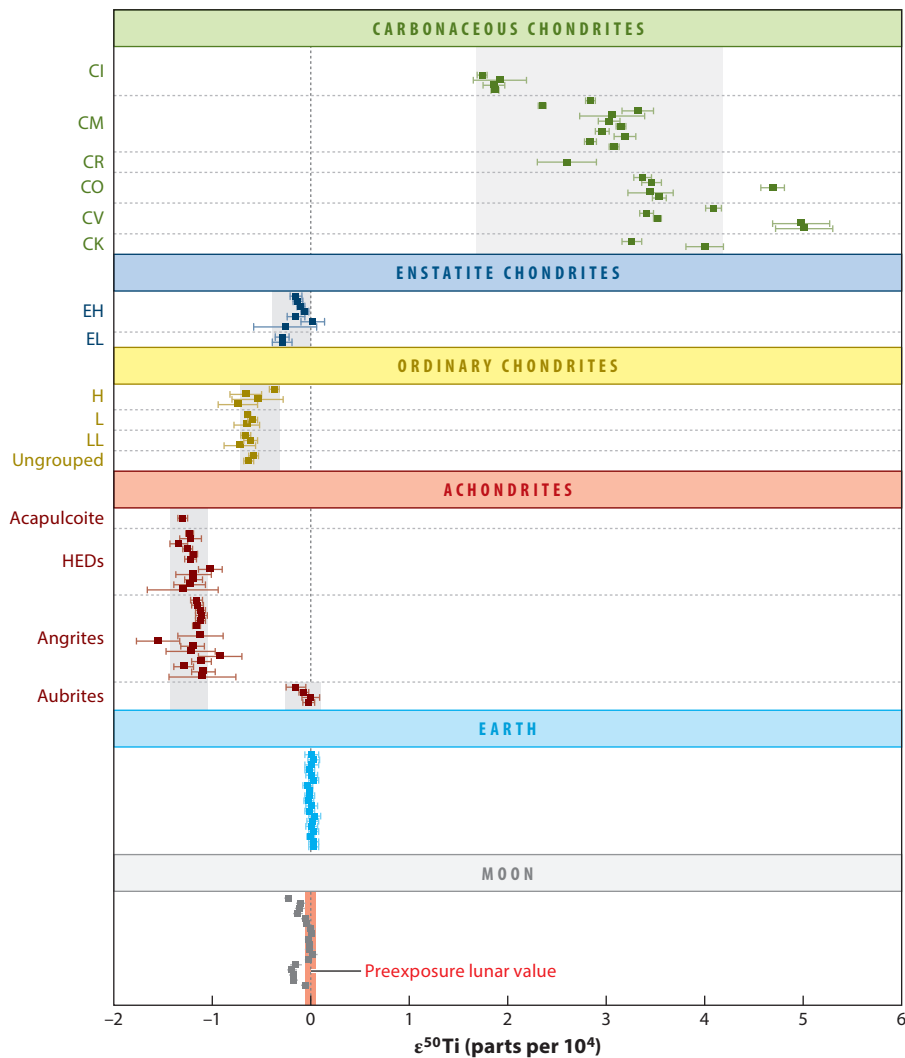


**Figure 17**

Titanium isotopic anomalies ( $\epsilon^{50}\text{Ti}$ ) in meteorites, Earth, and the Moon (Zhang et al. 2012). After correction for cosmogenic effects, the  $\epsilon^{50}\text{Ti}$  value of the Moon is indistinguishable from that of Earth within  $\pm 0.04 \epsilon$  units, whereas meteorites show a range in  $\epsilon^{50}\text{Ti}$  values of  $\sim 6 \epsilon$  units. This cannot be reconciled with models that assume gas-mediated equilibration between Earth and the Moon (Pahlevan & Stevenson 2007) and suggests instead that the Moon-forming impact departed from the canonical impact scenario (Canup 2012, Āuk & Stewart 2012) or that the Moon-forming impactor had Ti isotopic composition very similar to that of Earth (Dauphas et al. 2014a).

proto-Earth (2.3-h period). The preimpact proto-Earth of Āuk & Stewart (2012) displays a significant equatorial bulge, and the model shares similarities with the fission scenario of Darwin in that it allows for a large fraction of the Moon to be derived from the proto-Earth. Canup (2012) proposed that the Moon formed from the collision of two equal-sized bodies of approximately half the present Earth mass, so that Earth and the Moon would have received equal shares of the two

impactors. Those two models predict that the angular momentum of the postimpact Earth-Moon system was much higher than the present one, but Čuk & Stewart (2012) proposed that some of this angular momentum could be transferred to the rotation of Earth around the Sun. Work is still being done to evaluate the feasibility of this process (Wisdom & Tian 2015), but an important issue with these scenarios is that, unlike the canonical scenario, they require impact conditions (impactor size, impact angle, velocity, rotation rate of the proto-Earth) that are unlikely (Canup 2014).

Dauphas et al. (2014a,b) examined the geochemical constraints on the nature of the material that made Earth. The fact that Earth matches the isotopic composition of enstatite chondrites very closely (**Figure 13**) cannot be a coincidence, as isotopic anomalies are not correlated, and mixtures of materials of disparate compositions would not explain why Earth has the same composition as a particular chondrite group that represents a snapshot in time and space of the composition of the protosolar nebula. As discussed above, the fact that the silicate Earth plots on the Mo-Ru isotope correlation (**Figure 16**) also suggests that the material accreted by Earth did not change in composition before or after core formation (Dauphas et al. 2004). Based on this evidence, Dauphas et al. (2014b) suggested that the inner part of the protosolar nebula had uniform isotopic composition, similar to that of enstatite chondrites (this reservoir was called inner disk uniform reservoir, or IDUR). All the embryos that made Earth had the same isotopic composition as enstatite chondrites (but not necessarily the same chemical composition), including the Moon-forming impactor. This naturally explains why the Moon has the same isotopic composition as Earth. Mastrobuono-Battisti et al. (2015) reevaluated the basis of Pahlevan & Stevenson's (2007) argument that the impactor should have  $^{17}\text{O}$  isotopic composition distinct from that of Earth. Using a statistically more representative set of simulations, they concluded that having an impactor with the same isotopic composition as the proto-Earth was quite likely, with a probability of  $\sim 20\%$ . Doing a similar analysis, Kaib & Cowan (2015) obtained a lower number ( $\sim 5\%$  probability) and commented that this remains a low-probability event, although not as rare as what was inferred by Pahlevan & Stevenson (2007). Those models were focused on explaining the similarity in oxygen isotopic composition between Earth and the Moon and still allowed for a large radial gradient in isotopic composition, with the terrestrial composition representing a mixture of bodies with disparate compositions. We see this as unlikely because, as pointed out by Dauphas et al. (2014b), the isotopic anomalies are not all correlated (e.g.,  $^{17}\text{O}$  and  $^{50}\text{Ti}$ ; see **Figure 13**), so getting the right composition for  $^{17}\text{O}$  by mixing does not mean that  $^{50}\text{Ti}$  or  $^{54}\text{Cr}$  will also have the right isotopic compositions. It also does not explain why Earth has the same isotopic composition as enstatite chondrites. The simplest explanation remains that the inner part of the Solar System had uniform isotopic composition and that all the large impactors that made Earth had isotopic compositions similar to one another and to enstatite chondrites (the IDUR).

A difficulty that remains in regards to the composition of the Moon is the similarity in the  $^{182}\text{W}$  isotopic compositions of lunar and terrestrial rocks (Kruijer et al. 2015, Touboul et al. 2015). Indeed, this composition reflects the time evolution of the Hf/W ratio while  $^{182}\text{Hf}$  was still alive ( $^{182}\text{W}$  is produced by decay of  $^{182}\text{Hf}$  with a half-life of  $\sim 9$  Myr). There may be a small difference in the  $^{182}\text{W}$  isotopic composition of the terrestrial and lunar mantles that can be accounted for by a difference in the masses of the late veneers on the Moon and Earth, suggesting that the lunar and terrestrial mantles started with similar  $^{182}\text{W}$  isotopic compositions. Another puzzle is that the lunar and terrestrial mantles also seem to have very similar Hf/W ratios (Münker 2010, Dauphas et al. 2014a). No model can naturally explain this similarity. Dauphas et al. (2014a) presented an inversion technique to calculate the Hf/W ratios and  $\epsilon^{182}\text{W}$  values of the impactor and proto-Earth mantles and showed that those compositions would be in line with what would be expected for a rapidly formed embryo and a protoplanet that grew over an extended period of

time. The similarity in W isotopic composition between the lunar and terrestrial mantles may just be a coincidence, like the fact that the Moon is 400 times closer to us and 400 times smaller in diameter than the Sun, so that total lunar eclipses can perfectly obscure the Sun, leaving just the solar corona visible for astronomers to observe.

**6.3.4. Tracers of parent-body processing.** Meteorite parent bodies were affected by impacts, aqueous alteration, and thermal metamorphism. For elements that are volatile, and in particular for noble gases, the destruction of presolar grains by thermal metamorphism can have a strong influence on the isotopic composition of the meteorite (Huss & Lewis 1995). The effect of thermal metamorphism is also blatant in leachate studies, as leachate fractions in metamorphosed meteorites usually have uniform isotopic compositions because presolar grain destruction and diffusion have isotopically homogenized the samples (Rotaru et al. 1992, Dauphas et al. 2002c, Brandon et al. 2005).

## 7. TROUBLEMAKERS IN GEOCHRONOLOGY

The radiogenic component of isotopic variations is usually calculated by examining departures from mass-dependent fractionation for the radiogenic isotope. For this calculation to be correct, one must make sure that no other source of isotope variation is present. Cosmogenic effects produced by irradiation of the samples by cosmic rays are usually easily identified as they correlate with other proxies of space exposure. Other sources of isotopic anomalies must also be considered, in particular those that have a nucleosynthetic origin, and possibly nuclear field shift effects. Below, we review the radioactive isotope systems that are most severely affected by the presence of isotopic anomalies.

### 7.1. $^{26}\text{Al}$ - $^{26}\text{Mg}$ ( $t_{1/2} = 0.7$ Myr)

The initial  $^{26}\text{Al}/^{27}\text{Al}$  ratio in refractory inclusions in meteorites was established at  $\sim 5 \times 10^{-5}$  using a  $^{26}\text{Mg}/^{24}\text{Mg}$ - $^{27}\text{Al}/^{24}\text{Mg}$  isochron diagram (Lee et al. 1976). This ratio is much higher than what is observed by  $\gamma$ -ray astronomy in the average interstellar medium gas ( $3 \times 10^{-6}$ ) (Diehl et al. 2006, 2010; Tang & Dauphas 2012). It is also high in comparison to other short-lived nuclides such as  $^{60}\text{Fe}$  ( $t_{1/2} = 2.6$  Myr), for which the  $^{60}\text{Fe}/^{56}\text{Fe}$  ratio in the early Solar System, of  $1 \times 10^{-8}$  (Tang & Dauphas 2012, 2015), is lower than the ratio in the interstellar medium gas, of  $3 \times 10^{-7}$  (Wang et al. 2007, Tang & Dauphas 2012). The reason for this high abundance of  $^{26}\text{Al}$  is uncertain, but the most likely scenario is that it came from the winds of one or several massive stars that shed some of their mass right before the Solar System formed (Gounelle & Meynet 2012, Tang & Dauphas 2012, Young 2014). The question of the homogeneity of short-lived nuclides has been posed ever since it was found that refractory inclusions that carry large isotopic anomalies (FUN inclusions and hibonite inclusions) have a very low abundance of  $^{26}\text{Al}/^{27}\text{Al}$  (Ireland 1990, Lee et al. 1979) compared to non-FUN refractory inclusions (**Figure 9**; see the caption for an extensive reference list).  $^{182}\text{Hf}$  dating indicates that FUN CAIs are not much younger than non-FUN CAIs (Holst et al. 2013), but the half-life of  $^{182}\text{Hf}$  ( $\sim 9$  Myr) is not well adapted to resolve small age differences among CAIs. Most likely, the lower abundance of  $^{26}\text{Al}$  in FUN CAIs and hibonite inclusions does not reflect a difference in formation age but rather the fact that FUN CAIs and hibonite grains captured the composition of the solar nebula before complete homogenization of  $^{26}\text{Al}$ . This explains why these objects often carry large isotopic anomalies. An important question that has not yet been completely settled is the question of the homogeneity (or lack thereof) of  $^{26}\text{Al}$  at a bulk planetary scale. This is important because  $^{26}\text{Al}$  was a potent heat

source in planetesimals (Lee et al. 1976, 1977; Grimm & McSween 1993; Dauphas & Chaussidon 2011) and Mars (Dauphas & Pourmand 2011), and the  $^{26}\text{Al}$ - $^{26}\text{Mg}$  decay system is very well suited to establish the chronology of early Solar System events provided that it was uniformly distributed (Nyquist et al. 2009, Dauphas & Chaussidon 2011, Davis & McKeegan 2014). A way to examine this is to compare various radiochronometers, in particular U-Pb dating, with  $^{26}\text{Al}$ - $^{26}\text{Mg}$  (Zinner & Göpel 2002). Much of the discussion has centered on the age of quenched angrites (early-formed rapidly quenched basaltic meteorites) relative to CAIs, which are both amenable to dating by U-Pb (CAIs: Amelin et al. 2010, Bouvier & Wadhwa 2010, Connelly et al. 2012; quenched angrites: Amelin 2008, Connelly et al. 2008, Larsen et al. 2011, Brennecka & Wadhwa 2012) and  $^{26}\text{Al}$ - $^{26}\text{Mg}$  (CAIs: Jacobsen et al. 2008; quenched angrites: Spivak-Birndorf et al. 2009, Schiller et al. 2010) dating techniques. Other dating techniques can also be compared with  $^{26}\text{Al}$ - $^{26}\text{Mg}$ , such as  $^{53}\text{Mn}$ - $^{53}\text{Cr}$  (Glavin et al. 2004, Sugiura et al. 2005),  $^{60}\text{Fe}$ - $^{60}\text{Ni}$  (Quitté et al. 2010; Tang & Dauphas 2012, 2015), or  $^{182}\text{Hf}$ - $^{182}\text{W}$  (Kleine et al. 2012). Overall, the jury is still out on whether the  $^{26}\text{Al}$ - $^{26}\text{Mg}$  dating technique is concordant with other techniques (Davis & McKeegan 2014). An issue with U-Pb dating of CAIs, at the level of precision required for comparison with  $^{26}\text{Al}$ , is that analytical artifacts may be introduced by the leaching procedure used to reduce the contribution of common lead (Pb that is not produced by in situ decay, i.e., incorporated in the CAI when it formed, introduced from the surrounding matrix on the parent body or during sample preparation, or terrestrial contamination).

Another approach to tackle this issue of the initial  $^{26}\text{Al}$  abundance is to examine the  $^{26}\text{Mg}/^{24}\text{Mg}$  ratio in bulk planetary objects after correction for mass fractionation by internal normalization using the  $^{25}\text{Mg}/^{24}\text{Mg}$  ratio. The rationale behind this approach is that if some regions of the Solar System formed with heterogeneous  $^{26}\text{Al}/^{27}\text{Al}$ , decay of  $^{26}\text{Al}$  into  $^{26}\text{Mg}$  will have created  $^{26}\text{Mg}^*$  isotope variations at a bulk planetary scale (Villeneuve et al. 2009, Larsen et al. 2011). At the time of CAI formation, the solar initial  $^{26}\text{Al}/^{26}\text{Mg}$  ratio was  $\sim 3.6 \times 10^{-5}$ , which means that if a nebular reservoir was entirely missing  $^{26}\text{Al}$ , it would display an anomaly of  $-0.036\%$  in  $\Delta^{26}\text{Mg}$  (assuming that the  $^{27}\text{Al}/^{26}\text{Mg}$  ratio was uniform). CAIs display variable Mg isotopic mass fractionation due to evaporation/condensation processes, and choosing the proper mass fractionation law (Section 2) is important to discuss small  $^{26}\text{Mg}^*$  variations (Davis et al. 2015). Larsen et al. (2011) measured at high precision the  $\Delta^{26}\text{Mg}$  isotopic composition of several Solar System materials and found variations that range between approximately  $-0.008\%$  and  $+0.005\%$  relative to the terrestrial composition. An isochron diagram for CAIs and amoeboid olivine aggregates gives a  $\Delta^{26}\text{Mg}$  value at a solar Al/Mg ratio of  $+0.022\%$  for the nebular reservoir characterized by a  $^{26}\text{Al}/^{27}\text{Al}$  of  $5 \times 10^{-5}$ . Larsen et al. (2011) interpreted those variations to reflect the heterogeneous distribution of  $^{26}\text{Al}$  at a bulk planetary scale, so that most achondrite groups would have incorporated very low amounts of  $^{26}\text{Al}$  (as low as  $1 \times 10^{-5}$ ), whereas chondrites would have incorporated intermediate values ( $1.6 \times 10^{-5}$  to  $2.8 \times 10^{-5}$ ). The suggestion that achondrites incorporated low amounts of  $^{26}\text{Al}$  is counterintuitive because one of the reasons why these meteorites were molten, whereas chondrites experienced only subsolidus metamorphism, could be that achondrites accreted early (before chondrites), so that there was more  $^{26}\text{Al}$  around to induce melting (Dauphas & Chaussidon 2011). Larsen et al. (2011) assumed that the variations in  $^{26}\text{Mg}$  at a bulk planetary scale are due to the heterogeneous distribution of  $^{26}\text{Al}$ . More likely, these variations are isotopic anomalies of nucleosynthetic origin (Wasserburg et al. 1977, 2012; Ireland et al. 1991; Liu et al. 2009) and are unrelated to variations in the abundance of  $^{26}\text{Al}$  at a megascopic scale. A strong line of evidence in support of this view is the fact that  $\Delta^{26}\text{Mg}$  anomalies correlate with  $\epsilon^{54}\text{Cr}$  anomalies (Larsen et al. 2011), which have a clear nucleosynthetic origin (Dauphas et al. 2010, Qin et al. 2011b). This illustrates how interpreting isotopic variations is fraught with difficulties when the isotopic variations can be ascribed to several processes that cannot be disentangled easily. The presumed

uniformity of  $^{26}\text{Al}$  at large planetary scale does not imply that  $^{26}\text{Al}$  was homogeneously distributed at finer scale, as evidence suggests that FUN inclusions and hibonite inclusions probably formed from a reservoir depleted in  $^{26}\text{Al}$ .

### 7.2. $^{53}\text{Mn}$ - $^{53}\text{Cr}$ ( $t_{1/2} = 3.7$ Myr) and $^{60}\text{Fe}$ - $^{60}\text{Ni}$ ( $t_{1/2} = 2.6$ Myr)

As discussed above, isotopic anomalies are present for chromium, but these anomalies affect predominantly the neutron-rich isotope,  $^{54}\text{Cr}$ . Furthermore, besides  $^{53}\text{Cr}$  and  $^{54}\text{Cr}$ , chromium possesses two additional isotopes ( $^{50}\text{Cr}$  and  $^{52}\text{Cr}$ ) that can be used for correcting mass-dependent fractionation by internal normalization, so in theory,  $^{53}\text{Cr}$  isotope measurements should be devoid of confounding nucleosynthetic anomalies. However, in mass spectrometry, double normalization is sometimes used to improve the precision of isotopic analyses. This is done when the ratios after correction for mass fractionation by internal normalization still correlate with the raw ratios, meaning that the mass fractionation law is more complex than that used for mass fractionation correction (see Section 2; often an exponential law in mass spectrometry) (Russell et al. 1978, Hart & Zindler 1989, Maréchal et al. 1999). Before it was recognized that there were anomalies at a bulk planetary scale for  $^{54}\text{Cr}$  (Shukolyukov & Lugmair 2006a, Trinquier et al. 2007, Qin et al. 2010a), Lugmair & Shukolyukov (1998) corrected their  $^{53}\text{Cr}$  data by using a second-order mass fractionation correction incorporating both  $^{50}\text{Cr}/^{52}\text{Cr}$  and  $^{54}\text{Cr}/^{52}\text{Cr}$  ratios. Different specimens from the same parent body have the same  $^{54}\text{Cr}$  anomaly, so the  $\epsilon^{53}\text{Cr}$  measurements are all shifted by the same value. When plotting a  $^{53}\text{Cr}/^{52}\text{Cr}$  versus  $^{55}\text{Mn}/^{52}\text{Cr}$  isochron, the slope will not be affected but the intercept will. Thus, when comparing materials from planetary objects, systematic offsets will be present in their apparent initial  $^{53}\text{Cr}/^{52}\text{Cr}$  ratios that are not real but rather are artifacts from the second-order correction. Lugmair & Shukolyukov (1998) had thus concluded that the  $^{53}\text{Mn}/^{55}\text{Mn}$  initial ratio was heterogeneous, possibly following a gradient with the heliocentric distance. Subsequent work (Shukolyukov & Lugmair 2006a, Trinquier et al. 2007, Qin et al. 2010a) showed that this was not real but an artifact from the data correction procedure and the fact that isotopic anomalies were present on  $^{54}\text{Cr}$ . Double normalization is seldom used except occasionally in ultrahigh-precision TIMS measurements (Caro et al. 2003, Touboul & Walker 2012). When applied, one must make sure that all the isotopes involved in the correction are clear of isotope anomalies, from either nucleosynthetic or nuclear field shift effects.

More recently, subtle effects were detected for Ni isotopes. Small effects were found in CB chondrites that are due to the presence of large natural isotopic fractionation associated with condensation that is not well accounted for by the exponential law (Tang & Dauphas 2012). Terrestrial standards used as references for isotopic ratios can also be affected by isotopic anomalies introduced during the industrial process used for producing high-purity materials. This was documented for Ni by Steele et al. (2011), who suggested that Ni purification by the Mond process (purification of Ni as volatile nickel tetracarbonyl) could have imparted isotope effects that are not fully accounted for by the exponential law. These anomalies have to be taken into account to infer the abundance of  $^{60}\text{Fe}$  in meteorites from  $^{60}\text{Ni}$  isotope measurements.

### 7.3. $^{146}\text{Sm}$ - $^{142}\text{Nd}$ ( $t_{1/2} = 68$ or 103 Myr)

For refractory lithophile elements, the assumption is usually that they are present in constant chondritic proportions in Solar System materials. At a bulk scale, one would therefore expect Earth's mantle to have chondritic Sm/Nd ratio, as well as chondritic  $^{142}\text{Nd}/^{144}\text{Nd}$  and

$^{143}\text{Nd}/^{144}\text{Nd}$  ratios, where  $^{142}\text{Nd}$  and  $^{143}\text{Nd}$  are produced in part by the decays of  $^{146}\text{Sm}$  ( $t_{1/2} = 68$  or 103 Myr) and  $^{147}\text{Sm}$  ( $t_{1/2} = 106$  Gyr). It is difficult to evaluate whether the  $^{143}\text{Nd}/^{144}\text{Nd}$  ratio is chondritic in the silicate Earth, because planetary differentiation processes and in particular continental crust extraction fractionated the Sm/Nd ratio, and decay of  $^{147}\text{Sm}$  created reservoirs with disparate  $^{143}\text{Nd}/^{144}\text{Nd}$  ratios. The  $^{142}\text{Nd}/^{144}\text{Nd}$  ratio is potentially more straightforward to interpret because any variation in  $^{142}\text{Nd}$  must have been caused by early Sm/Nd fractionation, while  $^{146}\text{Sm}$  was still alive. Boyet & Carlson (2005) measured the  $\epsilon^{142}\text{Nd}$  isotopic compositions of several chondrite groups and found that they had lower  $\epsilon^{142}\text{Nd}$  than terrestrial rocks available at Earth's surface. They interpreted those deficits as evidence that rocks available at Earth's surface are not representative of the silicate Earth. In their scenario, an early-enriched reservoir (a proto-crust) was formed with a low Sm/Nd (during partial melting, Nd is more incompatible than Sm, so it partitions preferentially into the melt) that developed a subchondritic  $\epsilon^{142}\text{Nd}$ , which was then recycled in the deep Earth, where it was sequestered ever after as a hidden reservoir (Brown et al. 2014). The mantle reservoir left behind (early-depleted reservoir, or EDR) has a suprachondritic Sm/Nd ratio and  $\epsilon^{142}\text{Nd}$ . In contrast, Caro and coworkers (Caro et al. 2008, Caro 2015) interpreted these results to reflect the fact that Earth as a whole may have nonchondritic isotopic composition, as a result of early crustal erosion by impacts. It was shown recently that Earth displays a Tm anomaly relative to CI chondrites and that this reflects nebular fractionation of the rare earth elements (Dauphas & Pourmand 2015, Barrat et al. 2016), so nebular processes could also fractionate refractory lithophile elements at a bulk planetary scale. A difficulty with the scenario of early removal of crustal material, either to space or to the deep Earth, is that overall, lanthanides have similar behaviors, so one may expect that there should be clear collateral effects in the compositions of other elements. In the original study of Boyet & Carlson (2005), no enstatite chondrite was measured. Subsequent work showed that different chondrite groups have different  $\epsilon^{142}\text{Nd}$  values, which cannot be explained by fractionation in the Sm/Nd ratio (Gannoun et al. 2011).

Bulk carbonaceous chondrites display negative anomalies in  $^{144}\text{Sm}$ , a  $p$ -process isotope (Andreasen & Sharma 2006, Gannoun et al. 2011).  $^{142}\text{Nd}$  is an  $s$ -process isotope with a small  $p$ -process contribution of  $\sim 4\%$  (Rauscher et al. 2013), but an additional complication when examining the isotopic anomalies of different elements is that during condensation in the presolar carrier of these anomalies, they can be chemically fractionated, and the slope of the line in a  $\epsilon^{142}\text{Nd}-\epsilon^{144}\text{Sm}$  diagram is influenced by the Sm/Nd ratio in the presolar carrier compared to the solar ratio (the curvature term in Equation 37; see Rauscher et al. 2013). Furthermore, given the observations made on  $^{144}\text{Sm}$ , it is conceivable that the short-lived  $p$ -nuclide  $^{146}\text{Sm}$  was heterogeneously distributed in the Solar System, which could have influenced  $^{142}\text{Nd}$  (Andreasen & Sharma 2006). Overall, carbonaceous chondrites display variations in the abundance of  $p$ -process isotopes, and they should not be used as a reference to estimate the bulk  $\epsilon^{142}\text{Nd}$  value of Earth.

An additional complication is the presence of isotopic anomalies corresponding to variable contributions of the  $s$ - and  $r$ -processes. Qin et al. (2011a) plotted all chondrite and basaltic eucrite data for  $\epsilon^{142}\text{Nd}$  versus  $\epsilon^{148}\text{Nd}$  and showed that they form an overall trend consistent with variations in the  $r$ - and  $s$ -processes. To estimate the starting bulk terrestrial  $\epsilon^{142}\text{Nd}$  value, one has to extrapolate the  $\epsilon^{142}\text{Nd}-\epsilon^{148}\text{Nd}$  correlation to  $\epsilon^{148}\text{Nd}$  values of zero. The  $\epsilon^{142}\text{Nd}-\epsilon^{148}\text{Nd}$  correlation is poorly defined (the error bars are large, and the slope is not well pronounced), so it is difficult to tell for sure whether measured terrestrial rocks are unlike any chondrite group after correction for isotopic anomalies. Recent high-precision Nd measurements of several chondrite groups seem to indicate that the variations in  $^{142}\text{Nd}$  among terrestrial and meteoritic samples are of



nucleosynthetic origin (Burkhardt et al. 2016). This is a perfect illustration of how nucleosynthetic anomalies can be troublemakers for geochronologic inferences.

#### 7.4. $^{182}\text{Hf}$ - $^{182}\text{W}$ ( $t_{1/2} = 9$ Myr)

The isotopic composition of W in meteorites can vary due to decay of  $^{182}\text{Hf}$ , but other issues complicate interpretation of W isotope variations. The first one is cosmogenic effects. This complication is prevalent in lunar rocks, where neutron capture on  $^{181}\text{Ta}$  and W isotopes can change the isotopic abundance of  $^{182}\text{W}$ . Strategies were devised to minimize and correct for these effects, including correlating  $\epsilon^{182}\text{W}$  with Ta/W ratios (Lee et al. 2002); measuring samples with low Ta/W ratio, such as metal (Touboul et al. 2015); and simultaneously analyzing other elements, such as Hf, that are sensitive to neutron-capture effects (Kruijer et al. 2015). Neutron-capture effects are also present in iron meteorites, and these effects tend to decrease the abundance of  $^{182}\text{W}$ , as this nuclide can capture neutrons to produce  $^{183}\text{W}$  but is not fed by any neutron-capture reaction. Again, strategies were devised to minimize and correct these effects, by focusing on samples with low exposure age and/or high shielding (Markowski et al. 2006, Scherstén et al. 2006, Qin et al. 2008b) or by measuring proxies of neutron capture in iron meteorites, such as Pt or Os (Wittig et al. 2013, Kruijer et al. 2014b, Qin et al. 2015). For W in bulk meteorites, cosmogenic effects are a much bigger issue than nucleosynthetic effects, but Qin et al. (2008a) reported the presence of small  $^{184}\text{W}$  isotopic anomalies in IVB iron meteorites. They calculated the expected collateral effect on  $^{182}\text{W}$  and concluded that this effect would most likely be small. Isotopic anomalies are a more serious concern in refractory inclusions, as their  $\epsilon^{182}\text{W}$  initial value is used as a reference to calculate  $^{182}\text{Hf}$ - $^{182}\text{W}$  ages of various planetary materials, in particular iron meteorites. CAIs display isotopic anomalies for  $\epsilon^{183}\text{W}$  (after internal normalization using  $^{186}\text{W}/^{184}\text{W}$ ) (Burkhardt et al. 2008, 2012a; Kruijer et al. 2014a). To correct the  $\epsilon^{182}\text{W}$  value of CAIs for the presence of nucleosynthetic effects, one has to know how  $\epsilon^{182}\text{W}$  and  $\epsilon^{183}\text{W}$  nucleosynthetic anomalies correlate. Because of uncertainties in *s*-process calculations, modeling results provide little guidance to constrain this relationship (Qin et al. 2008a). As discussed in Section 5, leachates can reveal isotopic heterogeneities that are not widely expressed at a bulk sample scale. Burkhardt et al. (2012a) measured the W isotopic composition of leachates from the Murchison meteorite and found W isotopic anomalies that allowed them to better constrain the nature of the correlation between  $\epsilon^{182}\text{W}$  and  $\epsilon^{183}\text{W}$  isotopic anomalies and refine estimates of the initial Solar System values of  $\epsilon^{182}\text{W}$  and  $^{182}\text{Hf}/^{180}\text{Hf}$ . They thus revised the initial  $\epsilon^{182}\text{W}$  of the Solar System from  $-3.28 \pm 0.12$  to  $-3.51 \pm 0.10$  parts per  $10^4$ . This solved a geochronologic conundrum, as previous data had shown that iron meteorites had a lower  $\epsilon^{182}\text{W}$  value than the supposed CAI initial value (Burkhardt et al. 2008), which taken at face value would have meant that iron meteorites formed before CAIs, a conclusion that seemed implausible. Taking into account isotopic anomalies in CAIs, Burkhardt et al. (2012a) showed that the CAI initial  $\epsilon^{182}\text{W}$  value was actually smaller than or similar to that of iron meteorites, consistent with their formation in the first 1–2 Myr of the formation of the Solar System. Subsequent work by Kruijer et al. (2014a) confirmed this conclusion.

Because tungsten is a high-atomic number element, there should perhaps be concern that the nuclear field shift effect (Section 4) could lead to isotope fractionation that is not correctly normalized by a mass-dependent fractionation law. Confounding effects from the nuclear volume component of the field shift effect are likely to be subtle, however, because the nuclear radii of the relevant tungsten isotopes correlate closely with their masses (e.g., Fricke & Heilig 2004). Reconnaissance field shift effect calculations (E.A. Schauble, unpublished work) suggest that anomalies of several parts per million in  $^{182}\text{W}/^{184}\text{W}$ , and hundreds of parts per billion in  $^{183}\text{W}/^{184}\text{W}$ , may

be possible if W(0)- and W(IV)-bearing phases (e.g., tungsten-iron alloy and WS<sub>2</sub>-tungstenite) equilibrate and one of the fractionated phases is preferentially sampled.

## 8. CONCLUSION

As analytical capabilities improve and isotopic ratios can be measured with better precision, the zoo of isotopic anomalies is rapidly expanding, which provides new insights into natural processes that are not available otherwise:

1. Although they cannot be strictly called isotopic anomalies, subtle variations in mass fractionation laws can now be investigated to decipher the mechanisms (e.g., kinetic versus equilibrium) involved in establishing isotopic variations, thus reducing the range of possibilities.
2. Bona fide isotopic anomalies in O and S in meteoritic and terrestrial samples provide considerable information on exotic physicochemical processes. Planetary materials are depleted in <sup>16</sup>O relative to the Sun, possibly reflecting gas-solid condensation chemistry or CO self-shielding in the solar nebula or in a molecular cloud environment. Mass-independent S isotope variation in sediments provides the most definitive record of Earth's atmosphere oxygenation through time.
3. Isotope fractionations caused by the magnetic effect and nuclear field shift affect the isotopic composition of mercury and other heavy elements in terrestrial surface environments. For the elements U and Tl, nuclear field shift is thought to be the main driving force to the stable isotope variations documented in nature. However, because those elements possess only two long-lived isotopes, it is necessary to combine theoretical modeling with measurements to confidently assign mass-dependent and mass-independent effects. Mercury, with seven stable isotopes, shows both large, probably magnetic mass-independent isotope signatures and subtler nuclear field shift effects. Both signatures are clearly manifested as odd-even mass modulations on mass-dependent fractionation.
4. Nucleosynthetic anomalies affect planetary materials at all scales, from nanometer-sized presolar grains to terrestrial planets. For elements in the iron-mass region, those anomalies affect predominantly the neutron-rich isotopes (<sup>48</sup>Ca, <sup>50</sup>Ti, <sup>54</sup>Cr, <sup>64</sup>Ni) and have a supernova origin. For heavier elements produced by the *s*-, *r*-, and *p*-processes, a variety of isotopic patterns are found that can be disentangled. Several processes seem to control the patterns in refractory inclusions, but some patterns correspond to clear variations in the *r*-process. Isotopic anomalies in acid leachates and bulk meteorites primarily involve variations in the *s*-process.
5. Isotopic anomalies in bulk planetary materials are like indelible tags that can be used to trace planetary genetics and ascertain meteorite classification. As an example, the Moon has <sup>16</sup>O, <sup>48</sup>Ca, <sup>50</sup>Ti, and <sup>54</sup>Cr isotopic compositions that are indistinguishable from those of Earth. This is best explained in a giant-impact model of lunar formation if the impactor had the same isotopic composition as the proto-Earth because material that made Earth did not change with time and came from a region of the disk that had uniform isotopic composition (the IDUR). Enstatite chondrites sample the same isotopic reservoir as Earth and Theia. The contrast in composition between carbonaceous and noncarbonaceous chondrites is best explained if these bodies were formed from nebular reservoirs that were separated in time or, more likely, space and never exchanged.
6. Isotopic anomalies can be a curse, as they can confound interpretations of radiogenic isotope systems commonly used in geochronology, such as <sup>26</sup>Al-<sup>26</sup>Mg or <sup>146</sup>Sm-<sup>142</sup>Nd.


The fields of isotope geochemistry and cosmochemistry have seen a tremendous growth in studies of mass fractionation laws and isotopic anomalies. With no end in sight, those studies are changing the paradigm, such that isotopic anomalies are the new normal.

## DISCLOSURE STATEMENT

The authors are not aware of any affiliations, memberships, funding, or financial holdings that might be perceived as affecting the objectivity of this review.

## ACKNOWLEDGMENTS

This paper is dedicated to the memories of Ian Hutcheon and Ernst Zinner, whose studies of high-temperature dust condensates of presolar and solar origins influenced all aspects of isotope cosmochemistry. Christoph Burkhardt is thanked for sharing a preliminary version of **Supplemental Table 1** and for discussions. This work was supported by NASA (LARS, grant NNX14AK09G to N.D.) and NSF (Petrology and Geochemistry, grant EAR1444951 to N.D.; CSEDI, grant EAR1502591 to N.D.; Geobiology and Low-Temperature Geochemistry, grant EAR1530306 to E.A.S.). We are grateful to A.M. Davis, A.J. Campbell, F.J. Ciesla, F. Nimmo, T. Rauscher, B.S. Meyer, and R. Gallino for discussions on isotopic anomalies, stellar nucleosynthesis, and planetary accretion.

 Supplemental Material

## LITERATURE CITED

- Abe M, Suzuki T, Fujii Y, Hada M. 2008a. An *ab initio* study based on a finite nucleus model for isotope fractionation in the U(III)-U(IV) exchange reaction system. *J. Chem. Phys.* 128:144309
- Abe M, Suzuki T, Fujii Y, Hada M, Hirao K. 2008b. An *ab initio* molecular orbital study of the nuclear volume effects in uranium isotope fractionations. *J. Chem. Phys.* 129:164309
- Abe M, Suzuki T, Fujii Y, Hada M, Hirao K. 2010. Ligand effect on uranium isotope fractionations caused by nuclear volume effects: an *ab initio* relativistic molecular orbital study. *J. Chem. Phys.* 133:044309
- Akram W, Schönbachler M, Bisterzo S, Gallino R. 2015. Zirconium isotope evidence for the heterogeneous distribution of s-process materials in the solar system. *Geochim. Cosmochim. Acta* 165:484–500
- Akram W, Schönbachler M, Sprung P, Vogel N. 2013. Zirconium-hafnium isotope evidence from meteorites for the decoupled synthesis of light and heavy neutron-rich nuclei. *Astrophys. J.* 777:169
- Amari S, Anders E, Virag A, Zinner E. 1990. Interstellar graphite in meteorites. *Nature* 345:238–40
- Amari S, Lewis RS, Anders E. 1994. Interstellar grains in meteorites: I. Isolation of SiC, graphite and diamond; size distributions of SiC and graphite. *Geochim. Cosmochim. Acta* 58:459–70
- Amari S, Zinner E, Gallino R. 2014. Presolar graphite from the Murchison meteorite: an isotopic study. *Geochim. Cosmochim. Acta* 133:479–522
- Amelin Y. 2008. U-Pb ages of angrites. *Geochim. Cosmochim. Acta* 72:221–32
- Amelin Y, Kaltenbach A, Iizuka T, Stirling CH, Ireland TR, et al. 2010. U–Pb chronology of the Solar System's oldest solids with variable  $^{238}\text{U}/^{235}\text{U}$ . *Earth Planet. Sci. Lett.* 300:343–50
- Anders E, Grevesse N. 1989. Abundances of the elements: meteoritic and solar. *Geochim. Cosmochim. Acta* 53:197–214
- Anders E, Zinner E. 1993. Interstellar grains in primitive meteorites: diamond, silicon carbide, and graphite. *Meteoritics* 28:490–514
- Andersen MB, Elliott T, Freymuth H, Sims KWW, Niu Y, Kelley KA. 2015. The terrestrial uranium cycle. *Nature* 517:356–59
- Andreasen R, Sharma M. 2006. Solar nebula heterogeneity in p-process samarium and neodymium isotopes. *Science* 314:806–9
- Andreasen R, Sharma M. 2007. Mixing and homogenization in the early solar system: clues from Sr, Ba, Nd, and Sm isotopes in meteorites. *Astrophys. J.* 665:874
- Angeli I. 2004. A consistent set of nuclear rms charge radii: properties of the radius surface  $R(N,Z)$ . *At. Data Nucl. Data Tables* 87:185–296
- Angeli I, Marinova KP. 2013. Table of experimental nuclear ground state charge radii: an update. *At. Data Nucl. Data Tables* 99:69–95

- Angert A, Rachmilevitch S, Barkan E, Luz B. 2003. Effects of photorespiration, the cytochrome pathway, and the alternative pathway on the triple isotopic composition of atmospheric O<sub>2</sub>. *Glob. Biogeochem. Cycles* 17:1030
- Arlandini C, Käppeler F, Wisshak K, Gallino R, Lugaro M, et al. 1999. Neutron capture in low-mass asymptotic giant branch stars: cross sections and abundance signatures. *Astrophys. J.* 525:886
- Armstrong J, Hutcheon I, Wasserburg G. 1984. Disturbed Mg isotopic systematics in Allende CAI. *Lunar Planet. Sci. Conf. Abstr.* 15:15–16
- Armytage R, Georg R, Williams H, Halliday A. 2012. Silicon isotopes in lunar rocks: implications for the Moon's formation and the early history of the Earth. *Geochim. Cosmochim. Acta* 77:504–14
- Assonov SS, Brenninkmeijer CAM. 2005. Reporting small  $\Delta^{17}\text{O}$  values: existing definitions and concepts. *Rapid Commun. Mass Spectrom.* 19:627–36
- Audi G, Wapstra AH, Thibault C. 2003. The AME2003 atomic mass evaluation. *Nucl. Phys. A* 729:337–676
- Bally J, Langer WD. 1982. Isotope-selective photodestruction of carbon monoxide. *Astrophys. J.* 255:143–48
- Bao H, Lyons JR, Zhou C. 2008. Triple oxygen isotope evidence for elevated CO<sub>2</sub> levels after a Neoproterozoic glaciation. *Nature* 453:504–6
- Bao Z, Beer H, Käppeler F, Voss F, Wisshak K, Rauscher T. 2000. Neutron cross sections for nucleosynthesis studies. *At. Data Nucl. Data Tables* 76:70–154
- Barkan E, Luz B. 2005. High precision measurements of  $^{17}\text{O}/^{16}\text{O}$  and  $^{18}\text{O}/^{16}\text{O}$  ratios in H<sub>2</sub>O. *Rapid Commun. Mass Spectrom.* 19:3737–42
- Barkan E, Luz B. 2012. High precision measurements of  $^{17}\text{O}/^{16}\text{O}$  and  $^{18}\text{O}/^{16}\text{O}$  ratios in CO<sub>2</sub>. *Rapid Commun. Mass Spectrom.* 26:2733–38
- Baroni M, Thiemens MH, Delmas RH, Savarino J. 2007. Mass-independent sulfur isotopic compositions in stratospheric volcanic eruptions. *Science* 315:84–87
- Barrat JA, Dauphas N, Gillet P, Bollinger C, Etoubleau J, et al. 2016. Evidence from Tm anomalies for non-CI refractory lithophile element proportions in terrestrial planets and achondrites. *Geochim. Cosmochim. Acta* 176:1–17
- Beckett JR. 1986. *The origin of calcium-, aluminum-rich inclusions from carbonaceous chondrites: an experimental study*. PhD Diss., Dep. Geophys. Sci., Univ. Chicago
- Bergquist BA, Blum JD. 2007. Mass-dependent and -independent fractionation of Hg isotopes by photoreduction in aquatic systems. *Science* 318:417–20
- Bernatowicz T, Fraundorf G, Ming T, Anders E, Wopenka B, et al. 1987. Evidence for interstellar SiC in the Murray carbonaceous meteorite. *Nature* 330:728–30
- Bigeleisen J. 1962. Correlation of tritium and deuterium isotope effects. In *Tritium in the Physical and Biological Sciences*, pp. 161–68. Vienna: Int. At. Energy Agency
- Bigeleisen J. 1996a. Nuclear size and shape effects in chemical reactions. Isotope chemistry of the heavy elements. *J. Am. Chem. Soc.* 118:3676–80
- Bigeleisen J. 1996b. Temperature dependence of the isotopes chemistry of heavy elements. *PNAS* 93:9393–96
- Bigeleisen J, Mayer MG. 1947. Calculation of equilibrium constants for isotopic exchange reactions. *J. Chem. Phys.* 15:261–67
- Bindeman IN, Eiler JM, Wing BA, Farquhar J. 2007. Rare sulfur and triple oxygen isotope geochemistry of volcanogenic sulfate aerosols. *Geochim. Cosmochim. Acta* 71:2326–43
- Birck JL. 2004. An overview of isotopic anomalies in extraterrestrial materials and their nucleosynthetic heritage. *Rev. Mineral. Geochem.* 55:25–64
- Birck JL, Allègre CJ. 1984. Anomalous isotopic composition of chromium in Allende inclusions. *Meteoritics* 19:190–92
- Birck JL, Allègre CJ. 1988. Manganese-chromium isotope systematics and the development of the early Solar System. *Nature* 331:579–84
- Birck JL, Lugmair GW. 1988. Nickel and chromium isotopes in Allende inclusions. *Earth Planet. Sci. Lett.* 90:131–43
- Black D, Pepin R. 1969. Trapped neon in meteorites: II. *Earth Planet. Sci. Lett.* 6:395–405
- Blöchl PE. 1994. Projector augmented-wave method. *Phys. Rev. B* 50:17953–79
- Blum JD, Sherman LS, Johnson MW. 2014. Mercury isotopes in Earth and environmental sciences. *Annu. Rev. Earth Planet. Sci.* 42:249–69

- Bogdanovski O, Papanastassiou D, Wasserburg G. 2002. Cr isotopes in Allende Ca-Al-rich inclusions. *Lunar Planet. Sci. Conf. Abstr.* 23:1802
- Bopp CJ IV, Lundstrom CC, Johnson TM, Glessner JJG. 2009. Variations in  $^{238}\text{U}/^{235}\text{U}$  in uranium ore deposits: isotopic signatures of the U reduction process? *Geology* 37:611–14
- Bopp CJ IV, Lundstrom CC, Johnson TM, Sanford RA, Long PE, Williams KH. 2010. Uranium  $^{238}\text{U}/^{235}\text{U}$  isotope ratios as indicators of reduction: results from an in situ biostimulation experiment at Rifle, Colorado, U.S.A. *Environ. Sci. Technol.* 44:5927–33
- Boss AP. 2004. Evolution of the solar nebula. VI. Mixing and transport of isotopic heterogeneity. *Astrophys. J.* 616:1265
- Bouvier A, Wadhwa M. 2010. The age of the Solar System redefined by the oldest Pb-Pb age of a meteoritic inclusion. *Nat. Geosci.* 3:637–41
- Boyet M, Carlson R. 2005.  $^{142}\text{Nd}$  evidence for early (>4.53 Ga) global differentiation of the silicate Earth. *Science* 309:576–81
- Boyet M, Gannoun A. 2013. Nucleosynthetic Nd isotope anomalies in primitive enstatite chondrites. *Geochim. Cosmochim. Acta* 121:652–66
- Brandon A, Humayun M, Puchtel I, Leya I, Zolensky M. 2005. Osmium isotope evidence for an *s*-process carrier in primitive chondrites. *Science* 309:1233–36
- Brennecke GA, Borg LE, Hutcheon ID, Sharp MA, Anbar AD. 2010a. Natural variations in uranium isotope ratios of uranium ore concentrates: understanding the  $^{238}\text{U}/^{235}\text{U}$  fractionation mechanism. *Earth Planet. Sci. Lett.* 291:228–33
- Brennecke GA, Borg LE, Wadhwa M. 2013. Evidence for supernova injection into the solar nebula and the decoupling of *r*-process nucleosynthesis. *PNAS* 110:17241–46
- Brennecke GA, Wadhwa M. 2012. Uranium isotope compositions of the basaltic angrite meteorites and the chronological implications for the early Solar System. *PNAS* 109:9299–303
- Brennecke GA, Wasylenki LE, Bargar JR, Weyer S, Anbar AD. 2011. Uranium isotope fractionation during adsorption to Mn-oxyhydroxides. *Environ. Sci. Technol.* 45:1370–75
- Brennecke GA, Weyer S, Wadhwa M, Janney PE, Zipfel J, Anbar AD. 2010b.  $^{238}\text{U}/^{235}\text{U}$  variations in meteorites: extant  $^{247}\text{Cm}$  and implications for Pb-Pb dating. *Science* 327:449–51
- Brigham CA. 1990. *Isotopic heterogeneity in calcium-aluminum-rich meteoritic inclusions*. PhD Diss., Div. Geol. Planet. Sci., Calif. Inst. Technol.
- Bron J, Chang CF, Wolfsberg M. 1973. Isotopic partition function ratios involving  $\text{H}_2$ ,  $\text{H}_2\text{O}$ ,  $\text{H}_2\text{S}$ ,  $\text{H}_2\text{Se}$  and  $\text{NH}_3$ . *Z. Naturforsch. A* 28:129–36
- Brown SM, Elkins-Tanton LT, Walker RJ. 2014. Effects of magma ocean crystallization and overturn on the development of  $^{142}\text{Nd}$  and  $^{182}\text{W}$  isotopic heterogeneities in the primordial mantle. *Earth Planet. Sci. Lett.* 408:319–30
- Buchachenko AL. 1995. Magnetic isotope effect. *Theor. Exp. Chem.* 31:118–26
- Buchachenko AL. 2013. Mass-independent isotope effects. *J. Phys. Chem. B* 117:2231–38
- Burbidge EM, Burbidge GR, Fowler WA, Hoyle F. 1957. Synthesis of the elements in stars. *Rev. Mod. Phys.* 29:547
- Burkhardt C, Borg LE, Brennecke GA, Shollenberger QR, Dauphas N, Kleine T. 2016. A nucleosynthetic origin of the Earth's anomalous  $^{142}\text{Nd}$  composition. *Nature*. In press
- Burkhardt C, Kleine T, Bourdon B, Palme H, Zipfel J, et al. 2008. Hf-W mineral isochron for Ca,Al-rich inclusions: age of the solar system and the timing of core formation in planetesimals. *Geochim. Cosmochim. Acta* 72:6177–97
- Burkhardt C, Kleine T, Dauphas N, Wieler R. 2012a. Nucleosynthetic tungsten isotope anomalies in acid leachates of the Murchison chondrite: implications for hafnium-tungsten chronometry. *Astrophys. J. Lett.* 753:L6
- Burkhardt C, Kleine T, Dauphas N, Wieler R. 2012b. Origin of isotopic heterogeneity in the solar nebula by thermal processing and mixing of nebular dust. *Earth Planet. Sci. Lett.* 357:298–307
- Burkhardt C, Kleine T, Oberli F, Pack A, Bourdon B, Wieler R. 2011. Molybdenum isotope anomalies in meteorites: constraints on solar nebula evolution and origin of the Earth. *Earth Planet. Sci. Lett.* 312:390–400

- Burkhardt C, Schönbacher M. 2015. Intrinsic W nucleosynthetic isotope variations in carbonaceous chondrites: implications for W nucleosynthesis and nebular vs. parent body processing of presolar materials. *Geochim. Cosmochim. Acta* 165:361–75
- Cameron AGW. 1957. *Stellar Evolution, Nuclear Astrophysics, and Nucleogenesis*. Chalk River, Can.: At. Energy Can.
- Cameron AGW, Ward WR. 1976. The origin of the Moon. *Lunar Planet. Sci. Conf. Abstr.* 7:120–22
- Canup RM. 2012. Forming a Moon with an Earth-like composition via a giant impact. *Science* 338:1052–55
- Canup RM. 2014. Lunar-forming impacts: processes and alternatives. *Philos. Trans. R. Soc. A* 372:20130175
- Canup RM, Asphaug E. 2001. Origin of the Moon in a giant impact near the end of the Earth's formation. *Nature* 412:708–12
- Canup RM, Barr AC, Crawford DA. 2013. Lunar-forming impacts: high-resolution SPH and AMR-CTH simulations. *Icarus* 222:200–19
- Cao X, Liu Y. 2011. Equilibrium mass-dependent fractionation relationships for triple oxygen isotopes. *Geochim. Cosmochim. Acta* 75:7435–45
- Carlson RW, Boyet M, Horan M. 2007. Chondrite barium, neodymium, and samarium isotopic heterogeneity and early earth differentiation. *Science* 316:1175–78
- Caro G. 2015. Chemical geodynamics in a non-chondritic Earth. In *The Earth's Heterogeneous Mantle: A Geophysical, Geodynamical, and Geochemical Perspective*, ed. A Khan, F Deschamps, pp. 329–66. Cham, Switz.: Springer
- Caro G, Bourdon B, Birck JL, Moorbath S. 2003.  $^{146}\text{Sm}$ - $^{142}\text{Nd}$  evidence from Isua metamorphosed sediments for early differentiation of the Earth's mantle. *Nature* 423:428–32
- Caro G, Bourdon B, Halliday AN, Quitté G. 2008. Super-chondritic Sm/Nd ratios in Mars, the Earth and the Moon. *Nature* 452:336–39
- Chabot N, Haack H. 2006. Evolution of asteroidal cores. In *Meteorites and the Early Solar System II*, ed. DS Lauretta, HY McSween Jr., pp. 747–71. Tucson: Univ. Ariz. Press
- Chakraborty S, Davis RD, Ahmed M, Jackson TL, Thiemens MH. 2012. Oxygen isotope fractionation in the vacuum ultraviolet photodissociation of carbon monoxide: wavelength, pressure, and temperature dependency. *J. Chem. Phys.* 137:024309
- Chakraborty S, Yanchulova P, Thiemens MH. 2013. Mass independent oxygen isotopic partitioning during gas-phase  $\text{SiO}_2$  formation. *Science* 342:463–66
- Chambers JE, Wetherill GW. 1998. Making the terrestrial planets: N-body integrations of planetary embryos in three dimensions. *Icarus* 136:304–27
- Chen HW, Chen JC, Lee T, Shen JJ. 2010. Calcium isotopic anomalies in the Allende CAIs and the angrite Angra dos Reis. *Lunar Planet. Sci. Conf. Abstr.* 41:2088
- Chen HW, Lee T, Lee DC, Shen JJ, Chen JC. 2011.  $^{48}\text{Ca}$  heterogeneity in differentiated meteorites. *Astrophys. J. Lett.* 743:L23
- Chen J, Papanastassiou D, Wasserburg G. 2010. Ruthenium endemic isotope effects in chondrites and differentiated meteorites. *Geochim. Cosmochim. Acta* 74:3851–62
- Choi BG, McKeegan KD, Krot AN, Wasson JT. 1998. Extreme oxygen-isotope compositions in magnetite from unequilibrated ordinary chondrites. *Nature* 392:577–79
- Chou CL. 1978. Fractionation of siderophile elements in the Earth's upper mantle. *Lunar Planet. Sci. Conf. Abstr.* 9:219–30
- Cioslowski J. 1989. A new population analysis based on atomic polar tensors. *J. Am. Chem. Soc.* 111:8333–36
- Clayton DD. 1988. Nuclear cosmochronology within analytic models of the chemical evolution of the solar neighbourhood. *MNRAS* 234:1–36
- Clayton DD, Nittler LR. 2004. Astrophysics with presolar stardust. *Annu. Rev. Astron. Astrophys.* 42:38–78
- Clayton RN. 1978. Isotopic anomalies in the early solar system. *Annu. Rev. Nucl. Part. Sci.* 28:501–22
- Clayton RN. 1993. Oxygen isotopes in meteorites. *Annu. Rev. Earth Planet. Sci.* 21:115–49
- Clayton RN. 2002. Self-shielding in the solar nebula. *Nature* 415:860–61
- Clayton RN. 2003. Oxygen isotopes in meteorites. In *Treatise on Geochemistry*, Vol. 1: *Meteorites, Comets, and Planets*, ed. AM Davis, pp. 129–42. Oxford, UK: Elsevier-Pergamon. 1st ed.
- Clayton RN, Grossman L, Mayeda TK. 1973. A component of primitive nuclear composition in carbonaceous meteorites. *Science* 182:485–88

- Clayton RN, Mayeda T. 1975. Genetic relations between the Moon and meteorites. *Lunar Sci. Conf. Abstr.* 6:1761–69
- Clayton RN, Onuma N, Mayeda TK. 1976. A classification of meteorites based on oxygen isotopes. *Earth Planet. Sci. Lett.* 30:10–18
- Coggon RM, Rehkämper M, Atteck C, Teagle DAH, Alt JC, Cooper MJ. 2014. Controls on thallium uptake during hydrothermal alteration of the upper ocean crust. *Geochim. Cosmochim. Acta* 144:25–42
- Connelly JN, Bizzarro M, Krot AN, Nordlund Å, Wielandt D, Ivanova MA. 2012. The absolute chronology and thermal processing of solids in the solar protoplanetary disk. *Science* 338:651–55
- Connelly JN, Bizzarro M, Thrane K, Baker J. 2008. The Pb-Pb age of angrite Sah99555 revisited. *Geochim. Cosmochim. Acta* 72:4813–24
- Craig H, Horibe Y, Sowers T. 1988. Gravitational separation of gases and isotopes in polar ice caps. *Science* 242:1675–78
- Croat TK, Bernatowicz TJ, Daulton TL. 2014. Presolar graphitic carbon spherules: rocks from stars. *Elements* 10:441–46
- Ćuk M, Stewart ST. 2012. Making the Moon from a fast-spinning Earth: a giant impact followed by resonant despinning. *Science* 338:1047–52
- Daulton T, Bernatowicz T, Lewis R, Messenger S, Stadermann F, Amari S. 2003. Polytype distribution of circumstellar silicon carbide: microstructural characterization by transmission electron microscopy. *Geochim. Cosmochim. Acta* 67:4743–67
- Dauphas N, Burkhardt C, Warren PH, Fang-Zhen T. 2014a. Geochemical arguments for an Earth-like Moon-forming impactor. *Philos. Trans. R. Soc. A* 372:20130244
- Dauphas N, Chaussidon M. 2011. A perspective from extinct radionuclides on a young stellar object: the Sun and its accretion disk. *Annu. Rev. Earth Planet. Sci.* 39:351–86
- Dauphas N, Chen JH, Papanastassiou DA. 2015a. Testing Earth-Moon isotopic homogenization with calcium-48. *Lunar Planet. Sci. Conf. Abstr.* 46:2436
- Dauphas N, Chen JH, Zhang J, Papanastassiou DA, Davis AM, Travaglio C. 2014b. Calcium-48 isotopic anomalies in bulk chondrites and achondrites: evidence for a uniform isotopic reservoir in the inner protoplanetary disk. *Earth Planet. Sci. Lett.* 407:96–108
- Dauphas N, Davis AM, Marty B, Reisberg L. 2004. The cosmic molybdenum-ruthenium isotope correlation. *Earth Planet. Sci. Lett.* 226:465–75
- Dauphas N, Marty B. 2002. Inference on the nature and mass of Earth's late veneer from noble metals and gases. *J. Geophys. Res.* 197(E12):5129
- Dauphas N, Marty B, Reisberg L. 2002a. Inference on terrestrial genesis from molybdenum isotope systematics. *Geophys. Res. Lett.* 29:1084
- Dauphas N, Marty B, Reisberg L. 2002b. Molybdenum evidence for inherited planetary scale isotope heterogeneity of the protosolar nebula. *Astrophys. J.* 565:640
- Dauphas N, Marty B, Reisberg L. 2002c. Molybdenum nucleosynthetic dichotomy revealed in primitive meteorites. *Astrophys. J.* 569:L139–42
- Dauphas N, Poitrasson F, Burkhardt C, Kobayashi H, Kurosawa K. 2015b. Planetary and meteoritic Mg/Si and  $\delta^{30}\text{Si}$  variations inherited from solar nebula chemistry. *Earth Planet. Sci. Lett.* 427:236–48
- Dauphas N, Pourmand A. 2011. Hf-W-Th evidence for rapid growth of Mars and its status as a planetary embryo. *Nature* 473:489–92
- Dauphas N, Pourmand A. 2015. Thulium anomalies and rare earth element patterns in meteorites and Earth: nebular fractionation and the nugget effect. *Geochim. Cosmochim. Acta* 163:234–61
- Dauphas N, Remusat L, Chen JH, Roskosz M, Papanastassiou DA, et al. 2010. Neutron-rich chromium isotope anomalies in supernova nanoparticles. *Astrophys. J.* 720:1577–91
- Davis AM. 2011. Stardust in meteorites. *PNAS* 108:19142–46
- Davis AM, McKeegan KD. 2014. Short-lived radionuclides and early solar system chronology. In *Treatise on Geochemistry*, Vol. 1: *Meteorites and Cosmochemical Processes*, ed. AM Davis, pp. 361–95. Oxford, UK: Elsevier-Pergamon. 2nd ed.
- Davis AM, Richter FM, Mendybaev RA, Janney PE, Wadhwa M, McKeegan KD. 2015. Isotopic mass fractionation laws for magnesium and their effects on  $^{26}\text{Al}$ - $^{26}\text{Mg}$  systematics in solar system materials. *Geochim. Cosmochim. Acta* 158:245–61

- Deines P. 2003. A note on intra-elemental isotope effects and the interpretation of non-mass-dependent isotope variations. *Chem. Geol.* 199:179–82
- Diehl R, Halloin H, Kretschmer K, Lichti GG, Schonfelder V, et al. 2006. Radioactive  $^{26}\text{Al}$  from massive stars in the Galaxy. *Nature* 439:45–47
- Diehl R, Lang MG, Martin P, Ohlendorf H, Preibisch T, et al. 2010. Radioactive  $^{26}\text{Al}$  from the Scorpius-Centaurus association. *Astron. Astrophys.* 522:A51
- Douglas M, Kroll NM. 1974. Quantum electrodynamical corrections to the fine structures of helium. *Ann. Phys.* 82:89–155
- Draine B. 2009. Interstellar dust models and evolutionary implications. *Astron. Soc. Pac. Conf. Ser.* 414:453–72
- Drake MJ. 2001. The eucrite/Vesta story. *Meteorit. Planet. Sci.* 36:501–13
- Eiler JM, Bergquist B, Bourg I, Cartigny P, Farquhar J, et al. 2014. Frontiers of stable isotope geoscience. *Chem. Geol.* 372:119–43
- Esat T, Papanastassiou D, Wasserburg G. 1979. The trials and tribulations of  $^{26}\text{Al}$ : evidence for disturbed systems. *Lunar Planet. Sci. Conf. Abstr.* 10:361–63
- Estrade N, Carignan J, Sonke JE, Donard OFX. 2009. Mercury isotope fractionation during liquid-vapor evaporation experiments. *Geochim. Cosmochim. Acta* 73:2693–711
- Fahey A, Goswami J, McKeegan K, Zinner E. 1987a.  $^{16}\text{O}$  excesses in Murchison and Murray hibonites: a case against a late supernova injection origin of isotopic anomalies in O, Mg, Ca, and Ti. *Astrophys. J.* 323:L91–95
- Fahey A, Goswami J, McKeegan K, Zinner E. 1987b.  $^{26}\text{Al}$ ,  $^{244}\text{Pu}$ ,  $^{50}\text{Ti}$ , REE, and trace element abundances in hibonite grains from CM and CV meteorites. *Geochim. Cosmochim. Acta* 51:329–50
- Farquhar J, Bao H, Thiemens M. 2000. Atmospheric influence of Earth's earliest sulfur cycle. *Science* 289:756–58
- Farquhar J, Johnston DT, Wing BA, Habicht KS, Canfield DE, et al. 2003. Multiple sulphur isotopic interpretations of biosynthetic pathways: implications for biological signatures in the sulphur isotope record. *Geobiology* 1:27–36
- Farquhar J, Savarino J, Airieau S, Thiemens MH. 2001. Observation of wavelength-sensitive mass-independent sulfur isotope effects during  $\text{SO}_2$  photolysis: implications for the early atmosphere. *J. Geophys. Res.* 106(E12):32829–39
- Farquhar J, Wing BA. 2003. Multiple sulfur isotopes and the evolution of the atmosphere. *Earth Planet. Sci. Lett.* 213:1–13
- Fischer-Gödde M, Burkhardt C, Kruijer TS, Kleine T. 2015. Ru isotope heterogeneity in the solar protoplanetary disk. *Geochim. Cosmochim. Acta* 168:151–71
- Fischer-Gödde M, Kleine T, Burkhardt C, Dauphas N. 2014. Origin of nucleosynthetic isotope anomalies in bulk meteorites: Evidence from coupled Ru and Mo isotopes in acid leachates of chondrites. *Lunar Planet. Sci. Conf. Abstr.* 45:2409
- Franchi IA. 2008. Oxygen isotopes in asteroidal materials. *Rev. Mineral. Geochem.* 68:345–97
- Franchi IA, Wright IP, Sexton AS, Pillinger CT. 1999. The oxygen-isotopic composition of Earth and Mars. *Meteorit. Planet. Sci.* 34:657–61
- Fricke G, Heilig K. 2004. *Nuclear Charge Radii*. Berlin: Springer
- Fujii Y, Higuchi N, Haruno Y, Nomura M, Suzuki T. 2006a. Temperature dependence of isotope effects in uranium chemical exchange reactions. *J. Nucl. Sci. Technol.* 43:400–6
- Fujii T, Moynier F, Agranier A, Ponzevera E, Abe M. 2011a. Nuclear field shift effect of lead in ligand exchange reaction using a crown ether. *Proc. Radiochem.* 1:387–92
- Fujii T, Moynier F, Albarède F. 2006b. Nuclear field versus nucleosynthetic effects as cause of isotopic anomalies in the early Solar System. *Earth Planet. Sci. Lett.* 247:1–9
- Fujii T, Moynier F, Albarède F. 2009. The nuclear field shift effect in chemical exchange reactions. *Chem. Geol.* 267:139–56
- Fujii T, Moynier F, Dauphas N, Abe M. 2011b. Theoretical and experimental investigation of nickel isotopic fractionation in species relevant to modern and ancient oceans. *Geochim. Cosmochim. Acta* 75:469–82
- Fujii T, Moynier F, Telouk P, Abe M. 2010. Experimental and theoretical investigation of isotope fractionation of zinc between aqua, chloro, and macrocyclic complexes. *J. Phys. Chem. A* 114:2543–52



- Fujii T, Moynier F, Telouk P, Albarède F. 2006c. Mass-independent isotope fractionation of molybdenum and ruthenium and the origin of isotopic anomalies in Murchison. *Astrophys. J.* 647:1506–16
- Fujii Y, Nomura M, Okamoto M, Onitsuka H, Kawakami F, Takeda K. 1989. An anomalous isotope effect of  $^{235}\text{U}$  in U(IV)–U(VI) chemical exchange. *Z. Naturforsch. A* 44:395–98
- Gannoun A, Boyet M, Rizo H, El Goresy A. 2011.  $^{146}\text{Sm}$ – $^{142}\text{Nd}$  systematics measured in enstatite chondrites reveals a heterogeneous distribution of  $^{142}\text{Nd}$  in the solar nebula. *PNAS* 108:7693–97
- Gao YQ, Marcus RA. 2002. On the theory of the strange and unconventional isotopic effects in ozone formation. *J. Chem. Phys.* 116:137–54
- Ghosh P, Adkins J, Affek H, Balta B, Guo W, et al. 2006.  $^{13}\text{C}$ – $^{18}\text{O}$  bonds in carbonate minerals: a new kind of paleothermometer. *Geochim. Cosmochim. Acta* 70:1439–56
- Ghosh S, Schauble EA, Lacrampe Couloume G, Blum JD, Bergquist BA. 2013. Estimation of nuclear volume dependent fractionation of mercury isotopes in equilibrium liquid-vapor evaporation experiments. *Chem. Geol.* 336:5–12
- Ghosh S, Xu Y, Humayun M, Odom L. 2008. Mass-independent fractionation of mercury isotopes in the environment. *Geochem. Geophys. Geosyst.* 9:Q03004
- Glavin D, Kubny A, Jagoutz E, Lugmair G. 2004. Mn–Cr isotope systematics of the D’Orbigny angrite. *Meteorit. Planet. Sci.* 39:693–700
- Goldmann A, Brennecke G, Noordman J, Weyer S, Wadhwa M. 2015. The uranium isotopic composition of the Earth and the Solar System. *Geochim. Cosmochim. Acta* 148:145–58
- Göpel C, Birk J. 2010. Mn/Cr systematics: a tool to discriminate the origin of primitive meteorites. *Geochim. Cosmochim. Acta* 74:A348
- Göpel C, Birk JL, Galy A, Barrat JA, Zanda B. 2015. Mn–Cr systematics in primitive meteorites: insights from mineral separation and partial dissolution. *Geochim. Cosmochim. Acta* 156:1–24
- Gould IR, Turro NJ, Zimmt MB. 1984. Magnetic field and magnetic isotope effects on the products of organic reactions. *Adv. Phys. Org. Chem.* 20:1–53
- Gounelle M, Meynet G. 2012. Solar system genealogy revealed by extinct short-lived radionuclides in meteorites. *Astron. Astrophys.* 545:A4
- Grilly ER. 1951. The vapor pressures of hydrogen, deuterium and tritium up to three atmospheres. *J. Am. Chem. Soc.* 73:843–46
- Grimm R, McSween H Jr. 1993. Heliocentric zoning of the asteroid belt by aluminum-26 heating. *Science* 259:653–55
- Grossman L. 1972. Condensation in primitive solar nebula. *Geochim. Cosmochim. Acta* 36:597–619
- Grossman L, Beckett JR, Fedkin AV, Simon SB, Ciesla FJ. 2008. Redox conditions in the solar nebula: observational, experimental, and theoretical constraints. *Rev. Mineral. Geochem.* 68:93–140
- Hallis L, Anand M, Greenwood R, Miller MF, Franchi I, Russell S. 2010. The oxygen isotope composition, petrology and geochemistry of mare basalts: evidence for large-scale compositional variation in the lunar mantle. *Geochim. Cosmochim. Acta* 74:6885–99
- Hans U, Kleine T, Bourdon B. 2013. Rb–Sr chronology of volatile depletion in differentiated protoplanets: BABI, ADOR and ALL revisited. *Earth Planet. Sci. Lett.* 374:204–14
- Harper C, Wiesmann H, Nyquist L. 1991a.  $^{135}\text{Cs}$ – $^{135}\text{Ba}$ : very high precision isotopic investigations and a new cosmochronometric constraint on the astrophysical site of the origin of the solar system. *Meteoritics* 26:341
- Harper C, Wiesmann H, Nyquist L, Hartmann D, Meyer B, Howard W. 1991b. Interpretation of the  $^{50}\text{Ti}$ – $^{96}\text{Zr}$  anomaly correlation in CAI: NNSE Zr production limits and S/R/P decomposition of the bulk solar system zirconium abundances. *Lunar Planet. Sci. Conf. Abstr.* 22:517–18
- Harper C Jr., Wiesmann H, Nyquist L. 1992. The search for  $^{135}\text{Cs}$  in the early solar system: very high precision measurements of barium isotopes in bulk Allende and refractory inclusions. *Meteoritics* 27:230
- Hart SR, Zindler A. 1989. Isotope fractionation laws: a test using calcium. *Int. J. Mass Spectrom. Ion Process.* 89:287–301
- Hartmann WK, Davis DR. 1975. Satellite-sized planetesimals and lunar origin. *Icarus* 24:504–15
- Heidenreich JE, Thiemens MH. 1986. A non-mass-dependent oxygen isotope effect in the production of ozone from molecular oxygen: the role of molecular symmetry in isotope chemistry. *J. Chem. Phys.* 84:2129–36

- Herwartz D, Pack A, Friedrichs B, Bischoff A. 2014. Identification of the giant impactor Theia in lunar rocks. *Science* 344:1146–50
- Hess BA. 1986. Relativistic electronic-structure calculations employing a two-component no-pair formalism with external-field projection operators. *Phys. Rev. A* 33:3742–48
- Hidaka H, Ohta Y, Yoneda S. 2003. Nucleosynthetic components of the early solar system inferred from Ba isotopic compositions in carbonaceous chondrites. *Earth Planet. Sci. Lett.* 214:455–66
- Hidaka H, Yoneda S. 2011. Diverse nucleosynthetic components in barium isotopes of carbonaceous chondrites: incomplete mixing of s- and r-process isotopes and extinct  $^{135}\text{Cs}$  in the early solar system. *Geochim. Cosmochim. Acta* 75:3687–97
- Hiess J, Condon DJ, McLean N, Noble SR. 2012.  $^{238}\text{U}/^{235}\text{U}$  systematic in terrestrial uranium-bearing minerals. *Science* 335:1610–14
- Hirose K, Labrosse S, Hernlund J. 2013. Composition and state of the core. *Annu. Rev. Earth Planet. Sci.* 41:657–91
- Hofmann MEG, Horváth B, Pack A. 2012. Triple oxygen isotope equilibrium fractionation between carbon dioxide and water. *Earth Planet. Sci. Lett.* 319–20:159–64
- Holst JC, Olsen MB, Paton C, Nagashima K, Schiller M, et al. 2013.  $^{182}\text{Hf}$ - $^{182}\text{W}$  age dating of a  $^{26}\text{Al}$ -poor inclusion and implications for the origin of short-lived radioisotopes in the early Solar System. *PNAS* 110:8819–23
- Horita J, Wesolowski DJ. 1994. Liquid-vapor fractionation of oxygen and hydrogen isotopes of water from the freezing to the critical temperature. *Geochim. Cosmochim. Acta* 58:3425–37
- Hsu W, Guan Y, Leshin L, Ushikubo T, Wasserburg G. 2006. A late episode of irradiation in the early solar system: evidence from extinct  $^{36}\text{Cl}$  and  $^{26}\text{Al}$  in meteorites. *Astrophys. J.* 640:525
- Huang S, Farkaš J, Yu G, Petaev MI, Jacobsen SB. 2012. Calcium isotopic ratios and rare earth element abundances in refractory inclusions from the Allende CV3 chondrite. *Geochim. Cosmochim. Acta* 77:252–65
- Hulston JR, Thode HG. 1965. Variations in the  $\text{S}^{33}$ ,  $\text{S}^{34}$ , and  $\text{S}^{36}$  contents of meteorites and their relation to chemical and nuclear effects. *J. Geophys. Res.* 70:3475–84
- Humayun M, Brandon AD. 2007. s-Process implications from osmium isotope anomalies in chondrites. *Astrophys. J.* 664:L59
- Huss GR, Lewis RS. 1995. Presolar diamond, SiC, and graphite in primitive chondrites: abundances as a function of meteorite class and petrologic type. *Geochim. Cosmochim. Acta* 59:115–60
- Hynes K, Gyngard F. 2009. The Presolar Grain Database: <http://presolar.wustl.edu/~pgd>. *Lunar Planet. Sci. Conf. Abstr.* 40:1198
- Ireland TR. 1988. Correlated morphological, chemical, and isotopic characteristics of hibonites from the Murchison carbonaceous chondrite. *Geochim. Cosmochim. Acta* 52:2827–39
- Ireland TR. 1990. Presolar isotopic and chemical signatures in hibonite-bearing refractory inclusions from the Murchison carbonaceous chondrite. *Geochim. Cosmochim. Acta* 54:3219–37
- Ireland TR, Fahey AJ, Zinner EK. 1991. Hibonite-bearing microspherules: a new type of refractory inclusions with large isotopic anomalies. *Geochim. Cosmochim. Acta* 55:367–79
- Jacobsen B, Yin Q, Moynier F, Amelin Y, Krot AN, et al. 2008.  $^{26}\text{Al}$ - $^{26}\text{Mg}$  and  $^{207}\text{Pb}$ - $^{206}\text{Pb}$  systematics of Allende CAIs: canonical solar initial  $^{26}\text{Al}/^{27}\text{Al}$  ratio reinstated. *Earth Planet. Sci. Lett.* 272:353–64
- Javoy M. 1995. The integral enstatite chondrite model of the Earth. *Geophys. Res. Lett.* 22:2219–22
- Javoy M, Kaminski E, Guyot F, Andraut D, Sanloup C, et al. 2010. The chemical composition of the Earth: enstatite chondrite models. *Earth Planet. Sci. Lett.* 293:259–68
- Jeffery P, Reynolds J. 1961. Origin of excess  $\text{Xe}^{129}$  in stone meteorites. *J. Geophys. Res.* 66:3582–83
- Johnston DT. 2011. Multiple sulfur isotopes and the evolution of Earth's surface sulfur cycle. *Earth-Sci. Rev.* 106:161–83
- Johnston DT, Farquhar J, Habicht KS, Canfield DE. 2008. Sulphur isotopes and the search for life: strategies for identifying sulphur metabolisms in the rock record and beyond. *Geobiology* 6:425–35
- Jungck M, Shimamura T, Lugmair G. 1984. Ca isotope variations in Allende. *Geochim. Cosmochim. Acta* 48:2651–58
- Kaib NA, Cowan NB. 2015. The feeding zones of terrestrial planets and insights into Moon formation. *Icarus* 252:161–74

- Kaminski E, Javoy M. 2013. A two-stage scenario for the formation of the Earth's mantle and core. *Earth Planet. Sci. Lett.* 365:97–107
- King WH. 1984. *Isotope Shifts in Atomic Spectra*. New York: Plenum
- Kleine T, Hans U, Irving AJ, Bourdon B. 2012. Chronology of the angrite parent body and implications for core formation in protoplanets. *Geochim. Cosmochim. Acta* 84:186–203
- Knyazev DA, Myasoedov NF. 2001. Specific effects of heavy nuclei in chemical equilibrium. *Sep. Sci. Technol.* 36:1677–96
- Kobayashi S, Imai H, Yurimoto H. 2003. New extreme  $^{16}\text{O}$ -rich chondrule in the early solar system. *Geochim. J.* 37:663–69
- Kokubo E, Ida S. 1998. Oligarchic growth of protoplanets. *Icarus* 131:171–78
- Kööp L, Davis AM, Nakashima D, Park C, Krot AN, et al. 2016. A link between oxygen, calcium and titanium isotopes in  $^{26}\text{Al}$ -depleted hibonite-rich CAIs from Murchison and implications for the heterogeneity of dust reservoirs in the solar nebula. *Geochim. Cosmochim. Acta*. Submitted
- Krankowsky D, Lämmerzahl P, Mauersberger K, Janssen C, Tuzson B, Röckmann T. 2007. Scollected samples. *J. Geophys. Res.* 112:D08301
- Krot AN, Keil K, Scott ERD, Goodrich CA, Weisberg MK. 2014. Classification of meteorites. In *Treatise on Geochemistry*, Vol. 1: *Meteorites, Comets, and Planets*, ed. AM Davis, pp. 1–63. Oxford, UK: Elsevier-Pergamon. 2nd ed.
- Kruijjer TS, Kleine T, Fischer-Gödde M, Burkhardt C, Wieler R. 2014a. Nucleosynthetic W isotope anomalies and the Hf-W chronometry of Ca-Al-rich inclusions. *Earth Planet. Sci. Lett.* 403:317–27
- Kruijjer TS, Kleine T, Fischer-Gödde M, Sprung P. 2015. Lunar tungsten isotopic evidence for the late veneer. *Nature* 520:534–37
- Kruijjer TS, Touboul M, Fischer-Gödde M, Bermingham KR, Walker RJ, Kleine T. 2014b. Protracted core formation and rapid accretion of protoplanets. *Science* 344:1150–54
- Landais A, Barkan E, Luz B. 2008. The record of  $\delta^{18}\text{O}$  and  $^{17}\text{O}$ -excess in ice from Vostok Antarctica during the last 150,000 years. *Geophys. Res. Lett.* 35:L02709
- Landais A, Steen-Larsen HC, Guillevic M, Masson-Delmotte V, Vinther B, Winkler R. 2012. Triple isotopic composition of oxygen in surface snow and water vapor at NEEM (Greenland). *Geochim. Cosmochim. Acta* 77:304–16
- Larsen KK, Trinquier A, Paton C, Schiller M, Wielandt D, et al. 2011. Evidence for magnesium isotope heterogeneity in the solar protoplanetary disk. *Astrophys. J.* 735:L37
- Lee DC, Halliday AN, Leya I, Wieler R, Wiechert U. 2002. Cosmogenic tungsten and the origin and earliest differentiation of the Moon. *Earth Planet. Sci. Lett.* 198:267–74
- Lee T, Papanastassiou DA. 1974. Mg isotopic anomalies in the Allende meteorite and correlation with O and Sr effects. *Geophys. Res. Lett.* 1:225–28
- Lee T, Papanastassiou DA, Wasserburg GJ. 1976. Demonstration of Mg-26 excess in Allende and evidence for Al-26. *Geophys. Res. Lett.* 3:41–44
- Lee T, Papanastassiou DA, Wasserburg GJ. 1977. Aluminum-26 in the early solar system: fossil or fuel? *Astrophys. J.* 211:L107–10
- Lee T, Russell W, Wasserburg G. 1979. Calcium isotopic anomalies and the lack of aluminum-26 in an unusual Allende inclusion. *Astrophys. J.* 228:L93–98
- Levin NE, Raub TD, Dauphas N, Eiler JM. 2014. Triple oxygen isotope variations in sedimentary rocks. *Geochim. Cosmochim. Acta* 139:173–89
- Lewis R, Tang M, Wacker JF, Anders E, Steel E. 1987. Interstellar diamonds in meteorites. *Nature* 326:160–62
- Leya I, Schönbächler M, Krähenbühl U, Halliday AN. 2009. New titanium isotope data for Allende and Efremovka CAIs. *Astrophys. J.* 702:1118
- Liu MC, McKeegan KD, Goswami JN, Marhas KK, Sahijpal S, et al. 2009. Isotopic records in CM hibonites: implications for timescales of mixing of isotope reservoirs in the solar nebula. *Geochim. Cosmochim. Acta* 73:5051–79
- Liu Q, Tossell JA, Liu Y. 2010. On the proper use of the Bigeleisen–Mayer equation and corrections to it in the calculation of isotopic fractionation equilibrium constants. *Geochim. Cosmochim. Acta* 74:6965–83
- Lodders K, Amari S. 2005. Presolar grains from meteorites: remnants from the early times of the solar system. *Chem. Erde Geochem.* 65:93–166

- Lodders K, Fegley B. 1997. An oxygen isotope model for the composition of Mars. *Icarus* 126:373–94
- Loss R, Lugmair G. 1990. Zinc isotope anomalies in Allende meteorite inclusions. *Astrophys. J.* 360:L59–62
- Loss R, Lugmair G, Davis A, MacPherson G. 1994. Isotopically distinct reservoirs in the solar nebula: isotope anomalies in Vigarano meteorite inclusions. *Astrophys. J.* 436:L193–96
- Lugmair G, Shukolyukov A. 1998. Early solar system timescales according to  $^{53}\text{Mn}$ - $^{53}\text{Cr}$  systematics. *Geochim. Cosmochim. Acta* 62:2863–86
- Luz B, Barkan E. 2000. Assessment of oceanic productivity with the triple-isotope composition of dissolved oxygen. *Science* 288:2028–31
- Luz B, Barkan E. 2010. Variations of  $^{17}\text{O}/^{16}\text{O}$  and  $^{18}\text{O}/^{16}\text{O}$  in meteoric waters. *Geochim. Cosmochim. Acta* 74:6276–86
- Luz B, Barkan E, Bender M, Thieme M, Boering KA. 1999. Triple-isotope composition of atmospheric oxygen as a tracer of biosphere productivity. *Science* 400:547–50
- Lyons JR. 2001. Transfer of mass-independent fractionation in ozone to other oxygen-containing radicals in the atmosphere. *Geophys. Res. Lett.* 28:3231–34
- Lyons JR. 2007. Mass-independent fractionation of sulfur isotopes by isotope-selective dissociation of  $\text{SO}_2$ . *Geophys. Res. Lett.* 34:L22811
- Lyons JR, Young ED. 2005. CO self-shielding as the origin of oxygen isotope anomalies in the early solar nebula. *Nature* 435:317–20
- MacPherson G, Bullock E, Janney P, Davis A, Wadhwa M, Krot A. 2007. High precision Al-Mg isotope studies of condensate CAIs. *Lunar Planet. Sci. Conf. Abstr.* 38:1378
- Marcus RA. 2004. Mass-independent isotope effect in the earliest processed solids in the solar system: a possible mechanism. *J. Chem. Phys.* 121:8201–11
- Maréchal CN, Télouk P, Albarède F. 1999. Precise analysis of copper and zinc isotopic compositions by plasma-source mass spectrometry. *Chem. Geol.* 156:251–73
- Markowski A, Quitté G, Halliday A, Kleine T. 2006. Tungsten isotopic compositions of iron meteorites: chronological constraints versus cosmogenic effects. *Earth Planet. Sci. Lett.* 242:1–15
- Martin E, Bindeman I. 2009. Mass-independent isotopic signatures of volcanic sulfate from three supereruption ash deposits in Lake Tecopa, California. *Earth Planet. Sci. Lett.* 282:102–14
- Mason B, Taylor SR. 1982. Inclusions in the Allende meteorite. *Smithson. Contrib. Earth Sci.* 1:30
- Mastrobuono-Battisti A, Perets HB, Raymond SN. 2015. A primordial origin for the compositional similarity between the Earth and the Moon. *Nature* 520:212–15
- Matsuhisa Y, Goldsmith JR, Clayton RN. 1978. Mechanisms of hydrothermal crystallization of quartz at 250°C and 15 kbar. *Geochim. Cosmochim. Acta* 42:173–82
- Mauersberger K. 1987. Ozone isotope measurements in the stratosphere. *Geophys. Res. Lett.* 14:80–83
- Mauersberger K, Erbacer B, Krankowsky D, Günther J, Nickel R. 1999. Ozone isotope enrichment: isotopomer-specific rate coefficients. *Science* 283:370–72
- Mayer B, Wittig N, Humayun M, Leya I. 2015. Palladium isotopic evidence for nucleosynthetic and cosmogenic isotope anomalies in IVB iron meteorites. *Astrophys. J.* 809:180
- McCulloch M, Wasserburg G. 1978a. Barium and neodymium isotopic anomalies in the Allende meteorite. *Astrophys. J.* 220:L15–19
- McCulloch M, Wasserburg G. 1978b. More anomalies from the Allende meteorite: samarium. *Geophys. Res. Lett.* 5:599–602
- McKeegan K, Kallio A, Heber V, Jarzebinski G, Mao P, et al. 2011. The oxygen isotopic composition of the Sun inferred from captured solar wind. *Science* 332:1528–32
- McSween HY, Binzel RP, De Sanctis MC, Ammannito E, Prettyman TH, et al. 2013. Dawn; the Vesta–HED connection; and the geologic context for eucrites, diogenites, and howardites. *Meteorit. Planet. Sci.* 48:2090–104
- Meijer HAJ, Li WJ. 1998. The use of electrolysis for accurate  $\delta^{17}\text{O}$  and  $\delta^{18}\text{O}$  isotope measurements of water. *Isotop. Environ. Health Stud.* 34:349
- Merrill P. 1952. Technetium in the stars. *Science* 115:479–89
- Messenger S, Keller LP, Stadermann FJ, Walker RM, Zinner E. 2003. Samples of stars beyond the solar system: silicate grains in interplanetary dust. *Science* 300:105–8

- Miller CA, Peucker-Ehrenbrink B, Schauble EA. 2015. Theoretical modeling of rhenium isotope fractionation, natural variations across a black shale weathering profile, and potential as a paleoredox proxy. *Earth Planet. Sci. Lett.* 430:339–48
- Miller MF. 2002. Isotopic fractionation and the quantification of  $^{17}\text{O}$  anomalies in the oxygen three-isotope system: an appraisal and geochemical significance. *Geochim. Cosmochim. Acta* 66:1881–89
- Ming T, Anders E. 1988. Isotopic anomalies of Ne, Xe, and C in meteorites. II. Interstellar diamond and SiC: carriers of exotic noble gases. *Geochim. Cosmochim. Acta* 52:1235–44
- Mioduski T. 1999. Comment to the Bigeleisen's theory of isotope chemistry of the heavy elements. *Comments Inorg. Chem.* 21:175–96
- Mittlefehldt DW. 2005. Ibitira: a basaltic achondrite from a distinct parent asteroid and implications for the Dawn mission. *Meteorit. Planet. Sci.* 40:665–77
- Mook WG. 2000. *Environmental Isotopes in the Hydrological Cycle: Principles and Applications*, Vol. 1: Introduction—Theory, Methods, Review. Geneva: Int. At. Energy Agency
- Morton J, Barnes J, Schueler B, Mauersberger K. 1990. Laboratory studies of heavy ozone. *J. Geophys. Res.* 95(D1):901–7
- Mosconi M, Fujii K, Mengoni A, Domingo-Pardo C, Käppeler F, et al. 2010. Neutron physics of the Re/Os clock. I. Measurement of the ( $n, \gamma$ ) cross sections of  $^{186,187,188}\text{Os}$  at the CERN n\_TOF facility. *Phys. Rev. C* 82:015802
- Moynier F, Day JM, Okui W, Yokoyama T, Bouvier A, et al. 2012. Planetary-scale strontium isotopic heterogeneity and the age of volatile depletion of early Solar System materials. *Astrophys. J.* 758:45
- Moynier F, Fujii T, Albarède F. 2009. Nuclear field shift effect as a possible cause of Te isotopic anomalies in the early solar system—an alternative explanation of Fehr et al. (2006 and 2009). *Meteorit. Planet. Sci.* 44:1735–42
- Moynier F, Fujii T, Brennecka GA, Nielsen SG. 2013. Nuclear field shift in natural environments. *C.R. Geosci.* 345:150–59
- Moynier F, Simon JL, Podosek FA, Meyer BS, Brannon J, DePaolo DJ. 2010. Ca isotope effects in Orgueil leachates and the implications for the carrier phases of  $^{54}\text{Cr}$  anomalies. *Astrophys. J.* 718:L7
- Münker C. 2010. A high field strength element perspective on early lunar differentiation. *Geochim. Cosmochim. Acta* 74:7340–61
- Murphy MJ, Stirling CH, Kaltenbach A, Turner SP, Schaefer BF. 2014. Fractionation of  $^{238}\text{U}/^{235}\text{U}$  by reduction during low temperature uranium mineralisation processes. *Earth Planet. Sci. Lett.* 388:306–17
- Nemoto K, Abe M, Seino J, Hada M. 2015. An ab initio study of nuclear volume effects for isotope fractionations using two-component relativistic methods. *J. Comput. Chem.* 36:816–20
- Nguyen AN, Zinner E. 2004. Discovery of ancient silicate stardust in a meteorite. *Science* 303:1496–99
- Nicolussi G, Pellin M, Lewis R, Davis A, Amari S, Clayton R. 1998. Molybdenum isotopic composition of individual presolar silicon carbide grains from the Murchison meteorite. *Geochim. Cosmochim. Acta* 62:1093–104
- Niederer FR, Papanastassiou DA. 1984. Ca isotopes in refractory inclusions. *Geochim. Cosmochim. Acta* 48:1279–93
- Niederer FR, Papanastassiou DA, Wasserburg GJ. 1981. The isotopic composition of titanium in the Allende and Leoville meteorites. *Geochim. Cosmochim. Acta* 45:1017–31
- Niederer FR, Papanastassiou DA, Wasserburg GJ. 1985. Absolute isotopic abundances of Ti in meteorites. *Geochim. Cosmochim. Acta* 49:835–51
- Nielsen SG, Rehkämper M, Norman MD, Halliday AN, Harrison D. 2006a. Thallium isotopic evidence for ferromanganese sediments in the mantle source of Hawaiian basalts. *Nature* 439:314–17
- Nielsen SG, Rehkämper M, Teagle DAH, Butterfield DA, Alt JC, Halliday AN. 2006b. Hydrothermal fluid fluxes calculated from the isotopic mass balance of thallium in the ocean crust. *Earth Planet. Sci. Lett.* 251:120–33
- Nielsen SG, Wasylenki LE, Rehkämper M, Peacock CL, Xue Z, Moon EM. 2013. Towards an understanding of thallium isotope fractionation during adsorption to manganese oxides. *Geochim. Cosmochim. Acta* 117:252–65
- Niemeyer S. 1988. Isotopic diversity in nebular dust: the distribution of Ti isotopic anomalies in carbonaceous chondrites. *Geochim. Cosmochim. Acta* 52:2941–54

- Niemeyer S, Lugmair G. 1981. Ubiquitous isotopic anomalies in Ti from normal Allende inclusions. *Earth Planet. Sci. Lett.* 53:211–25
- Niemeyer S, Lugmair G. 1984. Titanium isotopic anomalies in meteorites. *Geochim. Cosmochim. Acta* 48:1401–16
- Nishizawa K, Satoyama T, Miki T, Yamamoto T, Hosoe M. 1995. Strontium isotope effect in liquid-liquid extraction of strontium chloride using a crown ether. *J. Nucl. Sci. Technol.* 32:1230–35
- Nittler LR, Alexander CMD, Gao X, Walker RM, Zinner EK. 1994. Interstellar oxide grains from the Tieschitz ordinary chondrite. *Nature* 370:443–46
- Nittler LR, Alexander CMD, Gao X, Walker RM, Zinner EK. 1997. Stellar sapphires: the properties and origins of presolar Al<sub>2</sub>O<sub>3</sub> in meteorites. *Astrophys. J.* 483:475
- Nittler LR, Hoppe P, Alexander CMD, Amari S, Eberhardt P, et al. 1995. Silicon nitride from supernovae. *Astrophys. J.* 453:L25
- Nomura M, Higuchi N, Fujii Y. 1996. Mass dependence of uranium isotope effects in the U(IV)–U(VI) exchange reaction. *J. Am. Chem. Soc.* 118:9127–30
- Nozawa T, Maeda K, Kozasa T, Tanaka M, Nomoto Ki, Umeda H. 2011. Formation of dust in the ejecta of type Ia supernovae. *Astrophys. J.* 736:45
- Nyquist L, Kleine T, Shih CY, Reese Y. 2009. The distribution of short-lived radioisotopes in the early solar system and the chronology of asteroid accretion, differentiation, and secondary mineralization. *Geochim. Cosmochim. Acta* 73:5115–36
- Oduro H, Harms B, Sintim HO, Kaufman AJ, Cody G, Farquhar J. 2011. Evidence of magnetic isotope effects during thermochemical sulfate reduction. *PNAS* 108:17635–38
- Ono S, Wing B, Johnston D, Farquhar J, Rumble D. 2006. Mass-dependent fractionation of quadruple stable sulfur isotope system as a new tracer of sulfur biogeochemical cycles. *Geochim. Cosmochim. Acta* 70:2238–52
- Otake T, Lasaga AC, Ohmoto H. 2008. Ab initio calculations for equilibrium fractionations in multiple sulfur isotope systems. *Chem. Geol.* 249:357–76
- Pack A, Gehler A, Süssenger A. 2013. Exploring the usability of isotopically anomalous oxygen in bones and teeth as paleo-CO<sub>2</sub>-barometer. *Geochim. Cosmochim. Acta* 102:306–17
- Pack A, Herwartz D. 2014. The triple oxygen isotope composition of the Earth mantle and understanding δ<sup>17</sup>O variations in terrestrial rocks and minerals. *Earth Planet. Sci. Lett.* 390:138–45
- Pahlevan K, Stevenson DJ. 2007. Equilibration in the aftermath of the lunar-forming giant impact. *Earth Planet. Sci. Lett.* 262:438–49
- Pahlevan K, Stevenson DJ, Eiler JM. 2011. Chemical fractionation in the silicate vapor atmosphere of the Earth. *Earth Planet. Sci. Lett.* 301:433–43
- Papanastassiou D. 1986. Chromium isotopic anomalies in the Allende meteorite. *Astrophys. J.* 308:L27–30
- Papanastassiou D, Brigham C. 1989. The identification of meteorite inclusions with isotope anomalies. *Astrophys. J.* 338:L37–40
- Papanastassiou D, Wasserburg G. 1978. Strontium isotopic anomalies in the Allende meteorite. *Geophys. Res. Lett.* 5:595–98
- Park C, Nagashima K, Hutcheon I, Wasserburg G, Papanastassiou D, et al. 2013. Heterogeneity of Mg isotopes and variable <sup>26</sup>Al/<sup>27</sup>Al Ratio in FUN CAIs. *Meteorit. Planet. Sci.* 76(Suppl.):5085
- Park C, Nagashima K, Wasserburg G, Papanastassiou D, Hutcheon I, et al. 2014. Calcium and titanium isotopic compositions of FUN CAIs: implications for their origin. *Lunar Planet. Sci. Conf. Abstr.* 45:2656
- Passy BH, Hu H, Ji H, Montanari S, Li S, et al. 2014. Triple oxygen isotopes in biogenic and sedimentary carbonates. *Geochim. Cosmochim. Acta* 141:1–25
- Paton C, Schiller M, Bizzarro M. 2013. Identification of an <sup>84</sup>Sr-depleted carrier in primitive meteorites and implications for thermal processing in the solar protoplanetary disk. *Astrophys. J.* 763:L40
- Pavlov AA, Kasting JF. 2002. Mass-independent fractionation of sulfur isotopes in Archean sediments: strong evidence for an anoxic Archean atmosphere. *Astrobiology* 2:27–41
- Peacock CL, Moon EM. 2012. Oxidative scavenging of thallium by birnessite: controls on thallium sorption and stable isotope fractionation in marine ferromanganese precipitates. *Geochim. Cosmochim. Acta* 84:297–313

- Pinella C, Blanchard M, Balan E, Natarajan SK, Vuilleumier R, Mauri F. 2015. Equilibrium magnesium isotope fractionation between aqueous  $Mg^{2+}$  and carbonate minerals: insights from path integral molecular dynamics. *Geochim. Cosmochim. Acta* 163:126–39
- Podosek F, Ott U, Brannon J, Neal C, Bernatowicz T, et al. 1997. Thoroughly anomalous chromium in Orgueil. *Meteorit. Planet. Sci.* 32:617–27
- Pyper JW, Christensen LD. 1975. Equilibrium constants of hydrogen-deuterium-tritium self-exchange reactions in water vapor as studied with a pulsed molecular-beam quadrupole mass filter. *J. Chem. Phys.* 62:2596
- Qin L, Alexander CMD, Carlson RW, Horan MF, Yokoyama T. 2010a. Contributors to chromium isotope variation of meteorites. *Geochim. Cosmochim. Acta* 74:1122–45
- Qin L, Carlson RW, Alexander CMD. 2011a. Correlated nucleosynthetic isotopic variability in Cr, Sr, Ba, Sm, Nd and Hf in Murchison and QUE 97008. *Geochim. Cosmochim. Acta* 75:7806–28
- Qin L, Dauphas N, Horan MF, Leya I, Carlson RW. 2015. Correlated cosmogenic W and Os isotopic variations in Carbo and implications for Hf-W chronology. *Geochim. Cosmochim. Acta* 153:91–104
- Qin L, Dauphas N, Wadhwa M, Markowski A, Gallino R, et al. 2008a. Tungsten nuclear anomalies in planetesimal cores. *Astrophys. J.* 674:1234–41
- Qin L, Dauphas N, Wadhwa M, Masarik J, Janney PE. 2008b. Rapid accretion and differentiation of iron meteorite parent bodies inferred from  $^{182}\text{Hf}$ – $^{182}\text{W}$  chronometry and thermal modeling. *Earth Planet. Sci. Lett.* 273:94–104
- Qin L, Nittler LR, Alexander CMD, Wang J, Stadermann FJ, Carlson RW. 2011b. Extreme  $^{54}\text{Cr}$ -rich nano-oxides in the CI chondrite Orgueil: implication for a late supernova injection into the solar system. *Geochim. Cosmochim. Acta* 75:629–44
- Qin L, Rumble D, Alexander CMD, Carlson RW, Jenniskens P, Shaddad MH. 2010b. The chromium isotopic composition of Almahata Sitta. *Meteorit. Planet. Sci.* 45:1771–77
- Quitté G, Markowski A, Latkoczy C, Gabriel A, Pack A. 2010. Iron-60 heterogeneity and incomplete isotope mixing in the early solar system. *Astrophys. J.* 720:1215
- Rankenburg K, Brandon A, Neal C. 2006. Neodymium isotope evidence for a chondritic composition of the Moon. *Science* 312:1369–72
- Rauscher T, Dauphas N, Dillmann I, Fröhlich C, Fülöp Z, Gyürky G. 2013. Constraining the astrophysical origin of the p-nuclei through nuclear physics and meteoritic data. *Rep. Prog. Phys.* 76:066201
- Rauscher T, Heger A, Hoffmann RD, Woosley SE. 2002. Nucleosynthesis in massive stars with improved nuclear and stellar physics. *Astrophys. J.* 576:323–48
- Regelous M, Elliott T, Coath CD. 2008. Nickel isotope heterogeneity in the early Solar System. *Earth Planet. Sci. Lett.* 272:330–38
- Rehkämper M, Frank M, Hein JR, Porcelli D, Halliday A, et al. 2002. Thallium isotope variations in seawater and hydrogenetic, diagenetic, and hydrothermal ferromanganese deposits. *Earth Planet. Sci. Lett.* 197:65–81
- Rehkämper M, Halliday AN. 1999. The precise measurement of Tl isotopic compositions by MC-ICPMS: application to the analysis of geological materials and meteorites. *Geochim. Cosmochim. Acta* 63:935–44
- Reisberg L, Dauphas N, Luguet A, Pearson D, Gallino R, Zimmermann C. 2009. Nucleosynthetic osmium isotope anomalies in acid leachates of the Murchison meteorite. *Earth Planet. Sci. Lett.* 277:334–44
- Richtel P, Bottinga Y, Javoy M. 1977. A review of hydrogen, carbon, nitrogen, oxygen, sulphur, and chlorine stable isotope fractionation among gaseous molecules. *Annu. Rev. Earth Planet. Sci.* 5:65–110
- Richter S, Ott U, Begemann F. 1998. Tellurium in pre-solar diamonds as an indicator for rapid separation of supernova ejecta. *Nature* 391:261–63
- Rotaru M, Birck JL, Allegre CJ. 1992. Clues to early solar system history from chromium isotopes in carbonaceous chondrites. *Nature* 358:465–70
- Rowe M, Kuroda P. 1965. Fissionogenic xenon from the Pasamonte meteorite. *J. Geophys. Res.* 70:709–14
- Rubie DC, Frost DJ, Mann U, Asahara Y, Nimmo F, et al. 2011. Heterogeneous accretion, composition and core-mantle differentiation of the Earth. *Earth Planet. Sci. Lett.* 301:31–42
- Rumble D, Miller MF, Franchi IA, Greenwood RC. 2007. Oxygen three-isotope fractionation lines in terrestrial silicate minerals: an inter-laboratory comparison of hydrothermal quartz and eclogitic garnet. *Geochim. Cosmochim. Acta* 71:3592–600

- Russell W, Papanastassiou D, Tombrello T. 1978. Ca isotope fractionation on the Earth and other solar system materials. *Geochim. Cosmochim. Acta* 42:1075–90
- Sahijpal S, Goswami J, Davis A. 2000. K, Mg, Ti and Ca isotopic compositions and refractory trace element abundances in hibonites from CM and CV meteorites: implications for early solar system processes. *Geochim. Cosmochim. Acta* 64:1989–2005
- Sakamoto N, Seto Y, Itoh S, Kuramoto K, Fujino K, et al. 2008. Remnants of the early solar system water enriched in heavy oxygen isotopes. *Science* 317:231–33
- Sanloup C, Jambon A, Gillet P. 1999. A simple chondritic model of Mars. *Phys. Earth Planet. Inter.* 112:43–54
- Savarino J, Romero A, Cole-Dai JH, Bekki S, Thiemens MH. 2003. UV induced mass-independent sulfur isotope fractionation in stratospheric volcanic sulfate. *Geophys. Res. Lett.* 30:2131
- Savina MR, Davis AM, Tripa CE, Pellin MJ, Gallino R, et al. 2004. Extinct technetium in silicon carbide stardust grains: implications for stellar nucleosynthesis. *Science* 303:649–52
- Schauble EA. 2004. Applying stable isotope fractionation theory to new systems. *Rev. Mineral. Geochem.* 55:65–111
- Schauble EA. 2006. Equilibrium uranium isotope fractionation by nuclear volume and mass-dependent processes. *Eos Trans. AGU* 87(Fall Meet. Suppl.):V21B-0570 (Abstr.)
- Schauble EA. 2007. Role of nuclear volume in driving equilibrium stable isotope fractionation of mercury, thallium and other very heavy elements. *Geochim. Cosmochim. Acta* 71:2170–89
- Schauble EA. 2008. Mass-dependent and independent fractionation of Mo and Re. *Eos Trans. AGU* 89(Fall Meet. Suppl.):V43G-2212 (Abstr.)
- Schauble EA. 2011. First-principles estimates of equilibrium magnesium isotope fractionation in silicate, oxide, carbonate and hexaaquamagnesium<sup>2+</sup> crystals. *Geochim. Cosmochim. Acta* 75:844–69
- Schauble EA. 2013a. *Modeling nuclear field shift isotope fractionation in crystals*. Presented at AGU Fall Meet., Dec. 1–9, San Francisco, Abstr. V51A-2645
- Schauble EA. 2013b. Modeling nuclear volume isotope effects in crystals. *PNAS* 110:17714–19
- Scherstén A, Elliott T, Hawkesworth C, Russell S, Masarik J. 2006. Hf-W evidence for rapid differentiation of iron meteorite parent bodies. *Earth Planet. Sci. Lett.* 241:530–42
- Schiller M, Baker JA, Bizzarro M. 2010. <sup>26</sup>Al–<sup>26</sup>Mg dating of asteroidal magmatism in the young Solar System. *Geochim. Cosmochim. Acta* 74:4844–64
- Schiller M, Paton C, Bizzarro M. 2015. Evidence for nucleosynthetic enrichment of the protosolar molecular cloud core by multiple supernova events. *Geochim. Cosmochim. Acta* 149:88–102
- Schiller M, Van Kooten E, Holst JC, Olsen MB, Bizzarro M. 2014. Precise measurement of chromium isotopes by MC-ICPMS. *J. Anal. At. Spectrom.* 29:1406–16
- Schönbächler M, Lee DC, Rehkämper M, Halliday AN, Fehr MA, et al. 2003. Zirconium isotope evidence for incomplete admixing of *r*-process components in the solar nebula. *Earth Planet. Sci. Lett.* 216:467–81
- Schönbächler M, Rehkämper M, Fehr MA, Halliday AN, Hattendorf B, Günther D. 2005. Nucleosynthetic zirconium isotope anomalies in acid leachates of carbonaceous chondrites. *Geochim. Cosmochim. Acta* 69:5113–22
- Schueler B, Morton J, Mauersberger K. 1990. Measurement of isotopic abundances in collected stratospheric ozone samples. *Geophys. Res. Lett.* 17:1295–98
- Scott ERD, Greenwood RC, Franchi IA, Sanders IS. 2009. Oxygen isotopic constraints on the origin and parent bodies of eucrites, diogenites, and howardites. *Geochim. Cosmochim. Acta* 73:5835–53
- Scott ERD, Krot AN. 2005. Chondritic meteorites and the high-temperature nebular origins of their components. *Astron. Soc. Pac. Conf. Ser.* 341:15–53
- Severinghaus JP, Bender ML, Keeling RF, Broecker WS. 1996. Fractionation of soil gases by diffusion of water vapor, gravitational settling, and thermal diffusion. *Geochim. Cosmochim. Acta* 60:1005–18
- Shollenberger Q, Brennecka G, Borg L. 2015. The strontium, barium, neodymium, and samarium isotopic compositions of non-Allende CAIs. *Lunar Planet. Sci. Conf. Abstr.* 46:2593
- Shukolyukov A, Lugmair G. 2006a. Manganese-chromium isotope systematics of carbonaceous chondrites. *Earth Planet. Sci. Lett.* 250:200–13
- Shukolyukov A, Lugmair G. 2006b. The Mn-Cr isotope systematics in the ureilites Kenna and LEW 85440. *Lunar Planet. Sci. Conf. Abstr.* 37:1478



- Skaron S, Wolfsberg M. 1980. Anomalies in the fractionation by chemical equilibrium of  $^{18}\text{O}/^{16}\text{O}$  relative to  $^{17}\text{O}/^{16}\text{O}$ . *J. Chem. Phys.* 72:6810–11
- Smith RL, Pontoppidan KM, Young ED, Morris MR, van Dishoeck EF. 2009. High-precision  $\text{C}^{17}\text{O}$ ,  $\text{C}^{18}\text{O}$ , and  $\text{C}^{16}\text{O}$  measurements in young stellar objects: analogues for CO self-shielding in the early solar system. *Astrophys. J.* 701:163–75
- Spicuzza MJ, Day J, Taylor LA, Valley JW. 2007. Oxygen isotope constraints on the origin and differentiation of the Moon. *Earth Planet. Sci. Lett.* 253:254–65
- Spivak-Birndorf L, Wadhwa M, Janney P. 2009.  $^{26}\text{Al}$ - $^{26}\text{Mg}$  systematics in D'Orbigny and Sahara 99555 angrites: implications for high-resolution chronology using extinct chronometers. *Geochim. Cosmochim. Acta* 73:5202–11
- Sprung P, Scherer EE, Upadhyay D, Leya I, Mezger K. 2010. Non-nucleosynthetic heterogeneity in non-radiogenic stable Hf isotopes: implications for early solar system chronology. *Earth Planet. Sci. Lett.* 295:1–11
- Steele RC, Coath CD, Regelous M, Russell S, Elliott T. 2012. Neutron-poor nickel isotope anomalies in meteorites. *Astrophys. J.* 758:59
- Steele RC, Elliott T, Coath CD, Regelous M. 2011. Confirmation of mass-independent Ni isotopic variability in iron meteorites. *Geochim. Cosmochim. Acta* 75:7906–25
- Stirling CH, Andersen MB, Potter EK, Halliday AN. 2007. Low-temperature isotopic fractionation of uranium. *Earth Planet. Sci. Lett.* 264:208–25
- Stroud RM, Chisholm MF, Heck PR, Alexander CMD, Nittler LR. 2011. Supernova shock-wave-induced co-formation of glassy carbon and nanodiamond. *Astrophys. J.* 738:L27
- Sugiura N, Miyazaki A, Yanai K. 2005. Widespread magmatic activities on the angrite parent body at 4562 Ma ago. *Earth Planets Space* 57:e13–16
- Sun T, Bao H. 2011. Non-mass-dependent  $^{17}\text{O}$  anomalies generated by a superimposed thermal gradient on a rarefied  $\text{O}_2$  gas in a closed system. *Rapid Commun. Mass Spectrom.* 25:20–24
- Tang H, Dauphas N. 2012. Abundance, distribution, and origin of  $^{60}\text{Fe}$  in the solar protoplanetary disk. *Earth Planet. Sci. Lett.* 359:248–63
- Tang H, Dauphas N. 2014.  $^{60}\text{Fe}$ - $^{60}\text{Ni}$  chronology of core formation on Mars. *Earth Planet. Sci. Lett.* 390:264–74
- Tang H, Dauphas N. 2015. Low  $^{60}\text{Fe}$  abundance in Semarkona and Sahara 99555. *Astrophys. J.* 802:22
- Thiemens MH. 2006. History and applications of mass-independent isotope effects. *Annu. Rev. Earth Planet. Sci.* 34:217–62
- Thiemens MH, Chakraborty S, Dominguez G. 2012. The physical chemistry of mass-independent isotope effects and their observation in nature. *Annu. Rev. Phys. Chem.* 63:155–77
- Tissot FLH, Dauphas N. 2015. Uranium isotopic compositions of the crust and ocean: age corrections, U budget and global extent of modern anoxia. *Geochim. Cosmochim. Acta* 167:113–43
- Tissot FLH, Dauphas N, Grossman L. 2016. Origin of uranium isotope variations in early solar nebula condensates. *Sci. Adv.* 2:e1501400
- Touboul M, Puchtel IS, Walker RJ. 2015. Tungsten isotopic evidence for disproportional late accretion to the Earth and Moon. *Nature* 520:530–33
- Touboul M, Walker RJ. 2012. High precision tungsten isotope measurement by thermal ionization mass spectrometry. *Int. J. Mass Spectrom.* 309:109–17
- Trinquier A, Birck JL, Allègre CJ. 2007. Widespread  $^{54}\text{Cr}$  heterogeneity in the inner solar system. *Astrophys. J.* 655:1179
- Trinquier A, Birck JL, Allègre C, Göpel C, Ulfbeck D. 2008.  $^{53}\text{Mn}$ - $^{53}\text{Cr}$  systematics of the early Solar System revisited. *Geochim. Cosmochim. Acta* 72:5146–63
- Trinquier A, Elliott T, Ulfbeck D, Coath C, Krot AN, Bizzarro M. 2009. Origin of nucleosynthetic isotope heterogeneity in the solar protoplanetary disk. *Science* 324:374–76
- Turro NJ. 1983. Influence of nuclear spin on chemical reactions: magnetic isotope and magnetic field effects (a review). *PNAS* 80:609–21
- Uemura R, Barkan E, Abe O, Luz B. 2010. Triple isotope composition of oxygen in atmospheric water vapor. *Geophys. Res. Lett.* 37:L04402

- Urey H. 1947. The thermodynamic properties of isotopic substances. *J. Chem. Soc.* 1947:562–81
- Villeneuve J, Chaussidon M, Libourel G. 2009. Homogeneous distribution of  $^{26}\text{Al}$  in the solar system from the Mg isotopic composition of chondrules. *Science* 325:985–88
- Visser R, van Dishoeck E, Doty S, Dullemond C. 2009. The chemical history of molecules in circumstellar disks. *Astron. Astrophys.* 495:881–97
- Völkening J, Papanastassiou D. 1989. Iron isotope anomalies. *Astrophys. J.* 347:L43–46
- Völkening J, Papanastassiou D. 1990. Zinc isotope anomalies. *Astrophys. J.* 358:L29–32
- Walker RJ. 2009. Highly siderophile elements in the Earth, Moon and Mars: update and implications for planetary accretion and differentiation. *Chem. Erde Geochem.* 69:101–25
- Wanajo S, Janka HT, Müller B. 2013. Electron-capture supernovae as origin of  $^{48}\text{Ca}$ . *Astrophys. J.* 767:L26
- Wang W, Harris MJ, Diehl R, Halloin H, Cordier B, et al. 2007. SPI observations of the diffuse  $^{60}\text{Fe}$  emission in the Galaxy. *Astron. Astrophys.* 469:1005–12
- Wang X, Johnson TM, Lundstrom CC. 2015a. Isotope fractionation during oxidation of tetravalent uranium by dissolved oxygen. *Geochim. Cosmochim. Acta* 150:160–70
- Wang X, Johnson TM, Lundstrom CC. 2015b. Low temperature equilibrium isotope fractionation and isotope exchange kinetics between U(IV) and U(VI). *Geochim. Cosmochim. Acta* 158:262–75
- Warren PH. 2011. Stable-isotopic anomalies and the accretionary assemblage of the Earth and Mars: a subordinate role for carbonaceous chondrites. *Earth Planet. Sci. Lett.* 311:93–100
- Wasserburg GJ, Lee T, Papanastassiou DA. 1977. Correlated O and Mg isotopic anomalies in Allende inclusions: II. Magnesium. *Geophys. Res. Lett.* 4:299–302
- Wasserburg GJ, Wimpenny J, Yin QZ. 2012. Mg isotopic heterogeneity, Al-Mg isochrons, and canonical  $^{26}\text{Al}/^{27}\text{Al}$  in the early solar system. *Meteorit. Planet. Sci.* 47:1980–97
- Webb MA, Miller TF. 2014. Position-specific and clumped stable isotope studies: comparison of the Urey and path-integral approaches for carbon dioxide, nitrous oxide, methane, and propane. *J. Phys. Chem. A* 118:467–74
- Weston RE Jr. 1999. Anomalous or mass-independent isotope effects. *Chem. Rev.* 99:2115–36
- Wetherill GW, Stewart GR. 1989. Accumulation of a swarm of small planetesimals. *Icarus* 77:330–57
- Weyer S, Anbar AD, Gerdes A, Gordon GW, Algeo TJ, Boyle EA. 2008. Natural fractionation of  $^{238}\text{U}/^{235}\text{U}$ . *Geochim. Cosmochim. Acta* 72:345–59
- Widanagamage IH, Schauble EA, Scher HD, Griffith EM. 2014. Stable strontium isotope fractionation in synthetic barite. *Geochim. Cosmochim. Acta* 147:58–75
- Wiechert U, Halliday A, Lee DC, Snyder G, Taylor L, Rumble D. 2001. Oxygen isotopes and the Moon-forming giant impact. *Science* 294:345–48
- Wiechert U, Halliday A, Palme H, Rumble D. 2004. Oxygen isotope evidence for rapid mixing of the HED meteorite parent body. *Earth Planet. Sci. Lett.* 221:373–82
- Wiederhold JG, Cramer CJ, Daniel K, Infante I, Bourdon B, Kretzschmar R. 2010. Equilibrium mercury isotope fractionation between dissolved Hg(II) species and thiol-bound Hg. *Environ. Sci. Technol.* 44:4191–97
- Wiederhold JG, Sklyberg U, Drott A, Jiskra M, Jonsson S, et al. 2015. Mercury isotope signatures in contaminated sediments as a tracer for local industrial pollution sources. *Environ. Sci. Technol.* 49:177–85
- Wiederhold JG, Smith RS, Siebner H, Jew AD, Brown GE Jr., et al. 2013. Mercury isotope signatures as tracers for Hg cycling at the New Idria Hg mine. *Environ. Sci. Technol.* 18:6137–45
- Wilson M. 1968. *Ab initio* calculation of screening effects on  $|\psi(0)|^2$  for heavy atoms. *Phys. Rev.* 176:58–63
- Wisdom J, Tian Z. 2015. Early evolution of the Earth-Moon system with a fast-spinning Earth. *Icarus* 256:138–46
- Wittig N, Humayun M, Brandon A, Huang S, Leya I. 2013. Coupled W–Os–Pt isotope systematics in IVB iron meteorites: in situ neutron dosimetry for W isotope chronology. *Earth Planet. Sci. Lett.* 361:152–61
- Wombacher F, Rehkämper M. 2003. Investigation of the mass discrimination of multiple collector ICP-MS using neodymium isotopes and the generalised power law. *J. Anal. At. Spectrom.* 18:1371–75
- Woodsley S. 1997. Neutron-rich nucleosynthesis in carbon deflagration supernovae. *Astrophys. J.* 476:801
- Yamakawa A, Yamashita K, Makishima A, Nakamura E. 2010. Chromium isotope systematics of achondrites: chronology and isotopic heterogeneity of the inner solar system bodies. *Astrophys. J.* 720:150

- Yamashita K, Ueda T, Nakamura N, Kita N, Heaman L. 2005. Chromium isotopic study of mesosiderite and ureilite: evidence for  $\epsilon^{54}\text{Cr}$  deficit in differentiated meteorites. *NIPR Symp. Antarct. Meteorit.* 29:100–1
- Yang S, Liu Y. 2015. Nuclear volume effects in equilibrium stable isotope fractionations of mercury, thallium and lead. *Sci. Rep.* 5:12626
- Yeung LY, Young ED, Schauble EA. 2012. Measurements of  $^{18}\text{O}^{18}\text{O}$  and  $^{17}\text{O}^{18}\text{O}$  in the atmosphere and the influence of isotope-exchange reactions. *J. Geophys. Res.* 117:D18306
- Yokoi K, Takahashi K, Arnould M. 1983. The  $^{187}\text{Re}$ – $^{187}\text{Os}$  chronology and chemical evolution of the Galaxy. *Astron. Astrophys.* 117:65–82
- Yokoyama T, Alexander CMD, Walker RJ. 2010. Osmium isotope anomalies in chondrites: results for acid residues and related leachates. *Earth Planet. Sci. Lett.* 291:48–59
- Yokoyama T, Fukami Y, Okui W, Ito N, Yamazaki H. 2015. Nucleosynthetic strontium isotope anomalies in carbonaceous chondrites. *Earth Planet. Sci. Lett.* 416:46–55
- Young ED. 2014. Inheritance of solar short- and long-lived radionuclides from molecular clouds and the unexceptional nature of the solar system. *Earth Planet. Sci. Lett.* 392:16–27
- Young ED, Galy A, Nagahara H. 2002. Kinetic and equilibrium mass-dependent isotope fractionation laws in nature and their geochemical and cosmochemical significance. *Geochim. Cosmochim. Acta* 66:1095–104
- Young ED, Kuramoto K, Marcus RA, Yurimoto H, Jacobsen SB. 2008. Mass-independent oxygen isotope variation in the solar nebula. *Rev. Mineral. Geochim.* 68:187–218
- Young ED, Russell SS. 1998. Oxygen reservoirs in the early solar nebula inferred from an Allende CAI. *Science* 282:452–55
- Young ED, Yeung LY, Kohl IE. 2014. On the  $\delta^{17}\text{O}$  budget of atmospheric  $\text{O}_2$ . *Geochim. Cosmochim. Acta* 135:102–25
- Yung YL, De Mone WB, Pinto JP. 1991. Isotopic exchange between carbon dioxide and ozone via  $\text{O}(^1\text{D})$  in the stratosphere. *Geophys. Res. Lett.* 18:13–16
- Yurimoto H, Kuramoto K. 2004. Molecular cloud origin for the oxygen isotope heterogeneity in the solar system. *Science* 305:1763–66
- Zhang J. 2012. *Titanium isotope cosmochemistry*. PhD Diss., Dep. Geophys. Sci., Univ. Chicago
- Zhang J, Dauphas N, Davis AM, Leya I, Fedkin A. 2012. The proto-Earth as a significant source of lunar material. *Nat. Geosci.* 5:251–55
- Zinner EK. 2003. Presolar grains. In *Treatise on Geochemistry*, Vol. 1: *Meteorites, Comets, and Planets*, ed. AM Davis, pp. 17–39. Oxford, UK: Elsevier-Pergamon. 1st ed.
- Zinner EK, Fahey AJ, McKeegan KD, Goswami JN, Ireland TR. 1986. Large  $^{48}\text{Ca}$  anomalies are associated with  $^{50}\text{Ti}$  anomalies in Murchison and Murray hibonites. *Astrophys. J.* 311:L103–7
- Zinner EK, Göpel C. 2002. Aluminum-26 in H4 chondrites: implications for its production and its usefulness as a fine-scale chronometer for early solar system events. *Meteorit. Planet. Sci.* 37:1001–13



# Contents

Tektites, Apollo, the Crust, and Planets: A Life with Trace Elements <i>Stuart Ross Taylor</i> .....	1
Environmental Detection of Clandestine Nuclear Weapon Programs <i>R. Scott Kemp</i> .....	17
From Tunguska to Chelyabinsk via Jupiter <i>Natalia A. Artemieva and Valery V. Shuvalov</i> .....	37
The Lakes and Seas of Titan <i>Alexander G. Hayes</i> .....	57
Inference of Climate Sensitivity from Analysis of Earth's Energy Budget <i>Piers M. Forster</i> .....	85
Ocean Basin Evolution and Global-Scale Plate Reorganization Events Since Pangea Breakup <i>R. Dietmar Müller, Maria Seton, Sabin Zabirovic, Simon E. Williams, Kara J. Matthews, Nicky M. Wright, Grace E. Shephard, Kayla T. Maloney, Nicholas Barnett-Moore, Maral Hosseinpour, Dan J. Bower, and John Cannon</i> ....	107
Lithification Mechanisms for Planetary Regoliths: The Glue that Binds <i>John G. Spray</i> .....	139
Forensic Stable Isotope Biogeochemistry <i>Thure E. Cerling, Janet E. Barnette, Gabriel J. Bowen, Lesley A. Chesson, James R. Ehleringer, Christopher H. Remien, Patrick Shea, Brett J. Tipple, and Jason B. West</i> .....	175
Reconstructing Ocean pH with Boron Isotopes in Foraminifera <i>Gavin L. Foster and James W.B. Rae</i> .....	207
Sun, Ocean, Nuclear Bombs, and Fossil Fuels: Radiocarbon Variations and Implications for High-Resolution Dating <i>Koushik Dutta</i> .....	239
Climate Sensitivity in the Geologic Past <i>Dana L. Royer</i> .....	277

Redox Effects on Organic Matter Storage in Coastal Sediments During the Holocene: A Biomarker/Proxy Perspective <i>Thomas S. Bianchi, Kathryn M. Schreiner, Richard W. Smith, David J. Burdige, Stella Woodard, and Daniel J. Conley</i> .....	295
Fracking in Tight Shales: What Is It, What Does It Accomplish, and What Are Its Consequences? <i>J. Quinn Norris, Donald L. Turcotte, Eldridge M. Moores, Emily E. Brodsky, and John B. Rundle</i> .....	321
The Climate of Titan <i>Jonathan L. Mitchell and Juan M. Lora</i> .....	353
The Climate of Early Mars <i>Robin D. Wordsworth</i> .....	381
The Evolution of Brachiopoda <i>Sandra J. Carlson</i> .....	409
Permafrost Meta-Omics and Climate Change <i>Rachel Mackelprang, Scott R. Saleska, Carsten Subr Jacobsen, Janet K. Jansson, and Neslihan Taş</i> .....	439
Triple Oxygen Isotopes: Fundamental Relationships and Applications <i>Huiming Bao, Xiaobin Cao, and Justin A. Hayles</i> .....	463
Cellular and Molecular Biological Approaches to Interpreting Ancient Biomarkers <i>Dianne K. Newman, Cajetan Neubauer, Jessica N. Ricci, Chia-Hung Wu, and Ann Pearson</i> .....	493
Body Size Evolution Across the Geozoic <i>Felisa A. Smith, Jonathan L. Payne, Noel A. Heim, Meghan A. Balk, Seth Finnegan, Michał Kowalewski, S. Kathleen Lyons, Craig R. McClain, Daniel W. McShea, Philip M. Novack-Gottshall, Paula Spaeth Anich, and Steve C. Wang</i> .....	523
Nuclear Forensic Science: Analysis of Nuclear Material Out of Regulatory Control <i>Michael J. Kristo, Amy M. Gaffney, Naomi Marks, Kim Knight, William S. Cassata, and Ian D. Hutcheon</i> .....	555
Biomarker Records Associated with Mass Extinction Events <i>Jessica H. Whiteside and Kliti Grice</i> .....	581
Impacts of Climate Change on the Collapse of Lowland Maya Civilization <i>Peter M. J. Douglas, Arthur A. Demarest, Mark Brenner, and Marcello A. Canuto</i> ...	613

Evolution of Oxygenic Photosynthesis <i>Woodward W. Fischer, James Hemp, and Jena E. Johnson</i> .....	647
Crustal Decoupling in Collisional Orogenesis: Examples from the East Greenland Caledonides and Himalaya <i>K.V. Hodges</i> .....	685
Mass Fractionation Laws, Mass-Independent Effects, and Isotopic Anomalies <i>Nicolas Dauphas and Edwin A. Schauble</i> .....	709

## Indexes

Cumulative Index of Contributing Authors, Volumes 35–44 .....	785
Cumulative Index of Article Titles, Volumes 35–44 .....	790

## Errata

An online log of corrections to *Annual Review of Earth and Planetary Sciences* articles may be found at <http://www.annualreviews.org/errata/earth>